Implementation of a Coupled Creep Damage Model in MOOSE Finite Element Framework: Application to Irradiated Concrete Structures

by

Naman Saklani

A Dissertation Presented in Partial Fulfillment
of the Requirements for the Degree
Doctor of Philosophy

Approved April 2020 by the
Graduate Supervisory Committee:

Narayanan Neithalath, Chair
Subramanian Rajan
Barzin Mobasher
Christian Hoover
Nikhilesh Chawla

ARIZONA STATE UNIVERSITY

May 2020

ABSTRACT

There has been a renewed interest to understand the degradation mechanism of concrete under radiation as many nuclear reactors are reaching their expiration date. Much of the information on the degradation mechanism of concrete under radiation comes from the experiments, which are carried out on very small specimens. With the advent of finite element analysis, a numerical predictive tool is desired that can predict the extent of damage in the nuclear concrete structure.

A mesoscale micro-structural framework is proposed in Multiphysics Object-Oriented Simulation Environment (MOOSE) finite element framework which represents the first step in this direction. As part of the framework, a coupled creep damage algorithm was developed and implemented in MOOSE. The algorithm considers creep through rheological models, while damage evolves exponentially as a function of elastic strain and creep strain. A characteristic length is introduced in the formulation such that the energy release rate associated with each element remains the same to avoid vanishing energy dissipation with mesh refinement. A creep damage parameter quantifies the effect of creep strain on the damage that was calibrated using three-point bending experiments with varying rates of loading.

The creep damage model was also validated with restrained ring shrinkage tests on cementitious materials containing compliant/stiff inclusions subjected to variable drying conditions. The simulation approach explicitly considers: (i) moisture diffusion driven differential shrinkage along the depth of the specimen (ii) viscoelastic response of aging cementitious materials (iii) isotropic damage model with Rankine′s failure initiation criterion, and (iv) random distribution of tensile strengths of individual finite elements.

The model was finally validated with experimental results on neutron-irradiated concrete. The simulation approach considers: (i) coupled hygro-thermal model to predict the temperature and humidity profile inside the specimen (ii) radiation-induced volumetric expansion of aggregates (RIVE) (iii) thermal, shrinkage and creep effects based on the temperature and humidity profile and (iv) isotropic damage model with Rankine's criterion to determine failure initiation.

DEDICATION

To my parents Keshav Chandra Saklani, Prabha Saklani and my sisters, Akanksha Saklani Gupta and Megha Saklani Bhatt for their constant support and encouragement.

ACKNOWLEDGMENTS

I would like to thank Dr. Narayanan Neithalath for providing me with this opportunity and his constant guidance, mentorship, support during the completion of this work. I am highly indebted for his patience when I struggled in this journey. I would also like to thank Dr. Subramaniam Rajan for his guidance, inputs and discussions which greatly helped in the completion of this work. I would also like to thank my committee members, Dr. Barzin Mobasher, Dr. Christian Hoover, Dr. Nikhilesh Chawla for their guidance and meaningful discussions.

I would like to extend special thanks to Dr. Benjamin Spencer, Idaho National Laboratory for answering many of my questions and long hours of discussions. I would also like to thank Dr. Bilal Khaled for the various meaningful discussions and his constant moral support. I would also like to thank my colleagues Aashay Arora, Aakash Dakhane and Gaurav Banwat for their immense help in the completion of this work. I would also like to thank all my friends and colleagues who made my life memorable at Arizona State University. Finally, I would like to thank Arizona State University for providing me with necessary resources that helped immensely in the completion of this thesis.

TABLE OF CONTENTS

Page

CHAPTER Page

LIST OF TABLES

LIST OF FIGURES

Figure Page

Figure Page

Figure Page

Figure Page

CHAPTER 1

INTRODUCTION

1.1 Background

The nuclear power plants are generally decommissioned from use after 40 to 80 years of operation. Nuclear power plants in the US are given a renewal of 20 years by the U.S. Nuclear Regulatory Commission (NRC) only if it has reasonable confidence regarding its safe operation ("NRC: Backgrounder on Reactor License Renewal"). NRC is currently reviewing renewal application for 17 reactors, 8 of which are due to expire by 2025. The process of decommissioning a nuclear power plant is extremely long and costly process as it must be ensured that the residual radioactivity is below a minimum threshold in these reactors ("What's the Lifespan for a Nuclear Reactor? Much Longer Than You Might Think"). The possibility to extend the operations of these nuclear power plants has been one of the leading points of discussion in the nuclear industry ("NRC: Backgrounder on Reactor License Renewal"; Giorla Alain B., Le Pape Yann, and Dunant Cyrille F. 2017; Pomaro 2016). This has renewed interest in understanding the degradation mechanism of concrete under radiation. Concrete walls are used as a shield inside nuclear power plants to arrest radiations. The primary support structure for the reactor pressure vessel is also made of concrete and is exposed to chronic irradiation during its operation. However, this chronic irradiation damages the concrete, severely reducing its strength and capability to arrest further radiation. A mesoscale microstructure framework is implemented in MOOSE to simulate the expansion under irradiation induced swelling of otherwise elastic aggregates and corresponding damage propagation in the paste undergoing creep, thermal strain, and drying shrinkage. As part of this framework, a coupled creep damage algorithm

is also implemented and tested against three-point bend experiments and early age shrinkage tests. The framework is validated with the experimental results of Maruyama et al. (Maruyama et al. 2017), which to date feature the most comprehensive set of tests on irradiated concrete. The framework considers the effect of elevated temperature, moisture condition and high neutron fluence on the mortar and aggregates separately. This numerical framework presents the first step towards having a numerical tool that can aid the researchers to ascertain the design life of concrete structure under chronic radiation.

1.2 Objective

The main objectives of the present study are:

a) Implementing a coupled creep damage algorithm in MOOSE framework, a finite element analysis tool kit developed by Idaho National Laboratory.
b) Analyzing the effect of creep strain on damage propagation using experimental three-point bend results under different rates of loading.
c) Using the coupled creep damage model for analyzing the cracking time in restrained ring shrinkage tests with changing relative humidity and the effect of soft/stiff inclusions
d) Utilizing the coupled creep damage model to simulate damage propagation in irradiated concrete using coupled hygro-thermal analysis and a coupled creep damage model.

1.3 Dissertation Layout

This dissertation is primarily composed of three research papers with each being published, submitted or under preparation for submission.

Chapter 2 presents the literature review on experiments and numerical simulation for concrete undergoing early age shrinkage and irradiation. It also describes the literature review on the constitutive model used for solving such problems. Chapter 3 discusses the MOOSE framework, the finite element analysis toolkit used in the analysis and its capabilities. This section also talks about the Jaobian free Newton Krylov technique and the modular architecture of MOOSE that make it easy to add new capabilities in the existing framework. It also describes the theory and numerical implementation of the existing creep and hygro-thermal model in MOOSE. Chapter 4 describes the implementation of a coupled creep damage model in the MOOSE framework and its verification using single element tests and its validation using three-point bend experiments under different rates of loading. Chapter 5 describes the validation of the model using ring test experiments using moisture diffusion theory and creep damage algorithm. Chapter 6 validates the model by simulating irradiation induced concrete expansion and damage. Chapter 7 summarizes the results and presents the conclusion of this study.

CHAPTER 2

LITERATURE REVIEW

The preceding literature review is composed of three sections. The first section talks about the radiation induced volumetric expansion of concrete and corresponding damage in concrete structures and the mechanisms and conditions to be considered while developing a numerical tool to predict the damage in such conditions. The second section talks about restrained shrinkage test and the conditions for the numerical tools to predict the damage under such condition. The third section talks about the various constitutive models for concrete available in the literature. These models comprise both the hygro-thermal model that simulate the heat and water diffusion in concrete and the mechanical models that can predict mechanical behavior such as creep, damage and its interaction.

2.1 Radiation Induced Volumetric Expansion of Concrete

The possibility to extend the operation of nuclear power plants requires to understand the various degradation phenomenon that takes place in concrete as it is widely used in the construction of nuclear power plants. Much of the experimental investigations on irradiated concrete was done till early seventies (Elleuch, Dubois, and Rappeneau 1972; Dubrovskij et al. 1966; Alexander 1963; Blosser et al. 1958; Cristiani, Granata, and Montagnini 1972; Dubrovskii et al. 1967; Gray 1972; Kelly et al. 1969) after which it was mostly disregarded. Recently, Maruyama et al. (Maruyama et al. 2017) carried out tests on irradiated concrete, which to date feature the most comprehensive set of tests on irradiated concrete. These tests provided conclusive evidence that radiation induced volumetric expansion of aggregate due to metamictization (also called amorphization in some works) coupled with drying of paste due to radiolysis and gamma heating cause damage in the specimen.

However, there was a vide disparity in these experiments in terms of neutron fluence, type of aggregate, type of cement paste, water cement ratio, irradiation conditions to name a few. A majority of tests were reviewed by Hilsdorf et al. (Hilsdorf, Kropp, and Koch 1978) and concluded that degradation of concrete starts at fluence level of $1x10^{19}$ n/cm^2 and decreases monotonically up to $1x10^{20}$n/cm^2, which is usually set as the reference level for neutron irradiation beyond which concrete is no longer considered sound. The study also concluded $2x10^5$ kGy as the limit for gamma energy deposition after which the concrete is no longer considered sound. It should be noted that the irradiated conditions in the test reactors differ vastly in comparison to actual scenario in a light water reactor (Field, Remec, and Pape 2015). Therefore, to extrapolate the results of these experiments to actual reactors requires an efficient numerical framework. The framework should consider the various time dependent mechanisms such as creep, shrinkage, radiation and high temperature induced expansion that takes place in concrete under an irradiated scenario. This requires correct estimation of all the conditions such as temperature, moisture and radiation profile inside the concrete. While temperature in a lightweight reactor (LWRs) is close to around 65^{o}C, it can vary significantly in test reactors from 50^{o}C to 500^{o}C. These high temperature can affect kinetic of moisture transport (Bai, Wang, and Xi 2020; Wang and Xi 2017), which can then affect the creep and shrinkage properties (Zdeněk P. Bažant 1983; Zdenek P. Bažant and Baweja 2000; Acker and Ulm 2001). The actual moisture condition is difficult to assess as it is typically not measured during the experiments. Gamma radiation is subsequently produced during neutron irradiation. In light water reactors the total dose at the end of 80 years could be around 200 MGy. The gamma rays' dosages are not sufficient to cause metamictization of aggregates, however, it causes

radiolysis of water present in the hardened cement paste (Maruyama et al. 2017; “Impact of Gamma-Ray Irradiation on Hardened White Portland Cement Pastes Exposed to Atmosphere | Elsevier Enhanced Reader”). The gamma rays are ultimately converted to heat, referred as gamma heating and cause drying shrinkage due to loss of water from the specimen. The elevated temperature also has a healing effect that reduces the radiation induced volumetric expansion of aggregates (Bykov et al. 1981). Le Pape et al. (Le Pape, Field, and Remec 2015) developed a micro mechanical model for concrete using homogenization of random media. Salomoni et al. (Salomoni et al. 2014, 4) carried out simulations on a meso-scale model by considering mortar and aggregate separately, however, they did not consider RIVE in their simulations. Using constant pore humidity and temperature profiles over the specimen, Giorla et al. (A. Giorla et al. 2015) also carried out 2D simulations on mesoscale concrete specimens. A constant pore humidity and temperature profile is a good first approximation for comparatively thin sections used in test reactors. However, it is necessary to consider the variation in temperature and moisture profiles if the numerical framework is to be used for simulation of actual nuclear structures, the depth of which could be in meters such as that of a containment wall.

2.2 Restrained Ring Shrinkage Tests

Volume changes in early-age concrete occur as a result of loss of moisture, temperature changes, and mismatch in the volumes of the reactants and products. When these volume changes are restrained, residual stresses are developed. When the residual stress exceeds the tensile strength of concrete, early-age cracking occurs (Bentz 2008; Henkensiefken et al. 2009; W. Jason Weiss, Yang, and Shah 1998; Neithalath, Pease, and Attiogbe 2005). It is well known that early-age cracking is a function of the geometry of the structure,

temperature change, rate and heat of reaction (hydration), temporal development of mechanical properties (including tensile strength, stiffness and viscoelasticity), the thermal characteristics of the concrete (i.e., heat capacity and coefficient of thermal expansion, which depend on the concrete constituents), and the imposed external conditions (temperature, relative humidity, and wind speed) (Holt and Leivo 2004; Altoubat and Lange 2001; Hooton et al. 1999; W. Jason Weiss, Yang, and Shah 2000; Carlson and Reading 1988). The restrained ring test (ASTM C 1581 and AASHTO T 334) has been commonly used to determine the residual stress development and cracking potential of concrete at early ages (S. W. Dean et al. 2010; Schlitter, Bentz, and Weiss 2013; See, Attiogbe, and Miltenberger 2003; W. Jason Weiss, Yang, and Shah 2000; Passuello, Moriconi, and Shah 2009). In its basic form, the ring tests consists of a concrete annulus cast in between two steel (or Invar, which has a very low coefficient of thermal expansion) rings (dual ring test), or around an inner ring. Expansion of concrete is restrained by both the inner and outer rings, which impose a compressive stress in the concrete annulus, while shrinkage is restrained by the inner ring, which causes circumferential tensile stresses to develop in the concrete annulus. Restrained ring tests have been used to investigate the influence of cement type, supplementary cementitious materials, and admixtures on the cracking response of cement-based materials (Passuello, Moriconi, and Shah 2009; W. J. Weiss and Shah 2002). Several variants of the ring test exist: changing the thickness of the steel/invar rings to simulate differing degrees of restraint (Hossain and Weiss 2004), changing the thickness and height of the concrete annulus (Hossain and Weiss 2006; W. J. Weiss and Shah 2002), and changing the ring geometry (circular/elliptical) (Dong et al. 2017; Zhou, Dong, and Oladiran 2014). Recently, the influence of inclusion type (soft or

stiff) on cracking behavior also has been elucidated using the ring test (Wei, Falzone, Das, et al. 2017b), where microencapsulated phase change materials (PCM) are used as soft inclusions and quartz particles as hard inclusions. PCMs are combined sensible-and-latent thermal energy storage materials that can be used to store and dissipate energy in the form of heat (Fernandes et al. 2014; Aguayo et al. 2016; Khudhair and Farid 2004). Their efficiency in controlling early-age cracking, when used as a concrete ingredient in microencapsulated form, has been demonstrated (Fernandes et al. 2014). The numerical simulation for these tests requires consideration of the moisture diffusion driven differential shrinkage, aging viscoelasticity and random strength distribution. Since the viscoelastic properties are experimentally difficult to measure for early age cementitious materials, previous numerical studies on restrained ring shrinkage tests have simplified the viscoelastic behavior using an effective elastic modulus (Moon and Weiss 2006; Dong et al. 2017; S. Dean et al. 2006; Zhou, Dong, and Oladiran 2014) or derived the viscoelastic parameters by matching the stresses in the restrained ring with those obtained from the numerical simulations (Raoufi et al. 2011). Many studies also oversimplified the shrinkage by considering plane stress assumptions, as such did not consider shrinkage variation along the depth of ring (Raoufi et al. 2011).

2.3 Constitutive Model for Concrete

As seen above, there are a multitude of complex mechanisms that takes place in concrete during experiments. The complexity arises from the various time dependent mechanisms and its interaction that take place in concrete (Zdeněk P. Bažant, 1988; Acker and Ulm 2001; Altoubat and Lange 2001; Di Luzio 2009; Zdenek P. Bažant and Baweja 2000). These mechanisms depend upon a variety of factors such as the age of concrete,

environmental conditions, the moisture state inside the concrete, modulus of aggregate, volume of aggregate, maximum aggregate size, degree of hydration etc. The experiments that characterize the mechanical behavior of concrete are usually carried out at constant temperature and humidity. In actual structures or experiments as in Section 2.1 and 2.2, the temperature and/or humidity conditions are never constant. Moreover, moisture transport takes place inside the concrete under elevated temperature (Bai, Wang, and Xi 2020; Stefan 2015; Wang and Xi 2017). Therefore, in such cases, a hygro-thermal analysis is required as the state of moisture and/or temperature is continuously changing inside the concrete structures. The development of hygro-thermal model in concrete will be described in the next section and theory and numerical implementation of the model available in MOOSE framework will be described in detail in Chapter 3. Apart from the hygro-thermal model, the mechanical constitutive model for concrete describes it mechanical behavior under different loading conditions. Under quasi-static conditions, the behavior of concrete is considered elastic. However, if there is a time component involved, concrete is considered as a viscoelastic material. If the applied stress exceeds the material strength, a damage model is usually employed. The development of damage model (Pijaudier-Cabot and Mazars 2001) for concrete will be discussed in Section 2.1.2. It is also well known that fracture that occurs in concrete is also rate sensitive and there exists enough evidence that creep and damage are related. Therefore, a correct prediction of the behaviour of concrete structures requires a correct understanding of all the possible coupled mechanisms that take place inside the concrete. Some of the models available in literature will be described in the Section 2.1.2 while the theory and implementation of creep damage model for this work will be described in Chapter 4.

2.3.1 Coupled Hygro-Thermal Model for Concrete

The moisture transport characteristics for a porous material is usually characterized using theory of partially saturated porous media (Bear 1991; Ingham and Pop 1998; Du Plessis and Masliyah 1988). These theories are very difficult to apply to a material like concrete as the parameters to account for such processes are very hard to determine for concrete. As a result, simpler models such as (Z. P. Bažant and Najjar 1971; Ababneh, Benboudjema, and Xi 2003) are used which use fewer parameters and can be easily calibrated from experiments. Much of the evaporable water of concrete remains in the nanopores and is called hindered adsorbed water and its movement is controlled by surface forces of adsorption. Under isothermal condition, its movement can be described by the water mass balance equation per unit volume,

$$\frac{\partial W}{\partial t} = \nabla . J_W + \frac{\partial W_d}{\partial t} \tag{2.1}$$

where, W is the total water content, $J_W = C\nabla \mathrm{W}$ is the moisture flux. W_d is the total mass of free evaporable water released into the pores by dehydration of cement paste. Also, it has been shown that the evaporable water content could be replaced by relative humidity inside the pore. This is called pore relative humidity and is equal to the partial vapor pressure of water vapor divided by the saturated vapor pressure. This pore humidity is the primary unknown in the moisture diffusion equation. The governing moisture diffusion equation is then formulated as

$$\frac{\partial W}{\partial H}\frac{\partial H}{\partial t} = \nabla(J_H) + \frac{\partial W_d}{\partial t} \tag{2.2}$$

where, H is the pore relative humidity, J_H is also the moisture flux but expressed as

$$J_H = D_H \nabla \mathrm{H} \tag{2.3}$$

Both moisture capacity $\frac{\partial W}{\partial H}$ and moisture diffusivity D_H depends on the relative humidity H which makes this equation highly nonlinear. The moisture capacity $\frac{\partial W}{\partial H}$ can be considered constant if H lies between 0.2 and 1 (Powers and Brownyard 1946). It can also be obtained from desorption isotherms. Additionally, it can also be obtained from the empirical relation for desorption isotherms provided by Xi et al. (Xi, Bažant, and Jennings 1994) which is based on the Brunauer-Emmett-Teller (BET) adsorption isotherm theory. The model has been shown to predict the moisture capacity for a range of water cement ratio, cement type, curing time and temperature. The moisture diffusivity is a complex function of temperature T, relative humidity H, and pore structure of concrete. There are indeed various diffusion mechanisms taking place simultaneously due to the different size of the pores. Kunzel (Künzel 1995) proposed a diffusion model that combined pressure difference induced water vapor diffusion, liquid water diffusion through micropores and capillary pores, and the moisture diffusion due to gradient in relative humidity in larger pores. Most models for concrete, however, are empirical in nature and do not account for different diffusion mechanisms and tend to reproduce the overall trend. Among the first such work for concrete was proposed by Bazant and Najjar (Z. P. Bažant and Najjar 1971) which considered a S- shape curve and Mensi (Mensi, Acker, and Attolou 1988) which considered an exponential curve that describes the diffusion coefficient in terms of relative humidity in the pores of concrete. The model by Bazant and Najjar (Z. P. Bažant and Najjar 1971) was later expanded to include the effect of temperature as in Bazant and Thonguthai (Bazant and Thonguthai 1978). The effect of water cement ratio and age for cement paste was considered as in (Xi et al. 1994). This was further extended to a concrete using composite theory by Ababneh (Ababneh, Benboudjema, and Xi 2003).

In regular service of concrete structures, the temperature is usually below 50^{o}C, however, it can go as high as ~ 70^{o}C in nuclear reactors, ~200^{o}C in irradiation experiments and ~ 1000^{o}C in a fire accident scenario. These high temperatures can have substantial effect on the moisture transport characteristic which in turn can affect the creep and shrinkage kinetics. It is therefore necessary to have a model that can realistically predict behavior of concrete at elevated temperature. The pioneering work in coupled moisture-heat transfer in capillary porous solids was done by Luikov et al. (Luikov 1975). In this study moisture diffusion takes place not just under liquid concentration gradient but also under a temperature gradient, commonly known as Soret effect. The study also considers that as liquid moves, the enthalpy transfer occurs as well. Luikov proposed the coupled differential equations for heat and mass transfer in the capillary porous bodies using Fourier's equation for heat transfer, Fick's equation for mass transfer and their interaction. The three basic assumptions used in these equations were as follows: (i) Body volume always remains constant. (ii) The different phases have equal temperature which is same as that of the mass skeleton. (iii) Mass content of liquid is equal to the mass content of water, i.e. mass of water vapor and air are considered negligible. Bažant and Thonguthai (Bazant and Thonguthai 1978; Zdeněk P. Bažant and Thonguthai 1979; Zdeněk P. Bažant, Chern, and Thonguthai 1982) extended this theory to concrete for coupled heat and moisture transfer in concrete at high temperature. They simplified the expression by assuming that vapor pressure causes mass transfer in the concrete. Using heat equilibrium, the governing partial differential equation for coupled heat and moisture transfer was given by (Bazant and Thonguthai 1978; Zdeněk P. Bažant and Thonguthai 1979; Zdeněk P. Bažant, Chern, and Thonguthai 1982),

$$\rho C \frac{\partial T}{\partial t} = \nabla(\mathrm{k}\nabla\mathrm{T}) + C_w \mathrm{J}\nabla\mathrm{T} + C_a \frac{\partial W}{\partial H}\frac{\partial H}{\partial t} + Q \tag{2.4}$$

where, $\rho C \frac{\partial T}{\partial t}$ represents heat consumed due to the change in temperature per unit volume per unit time, with ρ being the density, C being the specific heat (per unit mass), T is the temperature. $\nabla(\mathrm{k}\nabla\mathrm{T})$ represents rate of heat supplied by thermal conduction with k being thermal conductivity of concrete. $C_w \mathrm{J}\nabla\mathrm{T}$ represents the convective heat transport due to water movement with C_w being the isobaric heat capacity of water. $C_a \frac{\partial W}{\partial H}\frac{\partial H}{\partial t}$ represents the heat flow due to adsorption of free water molecules. Q represents the volumetric heat source. The thermal capacity and conductivity of mortar is assumed to be constant as it doesn't change appreciably below 100°C (Kodur, Wang, and Cheng 2004). The modified governing equation for moisture diffusion in concrete is given by,

$$\frac{\partial W}{\partial H}\frac{\partial H}{\partial t} = \nabla(\mathrm{D}_h \nabla\mathrm{H}) + \nabla(\mathrm{D}_{ht}\nabla\mathrm{T}) + \frac{\partial W_d}{\partial t} \tag{2.5}$$

where, D_{ht} is the coupled moisture diffusivity under the influence of a temperature gradient. The theory and numerical implementation of this model in MOOSE is described in Chapter 3.

2.3.2 Creep Damage Constitutive Model for Concrete

The mechanical response of concrete to loading is highly complicated and even the sophisticated model available cannot cover all the material properties. The increased use to concrete as a structural material necessitated the use of sophisticated material model to a variety of loading situations. In order to simulate high level loading under a long duration, such as the one in this work, it becomes necessary to understand creep, damage and its interaction. Damage arising due to creep is usually not included in the analysis of

reinforced concrete structures (C Mazzotti and Savoia 2001; Claudio Mazzotti and Savoia 2003; Pijaudier-Cabot et al. 2005). However, it becomes necessary to consider the effect of creep on fracture and failure in massive structures such as dams and nuclear power plants (C Mazzotti and Savoia 2001; Claudio Mazzotti and Savoia 2003; Zdenek P. Bažant and Gettu 1992; Giorla Alain B., Le Pape Yann, and Dunant Cyrille F. 2017; Zdenek P. Bažant and Baweja 2000; Altoubat and Lange 2001). It has been shown that creep is likely to reduce the expected life span of these structures (Giorla Alain B., Le Pape Yann, and Dunant Cyrille F. 2017; Challamel, Lanos, and Casandjian 2005). To realistically simulate such behavior, a combined creep-damage model is highly desirable. Cementitious materials can be considered to be linear viscoelastic at low stress levels (stress < 40-60% of the strength). Since the principle of superposition is valid for linear viscoelastic materials, the constitutive equation can be expressed as:

$$\left.\begin{aligned} \bar{\varepsilon}(t) &= \int_0^t J(t,t'):\frac{\partial \bar{\sigma}(t')}{\partial t'}\,\mathrm{d}t' \\ \bar{\sigma}(t) &= \int_0^t R(t,t'):\frac{\partial \bar{\varepsilon}(t')}{\partial t'}\,\mathrm{d}t' \end{aligned}\right\} \tag{2.6}$$

where, $J(t,t')$ and $R(t,t')$ are the creep compliance and relaxation functions, and $\bar{\varepsilon}$ and $\bar{\sigma}$ are the strain and stress tensor, respectively. The creep compliance or relaxation function can be obtained from creep or relaxation tests. Creep compliance can also be obtained using formulations such as the double power law (BP model (Zdeněk P. Bažant, 1988)), which is used in the present study. Creep is generally modeled using generalized Kelvin-Voigt (Figure 2-1(a)) or Maxwell models (Figure 2-1(b)) to represent the rheological behavior. It is easier to represent creep data using a generalized Kelvin-Voigt model, while relaxation data is more easily represented using a generalized Maxwell model (Zdeněk P. Bažant and

Wu 1974; 1973). To model the complex relaxation/creep behavior of aging concrete, the spring/dashpot properties can be varied, for e.g., with time, temperature or relative humidity (A. B. Giorla 2017).

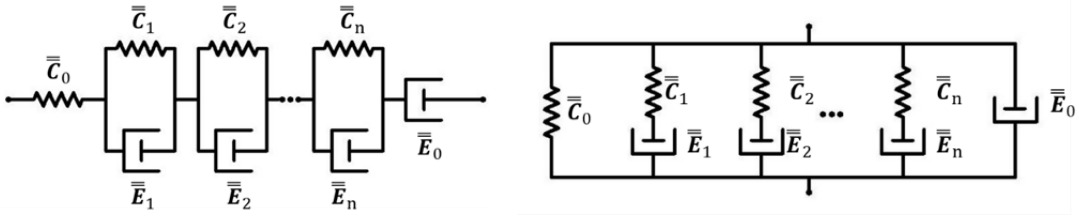

(a) (b)

Figure 2-1. (a) Generalized Kelvin-Voigt Model and (b) Generalized Maxwell Model

Significant progress has been made to simulate damage in quasi brittle materials, such as concrete (Kurumatani et al. 2016; Zdeněk P. Bažant and Lin 1988; Zdeněk P. Bažant and Oh 1983; Hillerborg, Modéer, and Petersson 1976; Zdenek P. Bažant and Planas 1997). In these materials, the crack tip is surrounded by a large fracture process zone which encapsulates a region of distributed microcracking (Pijaudier-Cabot, Bažant, and Tabbara 1988; Zdeněk P. Bažant et al. 1984; Zdeněk P. Bažant and Lin 1988). This causes strain softening in the material such that there is a gradual decline of stress with increasing strain. In continuum models, strain softening causes incorrect convergence of solutions causing vanishing energy dissipation as the mesh is refined (Pijaudier-Cabot, Bažant, and Tabbara 1988; Zdeněk P. Bažant and Lin 1988; de Vree, Brekelmans, and van Gils 1995). However, continuum models are still preferred over discrete models because of the ease with which they can be incorporated into computational frameworks. Moreover, modeling distributed cracking using the discrete crack approach is difficult. The problem of incorrect convergence of energy dissipation due to strain softening has been tackled using the crack band approach (Zdeněk P. Bažant and Oh 1983), regularization or non-local methods

(Zdeněk P. Bažant and Lin 1988; Zdeněk P. Bažant and Pijaudier-Cabot 1989; Pijaudier-Cabot and Bažant 1987), or energy equivalence (also called cohesive crack) approach (Kurumatani et al. 2016; Hillerborg, Modéer, and Petersson 1976; Zhang et al. 2002). The crack band approach involves fixing the size of the mesh to avoid incorrect convergence, keeping the fracture energy constant (Zdeněk P. Bažant and Oh 1983). The regularization method uses an internal length, the definition of which has been quite ambiguous. Here, it is assumed that the strain at a point is dependent on the strain at nearby points lying inside a sphere with a radius equal to the internal length. While this can be related to distributed cracking in the sense that strain at a point is governed by microcracks occurring in the fracture zone, there has never been a consensus regarding what is an appropriate value of internal length. Bažant and coworkers (Pijaudier-Cabot, Bažant, and Tabbara 1988; Zdeněk P. Bažant and Pijaudier-Cabot 1989; Pijaudier-Cabot and Bažant 1987) have routinely used a value of $3d$, with d being the largest aggregate size, as the internal length. Values ranging from $2d$ to $13d$ have also been found to give reasonable global response for specimens under three-point bending (Le Bellégo et al. 2003). In the energy equivalence approach, first proposed by Hillerborg et al. (Hillerborg, Modéer, and Petersson 1976), the fracture energy is specified as one of the material parameters. The fracture process zone of concrete is modeled as a discrete crack which is characterized by a stress-displacement law and not by stress-strain relations. Kurumatani et al. (Kurumatani et al. 2016) included the cohesive zone modeling approach in the constitutive equation by including the characteristic length for each element. The stress-strain response of each element is varied based on the characteristic length of the element, keeping the fracture energy constant. Consequently, there is no need to specify or calibrate the internal length as in the

regularization method. The advantage in using this approach is that it only requires small modifications in the constitutive relations to capture the mesh-independent strain softening behavior.

In recent works, incorporation of creep and damage to model fracture propagation in cementitious materials has been accomplished through a rate-dependent softening model with either linear viscoelasticity in the bulk of the specimen (Zdeněk P. Bažant and Li 1997; Di Luzio 2009) or a time-dependent cohesive model in an elastic solid for crack propagation (Rosa et al. 2012). While these models can be used in specific cases such as in a three-point bending specimen where the behavior of the material under different loading rates is known *a priori*, a generalized creep-damage model is required to model time-dependent fracture in situations where creep and damage properties are obtained separately(Pijaudier-Cabot et al. 2005). The concrete material properties such as elastic modulus, compressive strength and tensile strength are obtained at a certain rate usually specified in the ASTM standards. However, all the damage analysis is done in a time-independent manner. This can work for a range of loading rates similar to the rate at which these properties are estimated. At rates that differ significantly from those test conditions, the results could be entirely different. At lower rates particularly, the creep in the material interferes with the fracture and the strength of the material.

CHAPTER 3

MOOSE

3.1 Background and Overview

MOOSE is a high-performance, open source, C++-based FE framework, with customizable modules for multi-physics simulations (INL). MOOSE is designed to solve large systems of coupled equations simultaneously without using the traditional operator split method (MacNamara and Strang 2016). It utilizes a modular approach, which makes it straightforward to add new models to create new, fully coupled Multiphysics applications tailored to specific purposes (D. R. Gaston et al. 2015). MOOSE employs the Jacobian-free Newton-Krylov (JFNK) solution technique to solve systems of coupled physics equations in a fully coupled, implicit manner. The MOOSE architecture capitalizes on the fact that JFNK implementation requires only residual evaluations of the discrete system. For optimal convergence, the Jacobian-free approach calls for effective preconditioning for optimal convergence. MOOSE provides access to a variety of options for preconditioning to achieve parallel scalability and balanced use of computational resources (Derek Gaston et al. 2009). A relevant example of an application that takes advantage of MOOSE to model specific physical phenomena is the Grizzly code, which is being used to model the evolution of degradation mechanisms in concrete, considering the coupled effects of thermal and moisture transport and mechanical deformation (Huang and Spencer 2016).

3.2 Solving Technique

The Newton-Raphson method is the most popular iterative technique to solve the nonlinear algebraic equations. The residual system of equations of the weak form of the set of the partial differential equations (PDE's) to be solved is given by,

$$\boldsymbol{R_i(u)} = 0 \tag{3.1}$$

where **u** is the solution vector and is approximated as,

$$\boldsymbol{u} = \sum_{j=1}^{N} u_j \varphi_j \tag{3.2}$$

where, φ_j are the shape functions. u_j are the coefficients which are solved in Equation 3.1. In Galerkin finite element method, the number of equations (i in Equation 3.1)) are same as the coefficients to be solved. The coefficients are obtained using the Newton-Raphson's method as follows,

$$\boldsymbol{J(u_n)\delta u_{n+1}} = -\boldsymbol{R(u_n)} \tag{3.3}$$

where, the Jacobian matrix $\boldsymbol{J}(\mathbf{u_n})$ in the current iteration n is given as,

$$\boldsymbol{J_{ij}(u_n)} = \frac{\partial \boldsymbol{R_i(u_n)}}{\partial u_j} \tag{3.4}$$

The updated solution is then given by,

$$\boldsymbol{u_{n+1}} = \boldsymbol{u_n} + \delta \boldsymbol{u_{n+1}} \tag{3.5}$$

The iteration continues until $\mathbf{u_{n+1}} - \mathbf{u_n} < \boldsymbol{\delta_{tol}}$. The problem with Newton method is that for large number of equations (with increasing number of elements in the analysis) and a highly nonlinear problem which converges slowly, the cost of evaluating and storing Jacobian increases.

3.2.1 Krylov Iteration and GMRES

Krylov iterative procedures are used, which do not require the Jacobian matrix but approximates the multiplication of the Jacobian with any vector using a Krylov subspace. To solve $\mathbf{Ax} = \mathbf{b}$, a Krylov subspace is used (Knoll and Keyes 2004),

$$\boldsymbol{K_j = span\left(r_0, Ar_0, A^2 r_0, \ldots, A^{j-1} r_0\right)} \tag{3.1}$$

where $\mathbf{r}_0 = \mathbf{b} - \mathbf{A}\mathbf{x}_0$ are the initial residual vector and the vectors $\boldsymbol{v} = \mathbf{r}_0, \mathbf{A}\mathbf{r}_0, \mathbf{A}^2\mathbf{r}_0, \ldots, \mathbf{A}^{j-1}\mathbf{r}_0$ are called Krylov vectors. Generalized minimum residual method (GMRES) is one of the Krylov iteration scheme which gives an approximate solution $\mathbf{x}_n$ that minimizes Euclidean norm of the residual vector, $\mathbf{r}_\mathrm{n} = \mathbf{b} - \mathbf{A}\mathbf{x}_n$.

3.2.2 Jacobian Free Newton-Krylov Technique

In the JFNK approach, Equation 3.3 is solved by utilizing the Krylov iteration using an initial guess $\delta\boldsymbol{u}_0$. The initial residual vector at a fixed iteration n is then given by,

$$\boldsymbol{r}_0 = -\boldsymbol{R}(\boldsymbol{u}) - \boldsymbol{J}(\boldsymbol{u})\delta\boldsymbol{u_0} \tag{3.2}$$

As per GMRES, the l^{h} Krylov iteration is then given by,

$$\delta\boldsymbol{u}_l = \delta\boldsymbol{u}_0 + \sum_{\boldsymbol{i=0}}^{\boldsymbol{l-1}} \boldsymbol{\beta_j} (\boldsymbol{J})^{\boldsymbol{j}} \boldsymbol{r}_0 \tag{3.8}$$

where, $\boldsymbol{\beta_j}$ are scalars used to minimize the residual. In Equation 3.8, the Jacobian is not explicitly needed but its action on Krylov vectors is required. This is approximated using a finite difference approach (Derek Gaston et al. 2009; Knoll and Keyes 2004).

$$\boldsymbol{J}(\boldsymbol{u})\boldsymbol{v} = \frac{\boldsymbol{R}(\boldsymbol{u} + \varepsilon\boldsymbol{v}) - \boldsymbol{R}(\boldsymbol{u})}{\varepsilon} \tag{3.9}$$

where, ε is a small perturbation. The disadvantage with this approach is that iterations are required to solve any nonlinear problem to advance through a time step.

3.2.3 Preconditioned JFNK

Preconditioning reduces the number of iterations required in Krylov iterations. The traditional preconditioner that are usually used to are Jacobi, ILU and SSOR (D Gaston et al. 2009). Jacobi uses the diagonal of the matrix as the preconditioner, ILU uses splits the original matric into lower and upper triangles while in SSOR the original matrix is split into diagonal, lower and upper triangles.

MOOSE uses right preconditioning, which is given as,

$$(\boldsymbol{J}\boldsymbol{M}^{-1})(\boldsymbol{M}\delta\boldsymbol{u}) = -\boldsymbol{R}(\boldsymbol{u}) \tag{3.10}$$

where, M is the preconditioning matrix. The above equation is solved in two steps

$$(\boldsymbol{J}\boldsymbol{M}^{-1})(\boldsymbol{w}) = -\boldsymbol{R}(\boldsymbol{u}) \tag{3.11}$$

$\boldsymbol{w}$ is obtained in the above equation by a slight modification in equation (3.9) as follows

$$\boldsymbol{J}(\boldsymbol{u})\boldsymbol{M}^{-1}\boldsymbol{v} = \frac{\boldsymbol{R}(\boldsymbol{u} + \varepsilon\boldsymbol{M}^{-1}\boldsymbol{v}) - \boldsymbol{R}(\boldsymbol{u})}{\varepsilon} \tag{3.12}$$

and then $\delta\mathbf{u}$ is obtained as

$$\delta\boldsymbol{u} = \boldsymbol{M}^{-1}\boldsymbol{w} \tag{3.13}$$

3.2.4 Physics Based Conditioner

Preconditioning reduces the number of iterations required in Krylov iterations. The traditional preconditioner that are usually used to are Jacobi, ILU and SSOR (D Gaston et al. 2009). Jacobi uses the diagonal of the matrix as the preconditioner, ILU uses splits the original matric into lower and upper triangles while in SSOR the original matrix is split into diagonal, lower and upper triangles. MOOSE uses right preconditioning, which is given as,

$$(\boldsymbol{J}\boldsymbol{M}^{-1})(\boldsymbol{M}\delta\boldsymbol{u}) = -\boldsymbol{R}(\boldsymbol{u}) \tag{3.3}$$

where, M is the preconditioning matrix. The above equation is solved in two steps

$$(\boldsymbol{J}\boldsymbol{M}^{-\mathbf{1}})(\boldsymbol{w}) = -\boldsymbol{R}(\boldsymbol{u}) \tag{3.4}$$

$\boldsymbol{w}$ is obtained in the above equation by a slight modification in Equation 3.9 as follows

$$\boldsymbol{J}(\boldsymbol{u})\boldsymbol{M}^{-\mathbf{1}}\boldsymbol{v} = \frac{\boldsymbol{R}(\boldsymbol{u} + \varepsilon\boldsymbol{M}^{-\mathbf{1}}\boldsymbol{v}) - \boldsymbol{R}(\boldsymbol{u})}{\varepsilon} \tag{3.16}$$

and then $\delta\mathbf{u}$ is obtained as

$$\delta\boldsymbol{u} = \boldsymbol{M}^{-\mathbf{1}}\boldsymbol{w} \tag{3.5}$$

Moose employs incomplete LU decomposition as default preconditioner.

3.3 Structure of MOOSE

Figure 3-1 illustrates how a few different types of modules to represent specific physical phenomena can be integrated into the MOOSE architecture. MOOSE handles the finite element solution and provides interfaces for a variety of software objects that perform numerical operations or represent physics to be plugged into the system. One of the most commonly used modules, called the Kernel, represents an individual term in the weak form of the partial differential equation (PDE) to be solved. Boundary conditions can also be customized and represent surface terms in the PDE. Material objects compute values at volume or surface integration points, and are used to compute quantities describing local material behavior, which are then used by the kernels (Permann et al. 2019). MOOSE uses the libMesh FE framework(Kirk et al. 2006) to provide core finite element functions, mesh input-output, and interfaces to solver packages. Extensive documentation of the MOOSE framework is available(Slaughter et al. 2015; Permann et al. 2019). MOOSE is made publicly available through GitHub("*Https://Github.Com/Idaholab/Moose"*), which also provides a platform for peer review and testing of all new code contributions.

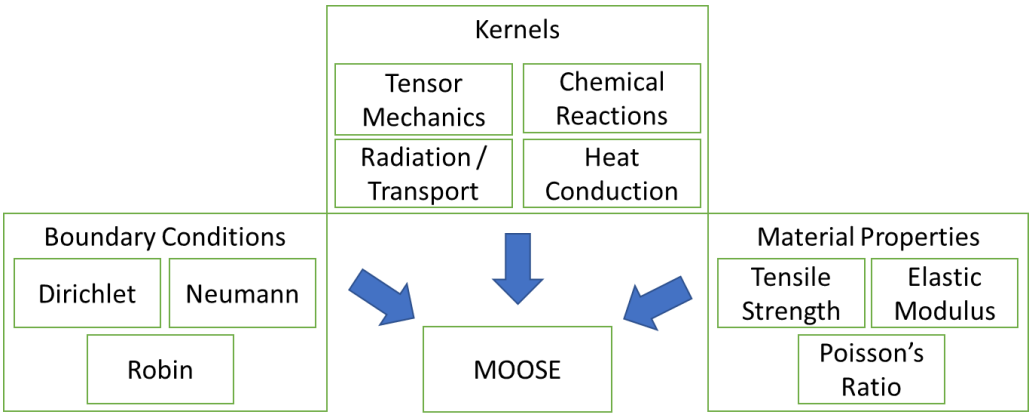

Figure 3-1. Modular Structure of MOOSE, Showing a Few of the Provided Pluggable Interfaces for Defining Physics-Specific Models (Permann et al. 2019)

The kernels, boundary conditions and materials will be explained next using the Tensor Mechanics kernel of MOOSE.

3.3.1 Tensor Mechanics Kernel

The Tensor Mechanics kernel in the MOOSE framework consists of libraries that help to solve mechanics problem. The governing equation when a material deforms under stress is given by,

$$\nabla.(\boldsymbol{\sigma} + \boldsymbol{\sigma}_0) + \boldsymbol{b} = 0 \tag{3.18}$$

with the boundary conditions as

$$\begin{aligned} \boldsymbol{u} &= \boldsymbol{u_p} \\ \boldsymbol{\sigma}.\boldsymbol{n} &= \boldsymbol{t} \end{aligned} \tag{3.19}$$

where, $\boldsymbol{\sigma}$ is the Cauchy stress tensor, $\boldsymbol{\sigma}_0$ is the additional stress, $\boldsymbol{b}$ is the body force, $\boldsymbol{u}$ is the displacement, $\boldsymbol{u_p}$ is the prescribed displacement at the boundary, $\mathbf{n}$ is the unit normal to the boundary and $\boldsymbol{t}$ is the prescribed traction on the boundary. The weak form of Equation 3.18 is given as (neglecting the body force),

$$\int_{\Omega} \nabla\varphi_m(\boldsymbol{\sigma} + \boldsymbol{\sigma}_0) + \int_{\Gamma} \varphi_m \boldsymbol{t} = 0 \tag{3.20}$$

The first term is the kernel while the last term is a boundary condition in the above equation. The first term is handled by *StressDivergenceKernel()* in MOOSE *("Www.Mooseframework.Org: StressDivergenceTensors Class Reference")*. The constitutive model for a linear elastic material is given as:

$$\bar{\boldsymbol{\sigma}} = \bar{\bar{\mathbf{C}}}(\bar{\boldsymbol{\varepsilon}} - \overline{\boldsymbol{\varepsilon_0}}) \tag{3.21}$$

where, $\bar{\boldsymbol{\sigma}}$, $\bar{\bar{\mathbf{C}}}$ and $\bar{\boldsymbol{\varepsilon}}$ are the stress, elasticity tensor and strain tensor respectively, and $\overline{\boldsymbol{\varepsilon_0}}$ is the stress-independent strain. The MOOSE implementation of mechanics uses a modular architecture("Parallel Multiphysics Finite Element Framework") based on the aforementioned Material system, in which $\bar{\boldsymbol{\sigma}}$, $\bar{\bar{\mathbf{C}}}$, $\bar{\boldsymbol{\varepsilon}}$ and $\overline{\boldsymbol{\varepsilon_0}}$ are defined as separate Material objects that can be combined together in a variety of ways to provide the desired behavior. Of these four tensors, the first three are required for any mechanics problem, while the latter one is optional. There are separate base classes for all of these basic types of Material objects, which used together, compute the material behavior at the quadrature points, which can be represented by scalars, vectors, or tensors("Parallel Multiphysics Finite Element Framework"). These values are assigned at each quadrature point. The values are declared inside a kernel easily using declareProperty<TYPE>() syntax. To use a material property, getMaterialProperty<TYPE>() is used inside a kernel or any other object. In some cases, it might be necessary to store the old values of a variable, in that case declarePropertyOld<TYPE>() is used.

3.3.2 Strain Materials Class

The base class to create a second order strain tensor is called *ComputeStrainBase()*. This base class creates a material object total_strain, which must be initialized in the overriding

classes. In case of incremental strains, *ComputeIncrementalBaseclass()* creates a material object strain_increment, rotation_increment etc. which must be overridden in classes inheriting from this class. These properties then become available for all the kernels, materials, boundary conditions etc.

MOOSE has small total strain, small incremental strain and finite incremental strain formulation. These strains are computed as follows

$$\begin{aligned} \boldsymbol{\varepsilon_{st}} &= 0.5(\nabla \boldsymbol{u} + \nabla \boldsymbol{u}^T) \\ \boldsymbol{\varepsilon_{si}} &= 0.5(\boldsymbol{F} + \boldsymbol{F}^T) \\ \boldsymbol{\varepsilon_{Fi}} &= \boldsymbol{D} \times dt \end{aligned} \tag{3.22}$$

where, u is the displacement vector, F is the deformation gradient and $\boldsymbol{D}$ is the stretching rate tensor. dt is the increment of time.

3.3.3 Elasticity Tensor

The base class to create a fourth order elasticity tensor is called *ComputeElasticityTensorBase()*. It creates a material object elasticity_tensor which is to be initiated in the derived class. One such class is called *ComputeElasticityTensor()* which builds the elasticity tensor based on the symmetry required by the user ("Compute Elasticity Tensor|MOOSE").

3.3.4 Stress Materials

The base class to create a second order stress tensor is called *ComputeStressBase* ("Www.Mooseframework.Org: ComputeStressBase Class Reference"). All the overriding class must override the function *computeQPStress*(). A variety of classes are available to compute elastic stress, plastic stress, creep stress, stress using a smeared cracking model, etc. and multiple sources of inelastic strains can be accounted for in the stress calculation with the *ComputeMultipleInelasticStress* ("Parallel Multiphysics Finite Element

Framework") class . In this class, the inelastic strains are computed first using the specified inelastic model. The effective stress is then computed, assuming that the material is undamaged. The effect of damage is then accounted for in the effective stress based on the computed isotropic damage index in the damage class. In the next section, the implementation of the existing creep model in MOOSE will be described.

3.4 Creep Model in MOOSE

Using Newmark finite difference scheme, the constitutive equation for the material described by the generalized Kelvin-Voigt or Maxwell models is given by (A. B. Giorla 2017):

$$\bar{\boldsymbol{\sigma}}^{(\boldsymbol{n+1})} = \bar{\bar{\boldsymbol{C}}}_{\boldsymbol{eq}}^{(n+1)} : \left[\bar{\boldsymbol{\varepsilon}}^{\,(n+1)} - \boldsymbol{\alpha}_{\boldsymbol{eq}}^{(n)}\right] \tag{3.23}$$

where the apparent stiffness tensor $\bar{\bar{\boldsymbol{C}}}_{\boldsymbol{eq}}^{(n+1)}$ and apparent internal strain $\boldsymbol{\alpha}_{\boldsymbol{eq}}^{(n)}$ for a generalized Kelvin-Voigt model are given as (A. B. Giorla 2017):

$$\begin{aligned} \bar{\bar{\boldsymbol{C}}}_{\boldsymbol{eq}}^{(n+1)} &= \left[\bar{\bar{\boldsymbol{C}}}_{\boldsymbol{0}}^{-1} + \sum_{1}^{N}\left[\left(1 + \frac{\eta_i}{\Delta t^{(n+1)}\theta_i}\right)\bar{\bar{\boldsymbol{C}}}_{\boldsymbol{i}}\right]^{-1}\right]^{-1} \\ \boldsymbol{\alpha}_{\boldsymbol{eq}}^{(n)} &= \sum_{1}^{N}\left(\frac{\eta_i}{\Delta t^{(n+1)}\theta_i}\right)\left[\boldsymbol{\alpha}_{\boldsymbol{i}}^{(n)} + \Delta t^{(n+1)}(1-\theta_i)\dot{\boldsymbol{\alpha}}_{\boldsymbol{i}}^{(n)}\right] \end{aligned} \tag{3.24}$$

For a generalized Maxwell model, the corresponding expressions are (A. B. Giorla 2017):

$$\begin{aligned} \bar{\bar{\boldsymbol{C}}}_{\boldsymbol{eq}}^{(n+1)} &= \bar{\bar{\boldsymbol{C}}}_{\boldsymbol{0}} + \sum_{1}^{N}\left[\left(\frac{1}{1 + \frac{\eta_i}{\Delta t^{(n+1)}\theta_i}}\right)\bar{\bar{\boldsymbol{C}}}_{\boldsymbol{i}}\right] \\ \boldsymbol{\alpha}_{\boldsymbol{eq}}^{(n)} &= \left[\bar{\bar{\boldsymbol{C}}}_{\boldsymbol{eq}}^{(n+1)}\right]^{-\mathbf{1}} : \sum_{1}^{N}\bar{\bar{\boldsymbol{C}}}_{\boldsymbol{i}} : \left(\frac{\frac{\eta_i}{\Delta t^{(n+1)}\theta_i}}{1 + \frac{\eta_i}{\Delta t^{(n+1)}\theta_i}}\right)\left[\boldsymbol{\alpha}_{\boldsymbol{i}}^{(n)} + \Delta t^{(n+1)}(1-\theta_i)\dot{\boldsymbol{\alpha}}_{\boldsymbol{i}}^{(n)}\right] \end{aligned} \tag{3.25}$$

where $\boldsymbol{\alpha_i}$ and $\boldsymbol{\dot{\alpha}_i}$ are the strain and strain rate in the $\boldsymbol{i^{th}}$ viscous dashpot ($\boldsymbol{i}$ ranging from 1 to N). $\overline{\overline{\boldsymbol{C}}}_{\boldsymbol{0}}$ and $\overline{\overline{\boldsymbol{C}}}_{\boldsymbol{i}}$ are the elasticity tensors of the standalone and $\boldsymbol{i^{th}}$ spring in the Kelvin-Voigt or Maxwell chains. η_i is the characteristic time, which defines viscosity of the dashpot ($\overline{\overline{\boldsymbol{E}}}_{\boldsymbol{i}}$) as:

$$\overline{\overline{\boldsymbol{E}}}_{\boldsymbol{i}} = \eta_i \overline{\overline{\boldsymbol{C}}}_{\boldsymbol{i}} \tag{3.26}$$

θ_i is a numerical parameter to control the convergence properties of the finite difference scheme. For unconditional convergence, $\theta_i \geq 0.5$. $\Delta t^{(n+1)}$ is the change between the current and previous time step.

The elasticity tensor of the material is given as:

$$\begin{aligned} \overline{\overline{\boldsymbol{C}}}_{\boldsymbol{orig}} &= \overline{\overline{\boldsymbol{C}}}_{\boldsymbol{0}} \qquad for\ Kelvin - Voigt\ model \\ \overline{\overline{\boldsymbol{C}}}_{\boldsymbol{orig}} &= \sum_{\boldsymbol{i=0}}^{\boldsymbol{N}} \overline{\overline{\boldsymbol{C}}}_{\boldsymbol{i}} \qquad for\ Maxwell\ model \end{aligned} \tag{3.27}$$

For aging materials such as concrete, the spring elasticities and dashpot viscosities are time dependent. Once the apparent stiffness and apparent internal strain are known, the actual creep strain increment is estimated as (A. B. Giorla 2017):

$$\Delta \bar{\boldsymbol{\varepsilon}}_{\boldsymbol{cr}}^{(n+1)} = \bar{\boldsymbol{\varepsilon}}_{\boldsymbol{mech}}^{(n+1)} - \left[\overline{\overline{\boldsymbol{C}}}_{\boldsymbol{orig}}^{(-1)} : \overline{\overline{\boldsymbol{C}}}_{\boldsymbol{eq}}^{(n+1)}\right] : \left[\bar{\boldsymbol{\varepsilon}}^{\,(n+1)} - \boldsymbol{\alpha}_{\boldsymbol{eq}}^{(n)}\right] - \bar{\boldsymbol{\varepsilon}}_{\boldsymbol{cr}}^{(n)} \tag{3.28}$$

The stress increment is computed as:

$$\boldsymbol{\Delta \bar{\sigma}^{(n+1)}} = \overline{\overline{\boldsymbol{C}}}_{orig} \boldsymbol{\Delta \bar{\varepsilon}_{cr}^{(n+1)}} \tag{3.29}$$

The effective stress is then computed as:

$$\boldsymbol{\bar{\sigma}^{(n+1)}} = \boldsymbol{\bar{\sigma}^{(n)}} + \overline{\overline{\boldsymbol{C}}}_{orig} \boldsymbol{\bar{\varepsilon}_{inc}} - \boldsymbol{\Delta \bar{\sigma}^{(n+1)}} \tag{3.30}$$

The details of the derivation are available in (A. B. Giorla 2017).

3.5 Hygro-Thermal Model in MOOSE

As stated in Section 2.1.2, the two partial differential equation to be solved for coupled hygro-thermal analysis are as follows:

$$\rho C \frac{\partial T}{\partial t} = \nabla(\mathrm{k}\nabla \mathrm{T}) + C_w \mathrm{J}\nabla \mathrm{T} + C_a \frac{\partial W}{\partial H}\frac{\partial H}{\partial t} + Q \tag{3.31}$$

$$\frac{\partial W}{\partial H}\frac{\partial H}{\partial t} = \nabla(\mathrm{D}_h \nabla \mathrm{H}) + \nabla(\mathrm{D}_{ht}\nabla \mathrm{T}) + \frac{\partial W_d}{\partial t} \tag{3.32}$$

The individual components for the weak form are the kernels (in MOOSE terminology) to be solved. In the equations above, the isobaric heat capacity of water is given by,

$$C_w = 350000(374.15 - T)^{\frac{1}{3}} \tag{3.33}$$

The empirical relation developed for cement paste mix is given by,

$$W = \frac{CkV_m H}{(1 - kH)[1 + (c-1)kH]} \tag{3.34}$$

where, W is the quantity of vapor absorbed (g/g of cement paste). V_m is the mass of adsorbate required to cover the adsorbent with a single molecular layer. It is given by the following relation with V_t, V_{wc}, and V_{ct} denoting the age of mix, water cement ratio and cement type.

$$V_m = V_t V_{wc} V_{ct} \tag{3.35}$$

The three constants are given by,

$$V_t = \begin{cases} 0.068 - \dfrac{0.22}{t} & t > 5\ days \\ V_t(5) & t \leq 5\ days \end{cases} \tag{3.36}$$

$$V_{wc} = \begin{cases} 0.85 + \dfrac{0.45w}{c} & 0.3 < \dfrac{w}{c} > 0.7 \\ V_{wc}(0.3) & \dfrac{w}{c} \leq 0.3 \end{cases} \tag{3.37}$$

$$V_{ct} = \begin{cases} 0.9 & \text{Type I cement} \\ 1 & \text{Type II cement} \\ 0.85 & \text{Type III cement} \\ 0.6 & \text{Type IV cement} \end{cases} \tag{3.38}$$

C and k are empirical constant which are given by,

$$C = \exp\left(\frac{855}{T + 273.15}\right) \tag{3.39}$$

$$k = 0 \leq \left(\frac{(n-1)C - 1}{n(C-1)}\right) \leq 1 \tag{3.40}$$

where, n depends upon the same factors as V_m and is expressed as,

$$n = N_t N_{wc} N_{ct} \tag{3.41}$$

with the constants given as below,

$$N_t = \begin{cases} 2.5 + \dfrac{1.5}{t} & t > 5\ days \\ 5.5 & t \leq 5\ days \end{cases} \tag{3.42}$$

$$N_{wc} = \begin{cases} 0.33 + \dfrac{2.2w}{c} & 0.3 < \dfrac{w}{c} > 0.7 \\ N_{wc}(0.3) & \dfrac{w}{c} \leq 0.3 \\ N_{wc}(0.7) & \dfrac{w}{c} \geq 0.7 \end{cases} \tag{3.43}$$

$$N_{ct} = \begin{cases} 1.1 & \text{Type I cement} \\ 1 & \text{Type II cement} \\ 1.15 & \text{Type III cement} \\ 1.5 & \text{Type IV cement} \end{cases} \tag{3.44}$$

More details about the implementation could be found in (Huang and Spencer 2016).

CHAPTER 4

CREEP DAMAGE MODEL THEORY AND NUMERICAL IMPLEMENTATION

The coupled creep-damage model for concrete is implemented in this work within the framework of MOOSE, a finite element environment developed by Idaho National Laboratory, for the solution of coupled multiphysics problems. The developed framework can be augmented with additional features such as a bilinear softening model (Hoover and Bažant 2014) or a nonlocal continuum approach for strain softening (Zdeněk P. Bažant and Lin 1988; Pijaudier-Cabot and Bažant 1987). In *ComputeMultipleInelasticStress* ("Parallel Multiphysics Finite Element Framework") class, the inelastic strains are computed first using the specified inelastic model. The effective stress is then computed, assuming that the material is undamaged. The effect of damage is then accounted for in the effective stress based on the computed isotropic damage index in the damage class. In the next section, the theory and implementation of the damage class will be described.

4.1 Damage Model

Damage is characterized in this work by an isotropic damage (scalar) variable d such that the stress in the body can be expressed as: (Kurumatani et al. 2016; Giorla Alain B., Le Pape Yann, and Dunant Cyrille F. 2017)

$$\bar{\boldsymbol{\sigma}} = \left(1 - d(\kappa)\right)\bar{\bar{\boldsymbol{C}}} : \bar{\boldsymbol{\varepsilon}}_{\boldsymbol{el}} \tag{4.1}$$

where, $\bar{\boldsymbol{\sigma}}$, $\overline{\boldsymbol{\varepsilon}_{\boldsymbol{el}}}$, and $\bar{\bar{\boldsymbol{C}}}$ are the second order stress and elastic strain tensors, and fourth-order elasticity tensor, respectively. The value of the damage parameter $d(\kappa)$ ranges from 0 for an undamaged specimen to 1.0 for a completely damaged specimen and is a function of the state variable κ used to describe the evolution of damage. κ captures the strain history in the material up to a considered instant of time. The underlying assumption is that the

material remains isotropic even after the damage has occurred. This assumption is valid for highly heterogeneous materials like concrete (Kurumatani et al. 2016; Pijaudier-Cabot and Mazars 2001; Fichant, La Borderie, and Pijaudier-Cabot 1999) since the random orientation of pores and defects present in the pristine material as well as in the damaged state makes it difficult to quantify damage as a function of orientation as is done for typical composite materials (Khaled et al. 2019). A simplifying assumption is made in this case that damage results in a reduction in the Young's modulus of the specimen. Such an isotropic model has been used to predict damage in uniaxial and mixed mode fracture cases (Kurumatani et al. 2016; Pijaudier-Cabot and Mazars 2001; C Mazzotti and Savoia 2001). However, damage-induced anisotropy should be considered in problems where failure occurs due to multiaxial extensions (Fichant, La Borderie, and Pijaudier-Cabot 1999).

The evolution of damage depends on how stress decays with strain increment in the post-peak region and occurs only when the equivalent strain, $\varepsilon_{eq} > \kappa$ with κ either increasing or remaining constant. In a one-dimensional case, this strain is the maximum principal strain. However, expanding it to a three-dimensional case requires the use of a strain invariant that is a function of the components of the strain tensor. The equivalent strain has been defined in multiple ways (de Vree, Brekelmans, and van Gils 1995; Mazars 1986; Mazars, Hamon, and Grange 2015). In this study, a modified von Mises strain is used as the equivalent strain (de Vree, Brekelmans, and van Gils 1995)'(Kurumatani et al. 2016), and is defined as:

$$\kappa = \varepsilon_{eq} = f(\bar{\boldsymbol{\varepsilon}}_{\boldsymbol{el}}) = \frac{k-1}{2k(1-2\nu)} I_1 + \frac{1}{2k}\sqrt{\left(\frac{k-1}{1-2\nu} I_1\right)^2 + \frac{12k}{(1+\nu)^2} J_2} \qquad (4.2)$$

where ν, k are the Poisson's ratio and the ratio of compressive to tensile strength, respectively. I_1 and J_2 are the first and second invariants of elastic strain, $\bar{\boldsymbol{\varepsilon}}_{\boldsymbol{el}}$ and the elastic strain deviator tensor, and are given as:

$$I_1 = \varepsilon_{xx} + \varepsilon_{yy} + \varepsilon_{zz} \tag{4.3}$$

$$J_2 = \frac{1}{3}\left(\varepsilon_{xx}^2 + \varepsilon_{yy}^2 + \varepsilon_{zz}^2 - \varepsilon_{xx}\varepsilon_{yy} - \varepsilon_{yy}\varepsilon_{zz} - \varepsilon_{xx}\varepsilon_{zz} + 3\left(\varepsilon_{xy}^2 + \varepsilon_{yz}^2 + \varepsilon_{xz}^2\right)\right) \tag{4.4}$$

Mazars has proposed an alternate definition of equivalent strain (Pijaudier-Cabot and Mazars 2001) as:

$$\varepsilon_{eq} = \sqrt{\sum_{i=1}^{3} \langle \varepsilon_i \rangle^2} \tag{4.5}$$

where $\langle \varepsilon_i \rangle$ are the tensile components of principal strain. While Mazars's equivalent strain appears to be more intuitive, numerical results show that this approach overestimates the peak and post-peak response in comparison to the experimental results, as shown later in this document.

Considering that stress decays in an exponential manner with strain (Gopalaratnam and Shah 1985), the damage evolution can be stated as:

$$d(\kappa) = 1 - \frac{\kappa_0}{\kappa} \mathrm{e}^{-\beta(\kappa - \kappa_0)} \tag{4.6}$$

where κ_0, β are the equivalent strain at which cracking begins and the initial slope of exponential softening (Figure 4-1), respectively. β controls the shape of the exponential softening. A higher value implies sudden failure (low fracture energy) while a lower value implies gradual softening (higher fracture energy). Thus, β depends on the fracture energy

of the specimen. The fracture energy is therefore taken as a material property. Mathematically, it can be stated as:

$$G_F = \int_0^{\infty} \sigma \partial w \tag{4.7}$$

where w is the crack opening displacement, which is a function of the characteristic length h_{ce} given by:

$$w = (\kappa - \kappa_0) h_{ce} \tag{4.8}$$

In finite element analysis, the characteristic length is generally related to the size of a typical element(Kurumatani et al. 2016) as:

$$h_{ce} = \begin{cases} \sqrt[2]{2A_e} & for\ triangle\ elements \\ \sqrt[2]{A_e} & for\ quadrilateral\ elements \\ \sqrt[3]{5V_e} & for\ tetrahedral\ elements \\ \sqrt[3]{V_e} & for\ hexahedral\ elements \end{cases} \tag{4.9}$$

where, A_e and V_e are the area and volume respectively of each finite element under consideration. The coefficients 2 and 5 in Eq. (10) implies that at least two triangles are required to form a quadrilateral and at least five tetrahedrons are required to form a hexahedron. Substituting Eq. (9) in (8), we have: (Kurumatani et al. 2016)

$$G_F = \int_0^{\kappa_f} \sigma h_{ce} \partial(\kappa) \tag{4.10}$$

Using the assumption of exponential decay of stress as described earlier, the fracture toughness can be restated as:

$$G_F = \frac{E \kappa_0 h_{ce}}{\beta} \tag{4.11}$$

To handle potential convergence problems in the softening region, a lower limit is set for the residual strength (σ_{res}) of the material (see Figure 4-1). The limiting value of equivalent strain is set as:

$$\kappa_{lim} = \kappa_0 - \frac{1}{\beta}\ln\left(\frac{\sigma_{res}}{f_t}\right) \tag{4.12}$$

If $\kappa > \kappa_{lim}$, damage is recomputed using the following equation:

$$d(\kappa) = 1 - \frac{\sigma_{res}}{E\kappa} \tag{4.13}$$

Once the damage is computed, f_y is determined as:

$$f_y = \max\left(f_t e^{-\beta(\kappa-\kappa_0)}, \sigma_{res}\right) \tag{4.14}$$

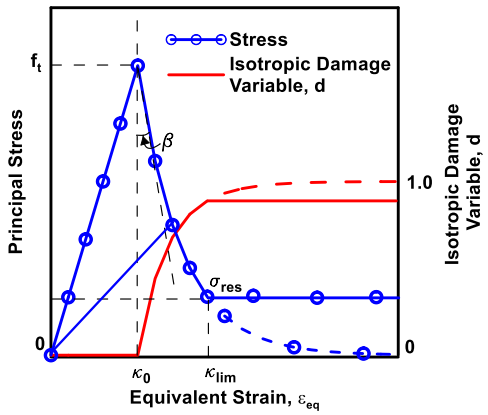

Figure 4-1. Damage Evolution Based on Exponential Decay of Stress

4.2 Creep-Damage Model

In the proposed creep-damage formulation, the total strain is decomposed into individual contributing parts as shown in Eq. (16).

$$\begin{aligned}\bar{\boldsymbol{\varepsilon}}(t) &= \bar{\boldsymbol{\varepsilon}}_{\boldsymbol{el}}(t) + \bar{\boldsymbol{\varepsilon}}_{\boldsymbol{cr}}(t) + \bar{\boldsymbol{\varepsilon}}_{\mathbf{0}}(t) \\ &= \bar{\boldsymbol{\varepsilon}}_{\boldsymbol{mech}}(t) + \bar{\boldsymbol{\varepsilon}}_{\mathbf{0}}(t)\end{aligned} \tag{4.15}$$

where, $\bar{\boldsymbol{\varepsilon}}(t)$is the total strain tensor, $\bar{\boldsymbol{\varepsilon}}_{\boldsymbol{el}}(t), \bar{\boldsymbol{\varepsilon}}_{\boldsymbol{cr}}(t)$ and $\bar{\boldsymbol{\varepsilon}}_{\mathbf{0}}(t)$ are the elastic strain, creep strain and stress-independent eigenstrain tensors, respectively. The eigenstrain includes

stress-independent inelastic strains, e.g., thermal and shrinkage strains. The sum of the elastic and creep strains is denoted as the mechanical strain $\bar{\boldsymbol{\varepsilon}}_{\boldsymbol{mech}}(t)$.

Once the creep strain is known, the stress is computed per Eq. (2) as:

$$\bar{\boldsymbol{\sigma}} = \big(1 - d(\kappa)\big)\bar{\bar{\boldsymbol{C}}} : [\bar{\boldsymbol{\varepsilon}} - \bar{\boldsymbol{\varepsilon}}_{\boldsymbol{cr}} - \bar{\boldsymbol{\varepsilon}}_{\mathbf{0}}\,] \tag{4.16}$$

In damage computations, it is assumed that a fraction of the creep strain also causes damage (C Mazzotti and Savoia 2001; Pijaudier-Cabot et al. 2005). Thus, the equivalent strain in Eq. (3) becomes

$$\kappa = \varepsilon_{eq} = f(\bar{\boldsymbol{\varepsilon}}_{\boldsymbol{el}} + \beta' \bar{\boldsymbol{\varepsilon}}_{\boldsymbol{cr}}) \tag{4.17}$$

where β' is termed as the creep-damage parameter. β' is a multiplier to account for the influence of creep strain on damage. A value of 1.0 for β' implies very strong coupling where all the creep strain contributes to damage, whereas a value of 0 implies that creep strain does not contribute to damage.

4.3 Implementation of the Creep-Damage Model in MOOSE

In this work, a new class that computes stress using the assumptions as stated in the description of the damage model was created and added to the MOOSE framework. The algorithm developed for creep-damage implementation is described below.

Step 1. Input the elastic material parameters, i.e., E and ν, and the fracture parameters, i.e., G_F, f_t and σ_{res}.

Step 2. Compute $\bar{\bar{\boldsymbol{C}}}^{\boldsymbol{orig}}$ using E and ν. This is computed in the *ComputeIsotropicElasticityTensor* class. The strain increment is computed using the *ComputeIncrementalSmallStrain* class as shown in Eq. (20).

Step 3. Initialize $\bar{\bar{\boldsymbol{C}}}^{\boldsymbol{d}} = \bar{\bar{\boldsymbol{C}}}^{\boldsymbol{orig}}$, $d = 0$, and $f_y = f_t$ and crack_flag = 0 at the current time step; crack_flag = 0 denotes that cracking has not occurred.

Step 4. Add the strain increment to the previous value to get the total strain. This is implemented in the *ComputeMultipleInelasticStress* class.

Step 5. If the damage parameter, d_{n-1}, and the tensile strength are greater than zero, then update the elasticity tensor using the value of damage in the previous state as:

$$\bar{\bar{\boldsymbol{C}}}_{\boldsymbol{n}}^{\boldsymbol{d}} = (\mathbf{1} - \boldsymbol{d}_{\boldsymbol{n-1}})\bar{\bar{\boldsymbol{C}}}^{\boldsymbol{orig}} \tag{4.18}$$

Step 6. The effective stress as computed in Eq. (28) is also updated based on previous damage state as follows:

$$\bar{\boldsymbol{\sigma}}^{(\boldsymbol{n+1})} = (\mathbf{1} - \boldsymbol{d}_{\boldsymbol{n-1}})\bar{\boldsymbol{\sigma}}^{(\boldsymbol{n+1})} \tag{4.19}$$

Step 7. Compute the maximum principal stress from the updated stress tensor. If the value of the equivalent strain is greater than f_y/E and cracking has occurred for the first time, then κ_0 is specified as the equivalent strain and crack_flag is set to 1. The damage value is updated using Eq. (7) and (14), and f_y using Eq. (15). Else, if crack_flag = 1 and loading is increased, $\kappa_n > \kappa_{n-1}$, the damage value is updated and f_y is computed. To account for creep-induced damage, the value of κ is computed using Eq. (18).

Per steps 5 and 6, the elasticity tensor and the stress are dependent on the previous state of damage. The stress is not corrected further after computing damage in the current time step as it leads to convergence issues. The downside of this approach is that the solution depends on the time step between two iterations. The error increases with larger time steps. Thus, a small-time step is chosen to ensure convergence to the correct solution. This algorithm is shown in the form of a flowchart in Figure 4-2. In this work, the steps in the isotropic damage block in Figure 4-2 are implemented in the new class.

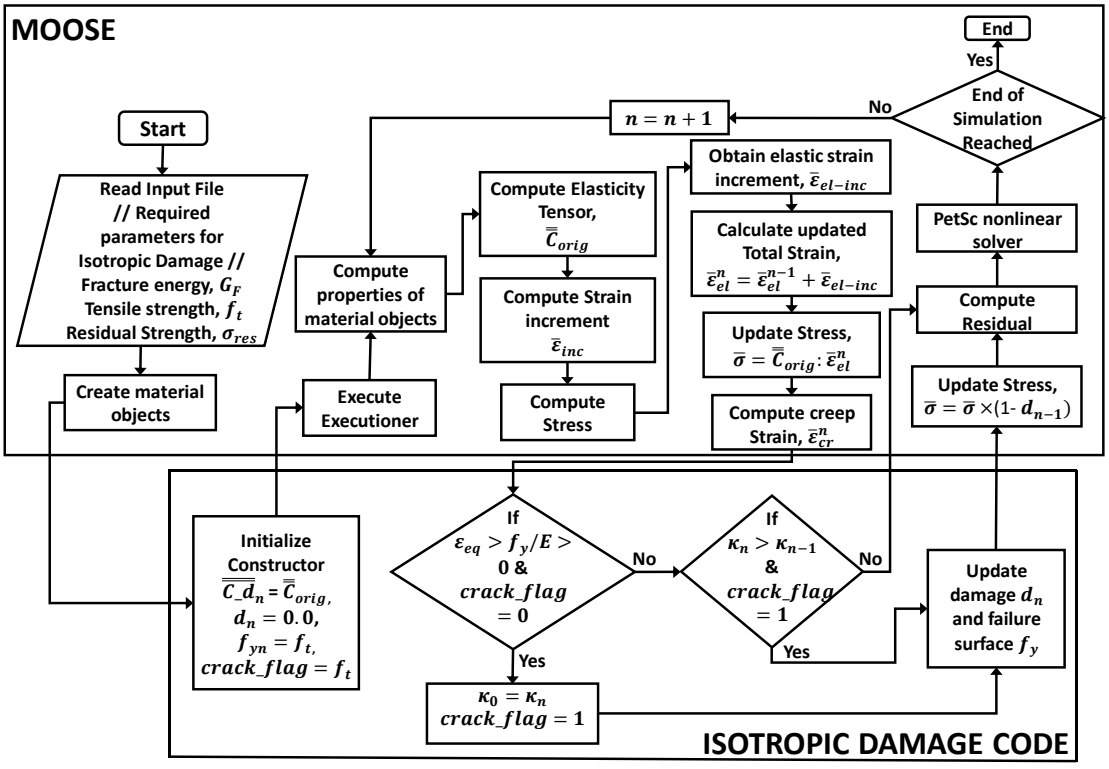

Figure 4-2. Flowchart for the Isotropic Damage Model Implemented in MOOSE

4.4 Verification of Numerical Model

Three verification tests to ascertain whether the constitutive model for isotropic damage has been implemented correctly are described in this section. The first test consists of a single element loaded in tension in a displacement-controlled manner and then unloaded to evaluate its response during unloading, loading in compression, unloading and finally reloading in tension. The second test consists of a simple shear test in which displacement-controlled loading is applied. In the last test, convergence behavior of the algorithm is verified. In these tests, the simulation results are verified against the analytical curve which is obtained outside of MOOSE using the input properties.

4.4.1 Uniaxial Tension-Compression

Model: A single element of size 50 x 50 x 50 mm is loaded in a displacement-controlled manner in tension, unloaded, and then loaded in compression, unloaded, and finally reloaded in tension. Figure 4-3(a) shows the boundary conditions. The displacement-controlled loading was applied in the Z-direction as shown in Figure 4-3(b) and details of the applied displacement history are provided in Table 4-1. The material properties are specified in Table 4-2.

Table 4-1. Applied Displacement With Time

Pseudo Time (s)	0	30	40	50	60	70
Applied displacement (mm)	0	0.04	0	-0.25	0	0.07

Table 4-2. Material Properties for Use in Uniaxial Verification Test

Property	Elastic Modulus, E (same in tension and compression)	Poisson's Ratio, ν	Tensile Strength, f_t	Fracture Energy, G_F
Value	20000 N/mm^2	0.2	3 MPa	0.1 N-mm/mm^2

Results: Figure 4-3(c) shows the analytical curve and the response computed by the algorithm. The analytical curve is estimated by computing β based on the input fracture energy (see Eq. (12)). For the uniaxial case, κ_0 is equal to G_F/E and is equal to 0.00015. During this initial segment of the loading history, the stress is computed using Eq. (2) and (7). As the loading is unidirectional, the maximum principal stress decays in the same manner as the input curve as shown in Figure 4-3(c). Once the direction of applied displacement is reversed, the specimen unloads with the damaged modulus which in this case is 1420 N/mm^2. The specimen then starts to load in compression with the same modulus. The implemented model adequately reproduces the material's tensile stress-strain softening behavior as shown. The strain shown in Figure 4-3(c) is the strain in the zz

direction, which is the maximum tensile and compressive strain for this case. The strains in the xx and yy directions are lower due to Poisson's effect while all the shear strains are zero (not shown here).

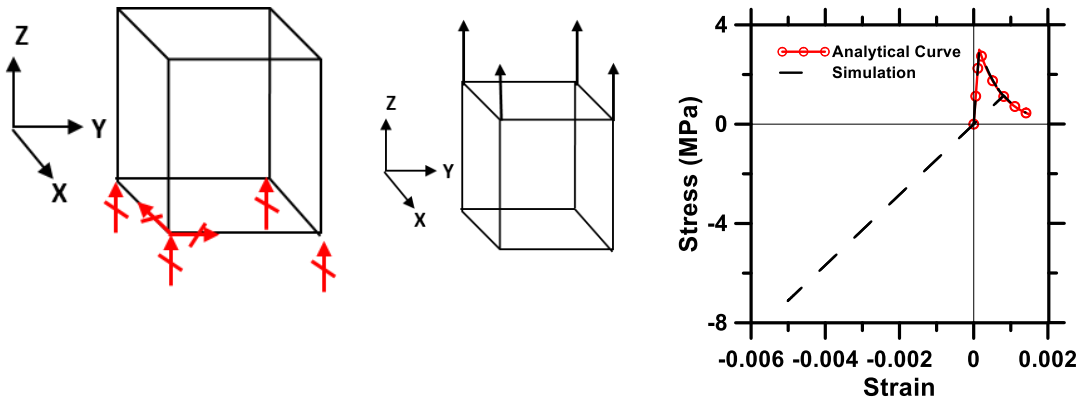

(a) (b) (c)

Figure 4-3. FE Model for Uniaxial Loading, Showing a Single Element With: (a) Boundary Conditions, (b) Loading Conditions, and (c) Computed Stress-Strain Response

4.4.2 Simple Shear

Model: A single element of size 50 x 50 x 50 mm was loaded in simple shear by applying displacement in the X-direction for the nodes lying at z = 50. The boundary conditions and applied displacement are shown in Figures 4-4(a) and 4-4(b) respectively. The applied displacement is increased from 0 to 0.5 mm in 100 s (pseudo time). The material properties shown in Table 4-2 are used here.

Results: Once the maximum principal stress is reached, the element starts degrading based on the exponential evolution law specified earlier. The evolution of damage is computed by estimating the equivalent cracking strain at which the degradation starts (κ_0 in Eq. (7)) and then using Eq. (7) to compute the damage.

For an isotropic material, the shear stress is given as:

$$\tau = \frac{E}{2(1+\nu)}(2\varepsilon) \tag{4.20}$$

where, τ and ε are the shear stress and strain respectively. Under simple shear, the maximum principal stress will be equal to the shear stress at a plane inclined at 45°. Substituting τ as 3 MPa and E and ν as given in Table 4-2 gives ε as 0.00018, J_2 as 3.24 x 10^{-8} (Eq. (5)) and κ_0 as 8.22 x 10^{-5}(Eq. (3)). The damage evolution as a function of equivalent strain is plotted in Figure 4-4(c). As shown in this figure, the simulated curve matches the analytical curve, demonstrating that the predicted damage evolution with equivalent strain is accurate. In this case, all the strains except that in the xz direction are observed to be zero (not shown here).

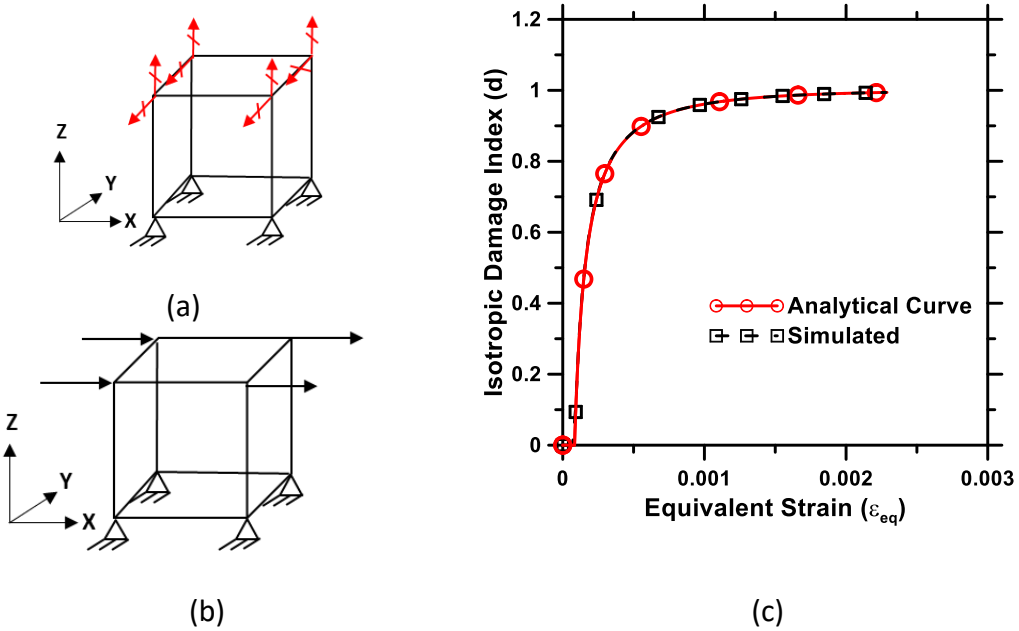

Figure 4-4. FE model for Simple Shear Showing a Single Element With: (a) Boundary Conditions, (b) Loading Conditions, and (c) Damage Evolution With the Equivalent Strain

4.5 Time Convergence

Model: A single element of size 50 x 50 x 50 mm was loaded in a displacement-controlled manner in tension, unloaded and then loaded in compression, unloaded, and finally reloaded in tension. The simulations were carried out with time steps of 1, 0.1 and 0.05 s.

Results: The results of the simulations are shown in Figure 4-5. Decreasing the time step is found to result in convergence with little difference noted in the response for time steps of 0.1 s and 0.05 s. As described earlier, the stress is not corrected to account for damage in the current time step as it leads to convergence issues. To account for such effects, the time step is decreased. A time step of 0.1 s is found to be satisfactory, and hence used in this simulation. A similar convergence analysis was performed for all the remaining verification and validation tests and the optimal time steps used in the simulations are reported along with the simulation results.

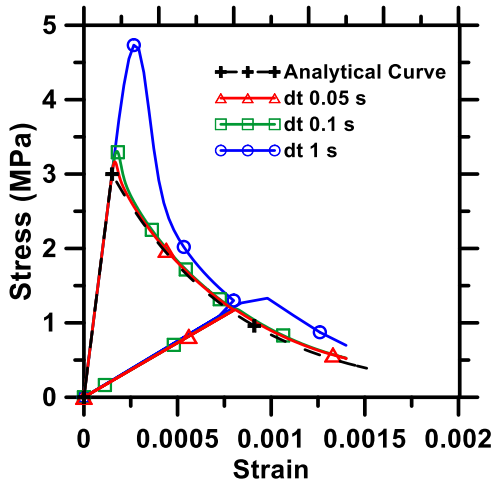

Figure 4-5. Uniaxial Tensile Stress-Strain Response as a Function of Different Time Steps: dt = 0.05, 0.1 and 1 s

4.6 Verification Tests for Creep-Damage Interaction

Three verification tests for the coupled creep-damage algorithm are discussed in this section. The intention of the verification tests is to examine if the creep-damage algorithm can predict the appropriate material behavior that is established through experiments. Only a qualitative assessment is made in this section while quantitative assessment and validation of creep-damage algorithm are carried out in a later section.

4.6.1 Effect of Creep Damage Parameter

Model: A single element of unit size is loaded in a displacement-controlled manner. The loading and boundary conditions are shown in Figures 8(a) and (b). The applied displacement is varied linearly with time, reaching a displacement of 0.002 mm in 10 seconds. The material properties are shown in Table 4-3. The material is defined by a generalized Maxwell model with nine Maxwell units and a standalone spring, the properties of which are given in Table 4-3. The Maxwell material properties were calibrated from the BP model in (Zdeněk P. Bažant, 1988) using the rate type creep formulation (Zdeněk P. Bažant and Wu 1974). The relaxation function using the BP model is given as:

$$R(t,t_1)=\frac{1}{J(t,t_1)}=\frac{E_0}{1+\varphi[(t')^{-m}+\alpha](t-t')^n} \tag{4.21}$$

where $R(t,t_1)$,$J(t,t')$ and E_0 are the relaxation function, creep compliance function and initial elastic modulus, t and t_1 are the current time and the time at which relaxation started, m =1/3, n =1/8, α=0.05, φ=3 are the fitting parameters for the BP model. Three different β' values: 0, 0.5 and 1.0 are used in the simulations.

Table 4-3. Material Properties for Use in Identifying the Influence of Creep Damage Parameter

Property	**Value**			
Elastic Modulus, E_0 (same in tension and compression)	56000 N/mm^2			
Poisson's Ratio, ν	0.2			
Modulus and corresponding characteristic time of each unit in the Maxwell model	7070	MPa	0.0001	s
	560	MPa	0.01	s
	6930	MPa	1	s
	5910	MPa	100	s
	8690	MPa	1.00E+04	s
	7550	MPa	1.00E+06	s
	6810	MPa	1.00E+08	s

	4650	MPa	1.00E+10	s
	3250	MPa	1.00E+12	s
	4580	MPa	∞	s
Tensile Strength, f_t	4.0 MPa			
Fracture Energy, G_F	0.001 N-mm/mm^2			

Results: Figure 8(c) shows the average stress-strain response of the specimen. The stresses and the strains are the average of the values obtained from all the eight quadrature points. The optimal time step for this case was found to be 0.01 s.

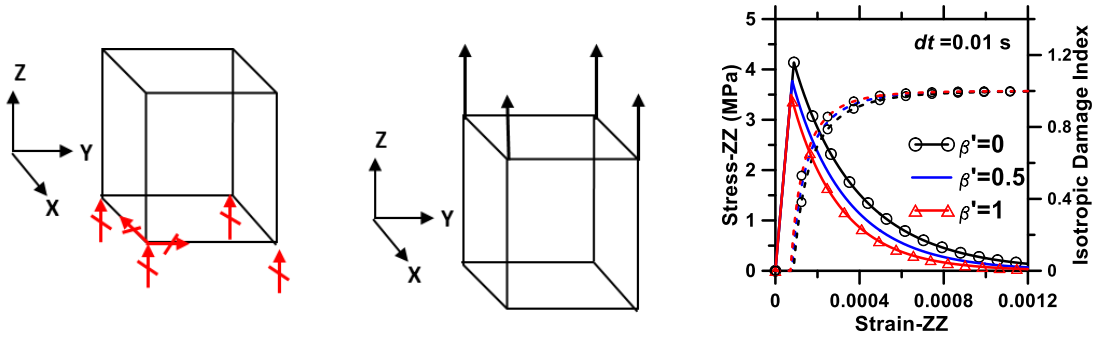

(a) (b) (c)

Figure 4-6. FE Model Showing a Single Element With: (a) Boundary Conditions, (b) Loading Conditions, and (c) Uniaxial Tensile Stress-Strain Response (Solid Lines) and the Crack Damage Parameter (Dashed Lines).

It is evident that that a non-zero value of the parameter β' increases the damage in the specimen, indicated by the reduction in the peak and post-peak stresses. As described earlier, the resulting damage will be underestimated if β' is taken as zero as multiple studies have shown that creep strain also causes damage in the specimen, especially when the tertiary creep region is reached (C Mazzotti and Savoia 2001; Claudio Mazzotti and Savoia 2003; Omar et al. 2009; ZDENEK P. Bažant 1995).

Furthermore, using the same model, instead of displacement, load is applied. The loads correspond to a stress of 3.0 MPa which is 75% of the tensile strength of the material.

Figure 4-7 shows the variation of strain with time. The time step used for this case was 0.1 s. A coupled creep-damage algorithm with β' equal to a non-zero value captures the tertiary creep region and imminent failure at a stress lower than the tensile strength, which would not be possible with an uncoupled algorithm as shown in this figure when β' is taken as zero.

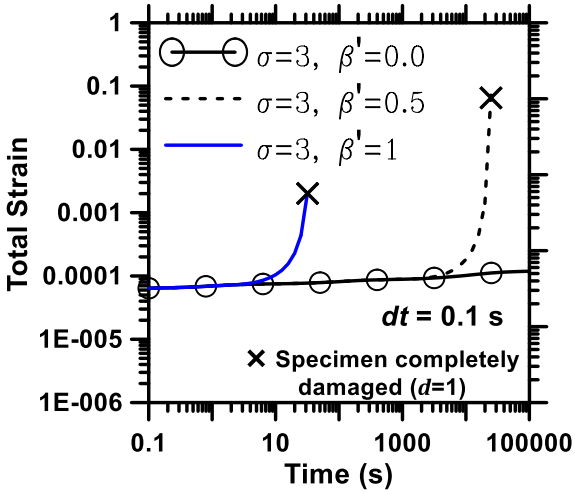

Figure 4-7. Total Strain as a Function of Time With a Constant Stress Applied on One Face, and Different Imposed Crack-Damage Parameters.

4.6.2 Effect of Rate of Loading

Model: The same model and boundary conditions used in the test explained in the previous section are used here, but with varying loading rates. Two cases have been analyzed – in the first case, the maximum displacement of 0.002 mm is reached in 10 s, and in the second case, in 10000 s. The creep damage parameter β' is taken as 0.5 in both the cases.

Results: Figure 4-8 shows the stress-strain response, averaged from all eight quadrature points in the single element.

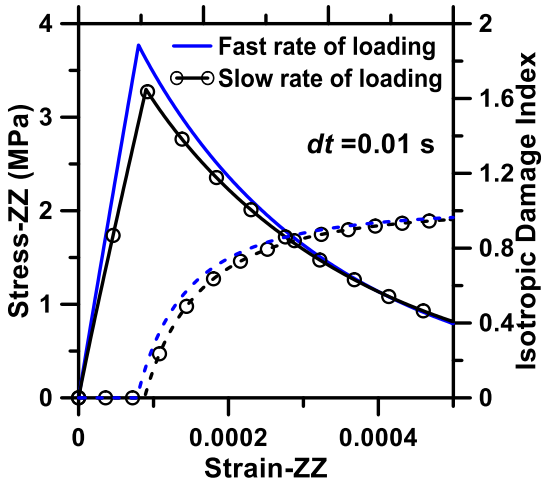

Figure 4-8. Uniaxial Tensile Stress-Strain Response (Solid Lines) and Isotropic Damage Parameter Evolution (Dashed Lines) for Different Rates of Loading.

The effect of loading rate on the tensile strength of the specimen is evident. A slower loading rate results in specimen failure at lower stress levels, which is in line with reported results(Zdenek P. Bažant and Gettu 1992; "Researches Toward a General Flexural Theory for Structural Concrete" 1960). Due to the damage induced by a relatively higher creep strain for slowly applied loading, the total fracture energy of the specimen is also reduced, which has also been observed in many studies (Zdenek P. Bažant and Gettu 1992; Ping 1992; Rosa et al. 2012; Ruiz et al. 2011).

4.7 Validation of Numerical Model

Experimental results from published literature are used to validate the developed constitutive model. Two different types of tests have been used in this validation exercise. In the first test, a notched specimen under uniaxial tension is simulated without considering the effect of creep to validate the damage portion of the constitutive model. The second tests consist of three-point bending specimens subjected to various loading rates. Coupling of damage and creep is considered in the second validation tests.

4.7.1 Fracture under Uniaxial tension (No Creep)

Model: In this section, deformation-controlled tests reported in (Hordijk and Reinhardt 1990) are simulated. The specimen size is 150 mm x 60 mm x 50 mm with two saw cuts each of depth 5 mm in the middle. Figure 4-9(a) shows the full specimen while Figure 4-9(b) shows the single quadrant of the specimen modeled in the simulations by taking advantage of symmetry planes. The width of the notch is 5 mm. The specimen ends were glued to steel plates. The bottom platen was fixed while the upper platen was connected to the actuator of a servo-hydraulic loading machine. The model with boundary conditions and loading are shown in Figures 4-9(c) and (d). The material properties used for this simulation are given in Table 4-4. Figure 4-10 shows the details of the finite element meshes with varying levels of refinement used in the convergence study.

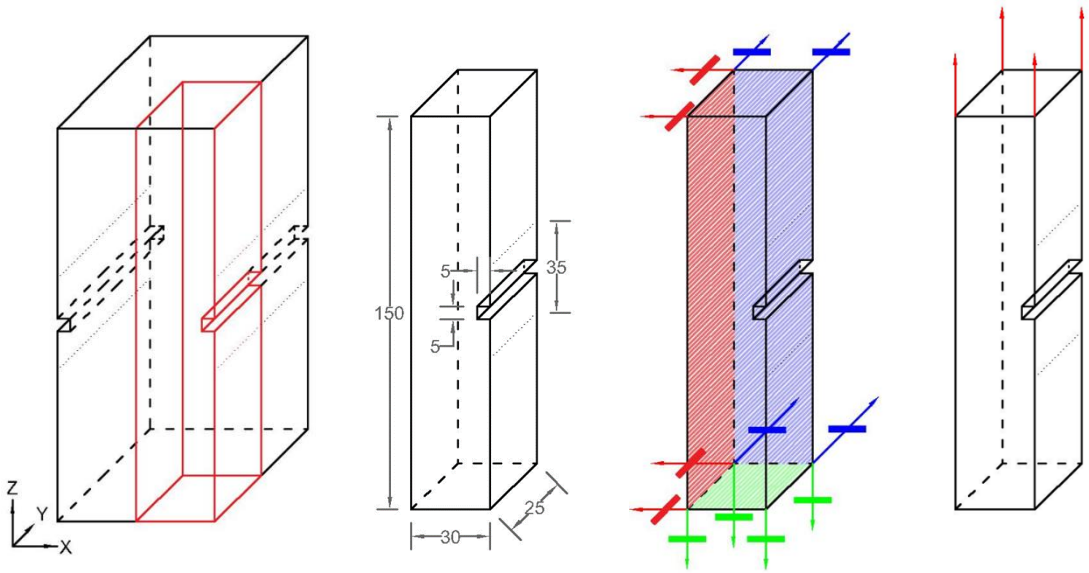

(a) (b) (c) (d)

Figure 4-9. FE Model Showing: (a) the Full Specimen and the Quarter Model (Inside) Used in the FE Simulation, (b) Geometric Details of the Specimen (Dimensions in mm), (c) FE Nodal Fixity Conditions, and (d) Applied Loading.

Results: In the experiments, the force was measured using a load cell. The stress in the notched section is obtained by dividing the force by the cross-sectional area at the notch.

The displacements were measured using four 35 mm extensometers positioned along the notched face of the specimen. In the simulation, the stress in the notched section is obtained by summing the reactions of all the nodes at the bottom and dividing by the cross-section area at the notch. The displacements were computed by subtracting the displacements of nodes at 17.5 mm below the center from the displacements of nodes at 17.5 mm above the center (Figure 4-9(b)). The results of simulations and experiments are shown in Figure 4-11.

Mesh 1	Mesh 2	Mesh 3	Mesh 4	Mesh 5
No. of elements 4025	No. of elements 21359	No. of elements 37393	No. of elements 417152	No. of elements 658142
No. of nodes 954	No. of nodes 4387	No. of nodes 7435	No. of nodes 76665	No. of nodes 72380
(a)	(b)	(c)	(d)	(e)

Figure 4-10. FE Meshes Used in the Simulation of the Validation Specimen Under Uniaxial Tension. (A)-(D) Mesh 1 Through 4 Have Tetrahedral Elements, (E) Mesh 5 Has Hexahedral Elements.

Table 4-4. Material Properties for Uniaxial Notched Concrete Specimens

Elastic modulus	18660 N/mm^2
Poisson's ratio	0.2
Tensile Strength	2.75 MPa
Fracture Energy	0.077 N-mm/mm^2
Residual Stress	0 MPa

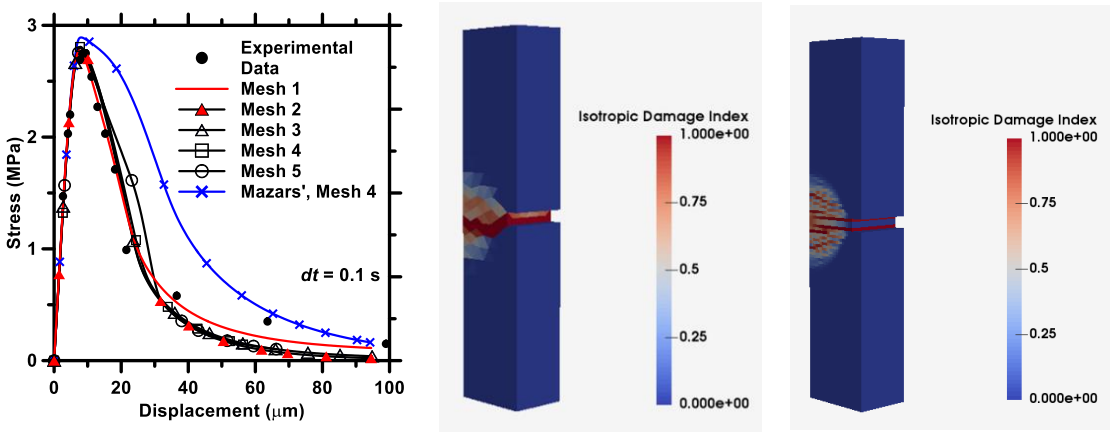

(a) (b) (c)

Figure 4-11. (a) Results of FE Simulations of Specimen Subjected to Uniaxial Tension, and Damage State at the End of the Simulation for (b) Mesh 1 and (c) Mesh 5. Experimental Data from (Hordijk and Reinhardt 1990)

Discussion: Figure 4-11(a) shows that the simulated load-displacement responses are only mildly affected by changes in element size within the considered range, since energy dissipation with varying mesh sizes and element types are the same. The convergence analysis was also carried out for hexahedral meshes and the results of only the finest mesh are shown to avoid repetition. The response in the post-peak region is overestimated (i.e., higher load for the same displacement) when Mazars' equivalent strain is used (Mesh 4 is used to implement Mazars' equivalent strain model, as an example). As explained earlier, this necessitated the use of von Mises equivalent strain even though Mazars' formulation is intuitively simpler to implement. Figure 4-11(b) shows the typical damage state at the end of the simulation for Mesh 1 while Figure 4-11(c) shows the damage state for Mesh 5.

4.7.2 Fracture Under Three-Point Bending (Combined Creep and Damage)

The three-point bending tests carried out at varying loading rates on concrete specimens reported in (Zdenek P. Bažant and Gettu 1992) and (Rosa et al. 2012) were used to validate the rate dependence of the creep-damage constitutive model. The experimental details are described followed by the model and material properties.

Experiments: In the first experiment simulated, the depth of the beam is 152 mm while in the second case, the depth is 100 mm. These tests will be referred to as D152 and D100 in the following discussion. The specimen details are listed along with Figure 4-12(a). The D152 tests are carried out at three different rates described by the authors in (Zdenek P. Bažant and Gettu 1992) as *usual*, *slow* and *very slow* based on the time it took to reach the peak load, which was around 500 s, 13,650 s and 253,000 s respectively. In the D100 tests, displacement loading rates of 5.5×10^{-4} mm/s and 1.74×10^{-5} mm/s was applied which will be referred to as *usual* and *slow*. Load-crack mouth opening displacement (CMOD) responses were obtained experimentally and are compared with simulated values.

FE model: The FE meshes used in the simulations are shown in Figure 4-12(b) and 4-12(c) for the D152 and D100 specimens respectively. A plane stress analysis is carried out in this case as the specimen geometry and the loading meet the required plane stress conditions. The load is applied at the center of the top steel block.

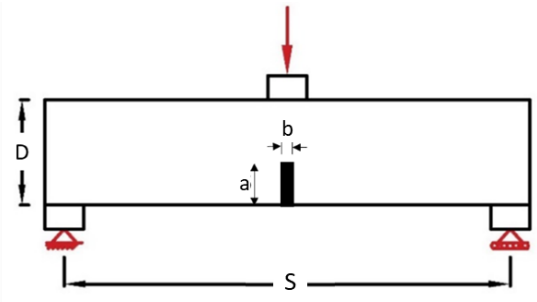

(a)

Dimensions	D152	D100
Beam depth, D	152 mm	100 mm
Beam width, B	38 mm	100 mm
Beam span, S	380 mm	450 mm
Notch width, b	1.8 mm	5 mm
Notch depth, a	25 mm	50 mm

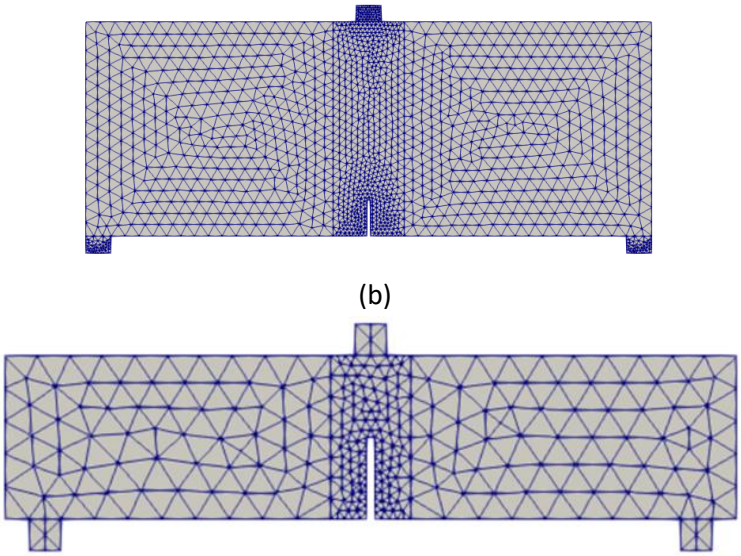

(b)

(c)

Figure 4-12. FE Model Showing: (a) Dimensions for the Simulated Specimens Used for Combined Creep-Damage Tests, and (b) and (c): Meshed D152 and D100 Beams Respectively.

Material Properties for D152: Material properties used in the simulation of the D152 tests are shown in Table 4-5. The elastic modulus, E_0 is taken as 56000 N/mm^2 which is the initial slope of stress-strain curve (Zdenek P. Bažant and Gettu 1992). The total fracture energy, G_F is taken as approximately 2.5 times the initial fracture energy G_f (area under the initial tangent of the stress-displacement plot) obtained from Bažant's size effect law (Z P Bažant 1999). For the *usual* loading rate case, the total fracture energy was obtained as 0.06 N-mm/mm^2. For *slow* and *very slow* loading rates, this value was taken as 0.07 N-mm/mm^2. A slightly higher fracture energy is taken for the specimen tested at *slow* and *very slow* rate of loading as these were cured for a longer duration than the specimens tested at the *usual* loading rate. The tensile strength was obtained as a function of compressive strength using the following relationship (Raphael 1984):

$$f_t = 0.437 \times {f_c}^{2/3} \text{ in MPa} \qquad (4.22)$$

To model the viscoelastic behavior, a generalized Maxwell model with ten Maxwell chains and a standalone spring were used, and the Maxwell material properties were determined based on Eq. (32) (Zdenek P. Bažant and Gettu 1992) using the rate type creep formulation (Zdeněk P. Bažant and Wu 1974).

Material Properties for D100: The elastic modulus is taken as $1.5E_{28}$ per (Zdeněk P. Bažant, 1988) where E_{28} is the secant modulus obtained at 28 days and is equal to 33.9 GPa(Rosa et al. 2012). The total fracture energy, G_F was measured as per RILEM recommendations (RILEM FMC-50 1985) and the modifications proposed in (Guinea, Planas, and Elices 1992; Planas, Elices, and Guinea 1992), and is provided as 0.128 N-mm/mm^2. The split tensile strength value provided in the experiments was used as the tensile strength. The Maxwell material properties were again calibrated using the relaxation function obtained from the BP model (Eq. (32)).

Table 4-5. Material Properties Used in the Simulation of Three-Point Bend Specimens

Material property	**D152**	**Notes**	**D100**	**Notes**
Elastic modulus, E_0	56000 N/mm^2	(A)	51000 N/mm^2	(F)
Poisson's ratio, ν	0.2	(B)	0.2	(B)
Tensile Strength	4.85 MPa	(C)	5.2 MPa	(A)
Fracture Energy	0.06 (*usual*) and 0.07 (*slow* and *very slow*) N-mm/mm^2	(D)	0.128	(A)
Modulus and corresponding characteristic time of each unit in the Maxwell model	7070 MPa, 1E-4 s 560 MPa, 1E-2 s 6930 MPa, 1 s 5910 MPa, 1E+2 s 8690 MPa, 1E+4 s 7550 MPa, 1E+6 s 6810 MPa, 1E+8 s 4650 MPa, 1E+10 s	(E)	6400 MPa, 1E-4 s 500 MPa, 1E-2 s 6300 MPa, 1 s 5400 MPa, 1E+2 s 7900 MPa, 1E+4 s 6900 MPa, 1E+6 s 6200 MPa, 1E+8 s 4200 MPa, 1E+10 s	(E)

	3250 MPa, 1E+12 s 4580 MPa, ∞		3000 MPa, 1E+12 s 4200 MPa, ∞	
Creep Damage Parameter	0.1, 0.9	(B)	0.1, 0.9	(B)

(A) Experimental Data in (Zdenek P. Bažant and Gettu 1992; Rosa et al. 2012), (B) Commonly adopted/assumed value for concrete, (C) Obtained using Eq. (33), (D) Calibrated using experimental data, (E) Obtained using rate type creep law (Zdeněk P. Bažant and Wu 1974), (F) Based on secant elastic modulus at 28 days as per (Zdeněk P. Bažant, 1988).

Results: The load-CMOD responses at various loading rates with two different values of the creep damage parameter ($\beta' = 0.1, 0.9$) are shown in Figure 4-13.

Discussion: As observed from Figure 4-13, the simulation results match quite well with the experimental results for all the cases considered, when $\beta' = 0.1$. The peak load is accurately predicted by the model. The post peak response also matches the experimental data reasonably well. It is not known if the reported experimental response is the average response of one or several replicated specimens for D152. For D100, the experimental curves shown in Figures 4-13(d) and (e) correspond to the upper and lower bound of four replicated specimens. For all of these cases, it is observed that a value of 0.1 for β' (indicative of weak coupling between creep and damage) predicts the experimental response quite well, as opposed to a strong coupling factor (0.9 for β'). Thus, a value of creep-damage parameter of 0.1 is recommended based on the proposed modeling framework and the validation results. This value is similar to the value obtained for a compression creep test in an earlier work (C Mazzotti and Savoia 2001).

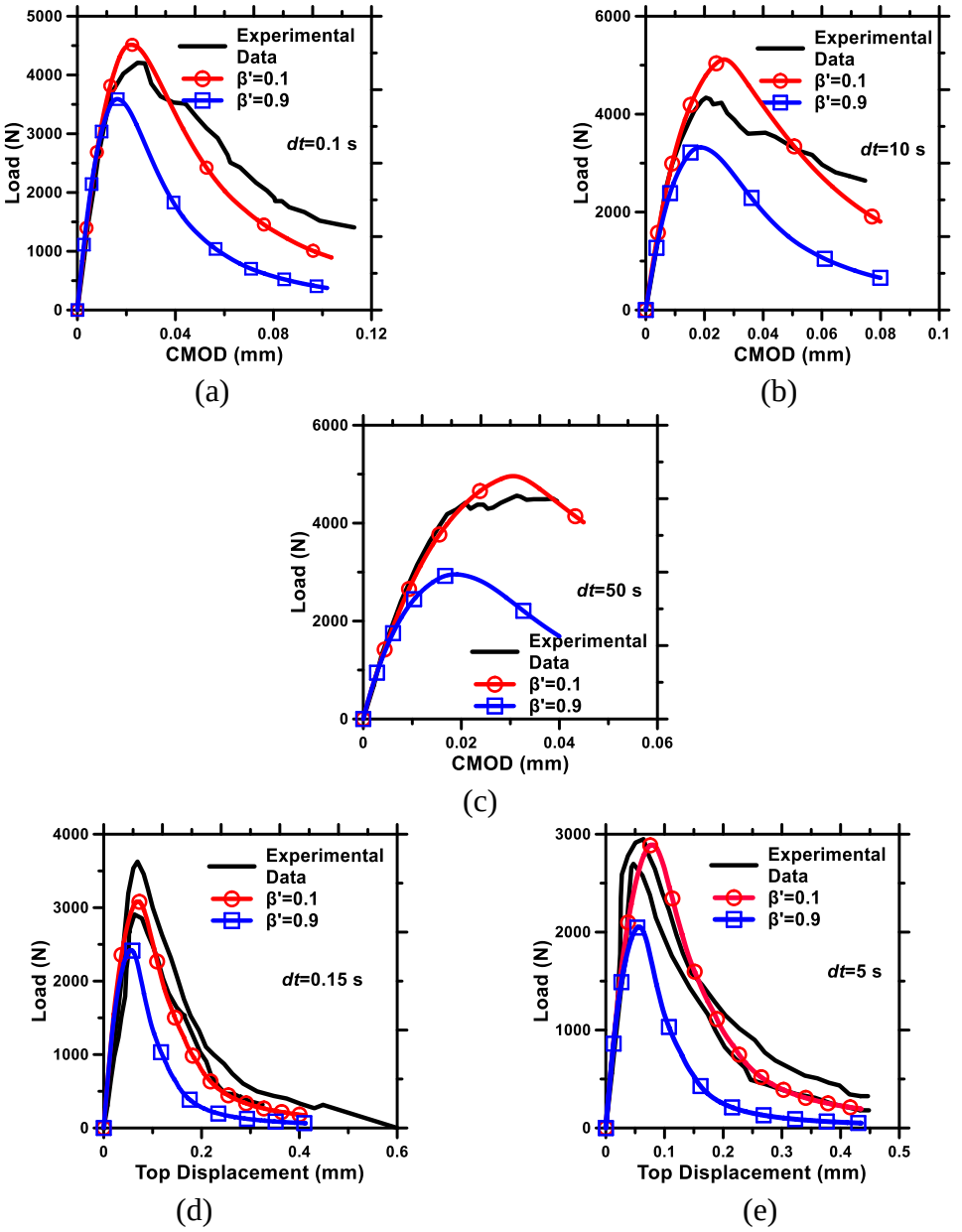

Figure 4-13. Results of FE Simulation and Comparison With Experimental Results of Three-Point Bend Specimens at Various Loading Rates: (a) *Usual* (b) *Slow* and (c) *Very Slow* Loading Rates for D152 Specimens, and (d) *Usual* and (E) *Slow* Loading Rates for D100 Specimens.

4.8 Summary and Conclusions

This work describes the numerical implementation of an isotropic damage model to simulate failure in concrete specimens including the coupled creep-damage effect in the

MOOSE framework, which is an open source C++ based finite element framework. The developed model considers linear viscoelasticity using generalized Maxwell and Kelvin-Voigt rheological models. A creep damage parameter is used to link non-linear creep and damage. To avoid convergence issues with vanishing energy dissipation, the characteristic length of each element is used such that the energy release rate for each element remains constant. The proposed formulation captures the interaction between creep and damage, and with a modification in the elastic damage model, can capture the behavior of concrete under slowly applied loading rates. The reduction of tensile strength and fracture energy under slower loading due to creep effects is captured by the model. Thus, the rate dependence of crack growth is implicitly reproduced by the proposed formulation.

The constitutive model was verified with various uniaxial and shear test cases. The model was then validated against the test results of notched specimens under uniaxial loading for the damage-only case. The model adequately captures the peak and post-peak behavior of the specimen, thus validating the damage model. The creep-damage model was also used to simulate the results of experimental tests whose duration varied from minutes to a few days. All the input material properties, such as the elastic modulus, tensile strength and fracture energy were taken as the ones corresponding to typical rates of quasi-static loading. These properties were then used to simulate the behavior at rates significantly lower than the typical quasi-static loading rates. The results showed that a strong coupling between creep and damage overestimates the damage and underpredicts the constitutive response. Parametric simulations using various values of the creep-damage parameter showed that only about 10% of the creep strain contributes towards damage for the cases considered in this study. This is similar to values reported for short term compression creep

tests (C Mazzotti and Savoia 2001) and hence can be chosen with a considerable degree of confidence in predictive simulations. However, the proposed formulation has not been evaluated for even slower loading rates due to the lack of experimental data; it would be important to ascertain if the creep effects on the softening behavior are properly accounted for in such extremely slow loading rates as such effects can be encountered in practice.

CHAPTER 5

VALIDATION OF NUMERICAL MODEL - RESTRAINED RING TEST

In this validation exercise, experimental results from published literature are used to validate the developed constitutive model by considering the moisture diffusion and its effect on the shrinkage properties. These tests are different than the three-point loading being considered in the previous section in which only mechanical loading was applied.

5.1 Restrained Ring Shrinkage Experiments

A series of restrained ring shrinkage tests on Ordinary Portland Cement (OPC) pastes with and without 10% or 20% by volume of inclusions (either soft or stiff) and varying humidity levels were carried out in (Wei, Falzone, Das, et al. 2017b). These tests are used in this work to develop and validate the numerical model and to ascertain the effect of inclusions and relative humidity on the cracking propensity of cementitious materials. Along with restrained ring shrinkage tests (in general, conforming to ASTM C 1581), this modeling effort requires results from free shrinkage (ASTM C157), elastic modulus (ASTM C469) and splitting tensile (ASTM C496) tests, which are also reported in (Wei, Falzone, Das, et al. 2017b). Phase change materials (PCMs) (Aguayo et al. 2016; Fernandes et al. 2014; Thiele et al. 2016; Wei, Falzone, Wang, et al. 2017) were used as soft inclusions and quartz sand as stiff inclusions, in an attempt to understand the cracking sensitivity of cementitious mixtures in the presence of compliant or stiff particles. The microencapsulated PCM particles had a median size of 20 μm while the quartz particles were 10 times larger. The volume fractions of the PCM used were 10% or 20%, while that of quartz was 10%. All the paste mixtures were proportioned at a fixed water-to-cement ratio (w/c; by mass) of 0.45. Material properties and mixture proportions of the pastes can be found in (Wei,

Falzone, Das, et al. 2017b). The dual ring geometry used for the tests is shown in Figure 5-1. The pastes were cast between two Invar rings (coefficient of thermal expansion of 2.5 με/^{o}C) and maintained in sealed bags in a programmable environmental chamber at 25±0.1^{o}C and 87±0.1% relative humidity (RH) to limit moisture loss for the first 7 days. The top surface was covered with PVC sheets to minimize the potential for drying. After 7 days of partially sealed curing, the rings were kept on an elevated wire mesh platform with their top and bottom surfaces exposed and dried at 50 ± 0.1% RH until cracking occurred. Four strain gauges each on the inner outer rings installed at 90^{o} from each other at the mid height of the ring, were used to detect cracking.

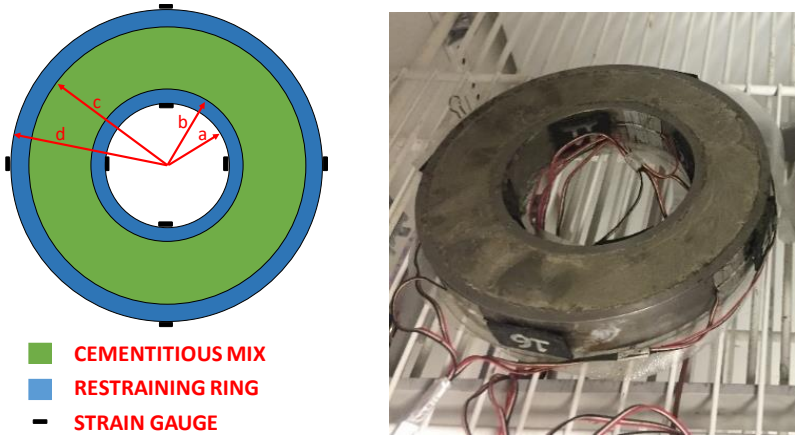

Radius (mm)	a	b	c	d
Ring test (dual ring) on cement pastes (with and without inclusions)	44.5	50.8	76.2	82.6

Figure 5-1. Illustration of the Restrained Ring Test and the Geometry Used in Experiments (Wei, Falzone, Das, et al. 2017b).

5.2 Material Models

The isotropic damage approach is used to model the fracture of cementitious materials in the ring test. To account for the fact that material strengths of individual finite elements are

statistically distributed, a framework to account for aleatory uncertainty and associated size effects is introduced in the simulations as described in (Strack, Leavy, and Brannon 2015). The viscoelastic response of aging cementitious materials is modeled using a rate-type creep law based on the generalized Maxwell model while damage is characterized by isotropic damage code as developed in Chapter 4.

5.2.1 Aleatory Uncertainty and Size Effects

Simulation of failure in heterogeneous cement-based materials needs consideration of statistical variability and associated microstructural size effects. Aleatory uncertainty indicates the uncertainty due to random variations – from a strength perspective, it indicates the natural variation in the spatial distribution of the microstructural features (flaws or microcracks, for example), that results in localized regions being stronger or weaker than the surrounding material (Strack, Leavy, and Brannon 2015). For cementitious materials which exhibit quasi-brittle behavior with a finite fracture process zone compared to the structural size, the cumulative probabilistic distribution of strength is highly complex (Le, Bažant, and Bažant 2011; Bernard, Kamali-Bernard, and Prince 2008; Li and Maalej 1996). In such cases, it is not physically realistic to predict the failure stress using a deterministic strength-based approach, where a uniform strength is assumed at every point in the material (or for all the finite elements, thereby violating Weibull scale effects where large elements are weaker, on average, than small elements). Thus, numerical perturbations in the spatial strength distribution are required for realistic modeling of failure. The variability in strength provides perturbations in the stress field necessary to simulate the local defects and crack localization inherent in the material. Without these perturbations, in structures with relatively uniform tensile stress fields over large areas such as the axisymmetric ring

specimens considered here, many finite elements would reach the failure stress simultaneously, causing convergence issues and undesirable responses in the FE modeling. Including a realistic numerical perturbation in the computational model gives rise to localized strains and stresses and is particularly useful for problems involving bifurcation in a localized state (Zdeněk P. Bažant and Xi 1991). Apart from the numerical perturbations, the strength of the brittle materials is highly dependent on the size of the structure. The probability of occurrence of a critical crack is higher in a larger structure than in a smaller structure (Z P Bažant 1999). Combining the size effect with the Weibull distribution of strength enhances numerical convergence by localizing the failure and makes the cracking model more robust.

In this work, we employ a methodology proposed in (Strack, Leavy, and Brannon 2015), to introduce spatial randomness in the FE model of the ring test. Microscale heterogeneities are accounted for by randomizing the material strengths in each finite element, while preserving the median strength of a finite volume of material. Each finite element is considered as an independent specimen, the strength of which needs to be statistically assigned based on laboratory data. Thus, the failure stress σ_e of a finite element of volume V_e is considered to be Weibull distributed with a median stress of $\bar{\sigma}$ determined for a collection of finite elements of total volume $\bar{V}$ (such that $V_e \neq \bar{V}$). In general, $\bar{V}$ can be considered to be the volume of the experimental sample. $\bar{\sigma}$ is taken as the tensile strength (e.g., from the splitting tensile strength experiments). The failure stress is predicted using Weibull theory as (Strack, Leavy, and Brannon 2015):

$$\sigma_e = \bar{\sigma} \left(\frac{\bar{V} \ln R}{V_e \ln\left(\frac{1}{2}\right)} \right)^{1/m} \tag{5.1}$$

where R is a uniformly distributed random number such that $0 \leq R < 1$, and m is the Weibull modulus. The Weibull modulus controls the shape of the distribution. A higher value of m indicates a lower variability in the distribution. In this work, 10 or more random realizations of the tensile strength distribution were generated, each using a unique value of the seed in the random generator, which results in a different structural strength for each run. The spread of the predictions is shown in the section on simulation results.

5.2.2 Generalized Maxwell Model for Viscoelasticity

The constitutive relations to describe the time-dependent deformation of early-age cementitious materials can be approximated using generalized Maxwell or Kelvin-Voigt models (Zdeněk P. Bažant and Wu 1974; Zdenek P. Bažant and Wu 1973) constituted of time-variable viscosities and spring moduli. Both the Maxwell model and Kelvin-Voigt model can be applied to analyze the aging viscoelastic behavior of hydrating cement paste. In this study, we select the Maxwell model since the material parameters are easier to identify in the context of stress relaxation (Zdeněk P. Bažant and Wu 1974). The constitutive relationship between stress $\sigma(t)$ and strain $\varepsilon(t)$ for a linear viscoelastic material under uniaxial loading is given as (Zdeněk P. Bažant and Wu 1974):

$$\sigma(t) = \int_0^t E_R(t, t')[d\varepsilon(t') - d\varepsilon^0(t')] \tag{5.2}$$

where, the integrals are the generalized form of Reimann integral, called as Stieltjes integrals. $\varepsilon^0(t)$ is the stress-independent inelastic strain, and the relaxation

function, $E_R(t,t')$ indicates the stress in the material at time t due to a unit constant strain acting since time t' $(t > t')$. The relaxation curves can be expanded into a Dirichlet series and approximated using the generalized Maxwell model which contains a standalone spring, and a combination of springs and dashpots in series (Maxwell units), both arranged in parallel (Figure 2-1). The relaxation function can then be expressed as (Zdeněk P. Bažant and Wu 1974):

$$E_R(t,t') = \sum_{\mu=1}^{p} E_\mu(t') e^{-\frac{t-t'}{\tau_\mu}} + E_\infty(t') \tag{5.3}$$

where p is the total number of Maxwell units of the generalized model, and $E_\mu(t')$ and $E_\infty(t')$ are the moduli associated with springs in the individual Maxwell unit and the standalone spring respectively. τ_μ is the relaxation time, which is represented as the ratio of the viscosity of the dashpot (η_μ) to the modulus of the spring (E_μ) as shown in Equation 5.4. The implementation of generalized Maxwell model in MOOSE is described in greater detail in Chapter 3.

$$\tau_\mu = \frac{\eta_\mu}{E_\mu} \tag{5.4}$$

5.3 Finite Element Model and Inputs

A two and three-dimensional FE model is used to characterize and compute the restrained volume change response of the cementitious mixtures. Using symmetry boundary conditions, one quarter model for 2D and one-eighth of the model for 3D (quarter model in plan, with half the actual thickness) as shown in Figure 5-2 are simulated, in order to lower computational time. Since the symmetric boundary condition alone suppresses the rigid body modes, external constraints are not needed. It should be noted, however, that

this is only an approximation of real behavior as this assumes that similar cracks are formed in the non-modeled sections also. The outer ring has not been modeled (even though it was a dual ring experiment as explained earlier), as the paste shrinks and loses contact with the outer ring and the volume change is restrained by the inner ring alone. Although the cement paste initially expands and then starts to shrink, the initial expansion, usually caused by the heat generated by early age cement hydration (Bentz 2008), is ignored in the model. The ring and cement paste are modeled as separate parts with a frictionless contact acting between the two parts to mimic the actual experiment where a form release agent was applied on the surface of the rings in contact with the cement paste. In order to generate and use an efficient but acceptably accurate FE model, a convergence analysis was carried by varying the number of nodes and elements. The model containing the finite element mesh shown in Figure 5-2, with 2325 four-noded quadrilateral and 30225 eight-noded hexahedral elements for 2D and 3D simulations respectively, yielded the best results. The mesh orientation has been chosen so that the crack runs in an outward radial direction, after initiation, to avoid mesh bias. All finite element simulations were carried out using Arizona State University computing cluster (Agave) - CentOS 7.4 with each node configured with Intel Broadwell CPU containing 28 cores and 128 GB RAM. Only one node with 28 cores was used that took approximately 10 minutes and 50 minutes of wall clock time for each 2D and 3D simulations respectively.

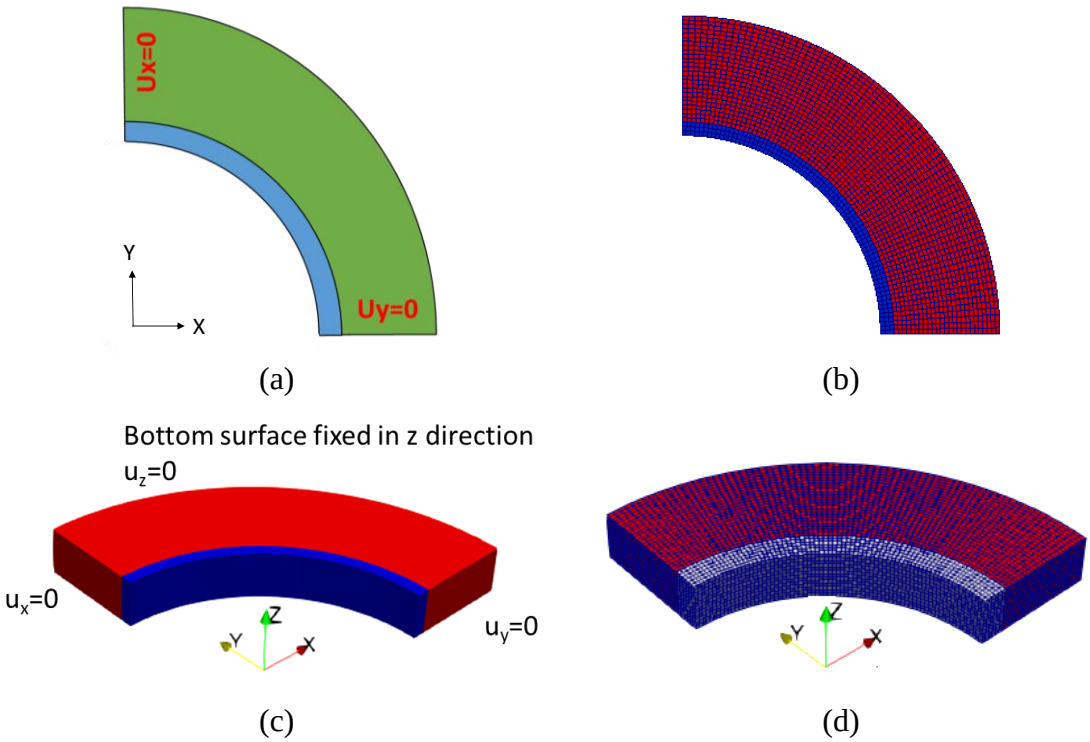

Figure 5-2. (a) Quarter Symmetry 2D FE Model With the Boundary Conditions Used in the Analysis, (b) a Typical 2D FE Mesh Used in the Analysis, and (c) One-Eighth Symmetry 2D FE Model (Quarter Model in the Plan, With Half the Thickness) With the Boundary Conditions Used in the Analysis, (d) a Typical 3D FE Mesh Used in the Analysis.

5.3.1 Input Parameters

The input parameters for the material models described in Section 3.1 are the Young's modulus, $E(t)$, the tensile strength σ_{tu}, the relaxation function, $E_R(t,t')$, and the post-peak stress-strain curve. As previously stated, the time-dependent evolution of elastic modulus and tensile strength were experimentally determined. The methodology to obtain the viscoelastic parameters (spring modulus and dashpot viscosities/relaxation times) is explained in the following section. Aleatory uncertainty described earlier was used to distribute the tensile strengths of the finite elements in accordance with Equation 5.1. The distribution of tensile strengths in the simulated ring for the paste with 20% PCM

inclusions at 7 days are shown in Figure 5-3 to demonstrate the random distribution of strengths, which accounts for uncertainties in failure initiation and propagation. As mentioned earlier, 10 or more such random realizations were used in each of the simulations. As the tensile strengths were found not to be influenced significantly by the presence of PCM particles (in the range of volume fractions considered in the study), the reasons for which have been adequately described in (Wei, Falzone, Das, et al. 2017b; Aguayo et al. 2016), and owing to their small size, they have not been meshed explicitly. The Weibull modulus (m) was taken as 24, which is commonly adopted for cement-based materials (Z P Bažant 1999). The elastic modulus and Poisson's ratio of the Invar ring were taken as 141 GPa and 0.28 respectively. The different parameters that are used in the framework and the corresponding values used are listed in Table 5-1.

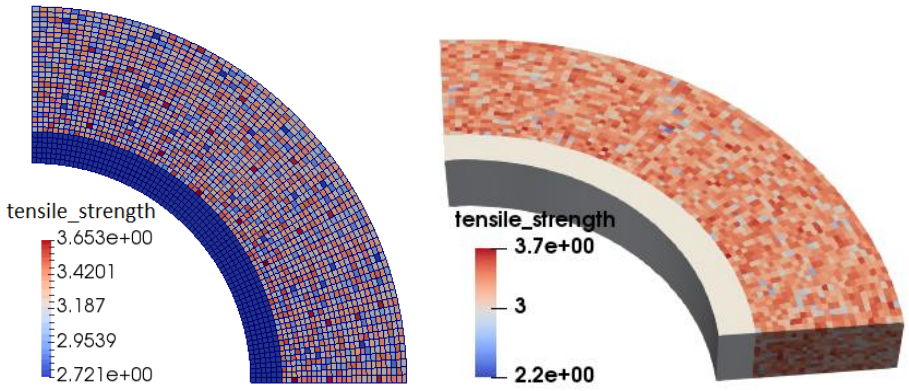

Figure 5-3. Representative Realizations of Aleatory Uncertainty-Based Distribution of Tensile Strengths in the Finite Element Model for Cement Paste for 2D and 3D Specimens.

Table 5-1. Constitutive Parameters Used in the Simulation of Ring Test

Material Property	Value	Ref
Elastic Modulus of Invar,	141 GPa	(Wei, Falzone, Das, et al. 2017b)
Poisson's ratio of invar, $\boldsymbol{\nu_I}$	0.28	
Poisson's ratio of paste, $\boldsymbol{\nu_p}$	0.20	
Relaxation function	See Figure 5-5	

$E_R(t,t')$		
Relaxation time of the first Maxwell unit τ_1	0.001 day	(Zi and Bažant 2002)
Relaxation time spacing a	4	
Median tensile strength, $\bar{\sigma}$	2.5 MPa	(Wei, Falzone, Das, et al. 2017b)
Volume, $\bar{V}$	257407 mm^3	
Weibull Modulus	24	(Z P Bažant 1999)
Weights, w_1 and w_2	0.1	(Zdeněk P. Bažant and Wu 1974)
Diffusion Coefficient, $\mathbf{D_1}$	60 mm^2/day	(Comite Euro-International Du Beton 1993)
Surface factor, $\mathbf{f}_{boundary}$	0.3 mm/day	(Oliveira, Azenha, and Lourenço 2015)
Diffusion equation parameters, α, h_c and n	0.05, 0.8 and 15	(Z. P. Bažant and Najjar 1971)
Creep equation parameters, k_1 and k_2	2.1, 0.5	(Tamtsia, Beaudoin, and Marchand 2004)
Ultimate Shrinkage coefficient, $\varepsilon_{SH-\infty}$	2000 μm/m 4000 μm/m	(Hansen 1987)

5.3.2 Algorithm for Determination of Viscoelastic Parameters

There exist several ways to obtain the relaxation function for early age cementitious materials if it is not available from experiments. The ring test itself could be used to obtain the aging relaxation function as described in (Grasley and D'Ambrosia 2011). It could also be obtained from creep compliance functions which are usually available in form of empirical relations for concrete. For early age cement paste, the creep compliance, J, can be expressed as a function of the degree of hydration α_d, the degree of hydration at loading α_{d0}, and the relative humidity in the paste as (Tamtsia, Beaudoin, and Marchand 2004):

$$J(t,t') = J_0\big(1 + \emptyset(\alpha_d, \alpha_{d0}, RH)\big) \tag{5.5}$$

where, J_0 is the compliance at the age of loading (t_0), which is equal to the inverse of the elastic modulus. $\emptyset$ is the creep coefficient given as:

$$\emptyset = k_1 {f_{\alpha_d}}^{k_2} \tag{5.6}$$

where, k_1 and k_2 are the experimentally fitted coefficients and are taken as k_1=2.1, k_2 =0.5 (Tamtsia, Beaudoin, and Marchand 2004) for all ages of loading. Ideally, $k_1$and k_2 should vary for different ages but in the absence of data for later ages of loading, they are taken as constant for all ages of loading. f_{α_d} is the fractional increase in degree of hydration and is given as:

$$f_{\alpha_d} = \frac{\alpha_d - \alpha_{d0}}{\alpha_{d0}} \tag{5.7}$$

The relaxation function is obtained from the creep compliance function by using the approximate relationship (Zdeněk P. Bažant, 1988):

$$E_R(t,t') = \frac{0.992}{J(t,t')} - \frac{0.115}{J_0}\left[\frac{J\left(t-\frac{t-t'}{2},t'\right)}{J\left(t,t'+\frac{t-t'}{2}\right)} - 1\right] \tag{5.8}$$

The expression for the relaxation function as a function of the Maxwell model parameters given in Equation 5.3 can be used to determine these parameters through a least square fit. However, $E_\mu(t')$ are unstable functions of $E_R(t,t')$ unless the relaxation times, τ_μ's, are selected beforehand and certain smoothing conditions implemented (shown later in Equation 5.10) (Zdeněk P. Bažant and Wu 1974). The relaxation times are usually taken as being equally spaced in logarithmic time scale:

$$\tau_\mu = a^{\mu-1}\tau_1 \ (\mu = 1,2,\dots.,m) \tag{5.9}$$

where: (i) τ_1, the relaxation time associated with the first Maxwell unit, was taken as the time during which the relaxation spectra begin to descend in the log time scale, and (ii) the spacing of the relaxation times in the time scale is given as a. In this work, the value of τ_1 is taken as 0.001 day (Zi and Bažant 2002), and the value of a is taken as 4 (instead of 10 as reported in (Zdeněk P. Bažant and Wu 1974)), as we are not concerned with long-term creep behavior. Numerical experiments were conducted using 7 Maxwell units to validate these choices and the assumed values provided a better distribution of τ_μ's over the time range of interest in this work (a few days). The spring moduli, $E_\mu(t')$, are obtained by minimizing the function Φ with respect to E_μ and E_∞ as:

$$\Phi = \sum_\beta \left(E_R(t_\beta, t') - \tilde{E}_R(t_\beta, t')\right)^2 + w_1 \sum_{\mu=1}^{m-1}\left(E_{\mu+1} - E_\mu\right)^2 + w_2 \sum_{\mu=1}^{m-2}\left(E_{\mu+2} - 2E_{\mu+1} + E_\mu\right)^2 \tag{5.10}$$

where, $\tilde{E}_R(t, t')$ denotes the actual values for the relaxation function, β denotes a series of $(t - t')$ values, and w_1 and w_2 denotes the weights associated with the sum of the squares of the first and second difference of E_μ as functions of μ. These weights have been taken as 0.1 here, in line with other reported studies (Zdeněk P. Bažant and Wu 1974). A custom MATLAB code was developed to compute the relaxation spectrum from the degree of hydration data. The code also computes the Maxwell model parameters from the relaxation spectrum which forms the input to the aging material model in MOOSE.

5.3.3 Relaxation Spectra for Cement Pastes

It has been shown that the soft/stiff inclusions do not significantly influence the degree of hydration of the cement paste in the range of volume fractions considered (Fernandes et al.

2014). The experimental degree of hydration data (Fernandes et al. 2014) was fitted using a logarithmic equation as shown below.

$$\alpha_d = 0.12ln(t) + 0.42 \tag{5.11}$$

Here, t is in days. The degree of hydration is then used to compute the creep compliance using Equation 5.5. The calculated creep compliance and experimental results for OPC pastes of two different w/c (Tamtsia, Beaudoin, and Marchand 2004) loaded after 1 day are shown in Figure 5-4(a).

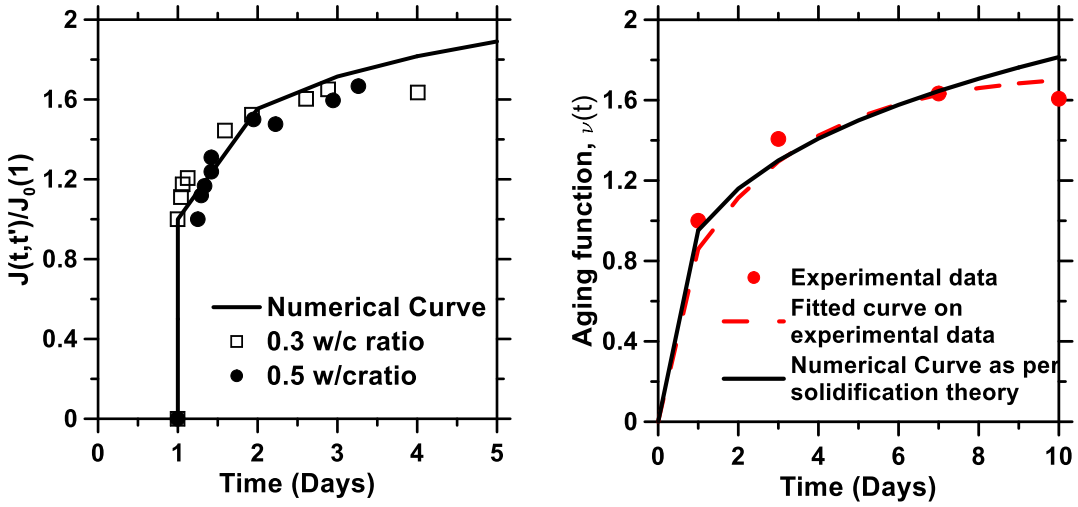

Figure 5-4. (a) Comparison of Numerically Obtained Compliance Function for OPC Paste With the Experimental Results. The Numerical Function is Obtained by Fitting the Maxwell Parameters while the Experimental Results are from (Tamtsia, Beaudoin, and Marchand 2004), and (b) Aging Function Obtained by Fitting Experimental Elastic Modulus Data and the Numerical Aging Function Given by Solidification Theory (Zdeněk P. Bažant and Prasannan 1989).

Once the creep compliance is known, it is converted to relaxation function using Equation 5.8. The relaxation spectra determined for the plain paste and the pastes with inclusions are shown in Figure 5-5. The relaxation function at later ages is computed by multiplying the viscoelastic modulus obtained at 1 day by the aging function. The relaxation function is

then used to compute the Maxwell model parameters by minimizing Equation 5.10. The aging function, $\nu(t)$, can be expressed as (Grasley and D'Ambrosia 2011):

$$\nu(t) = \kappa\left(1 - \exp\left(-\lambda(t + t_d)\right)\right) \tag{5.12}$$

where $t_d = 1$ day is the time when drying is initiated. κ and λ are fit parameters which can be obtained by substituting a normalized elastic modulus as shown in Equation 5.13, for the aging function in Equation 5.12.

$$\nu(t) = {E(t)}\Big/{E(t = 1)} \tag{5.13}$$

As per the solidification theory, the aging function is given as (Zdeněk P. Bažant and Prasannan 1989):

$$\nu(t) = \frac{1}{\left(\frac{1}{t}\right)^{m_a} + \alpha_a} \tag{5.14}$$

where, m_a and α_a are fitting parameters taken as 0.33 and 0.05 for cement pastes (Zdeněk P. Bažant and Prasannan 1989). Figure 5-4(b) shows that, for the time period of interest in a restrained ring test (< 10 days), the aging function determined from elastic modulus and that predicted by solidification theory are in agreement.

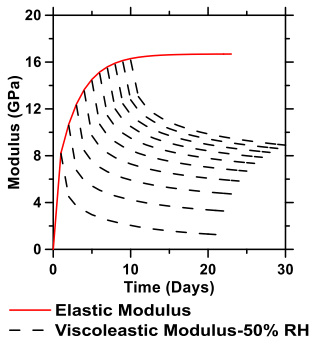

(a)

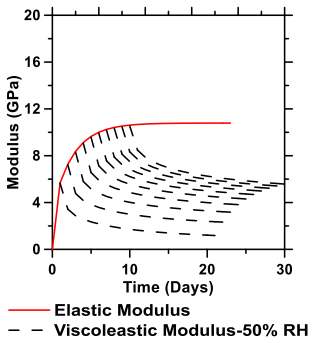

(b)

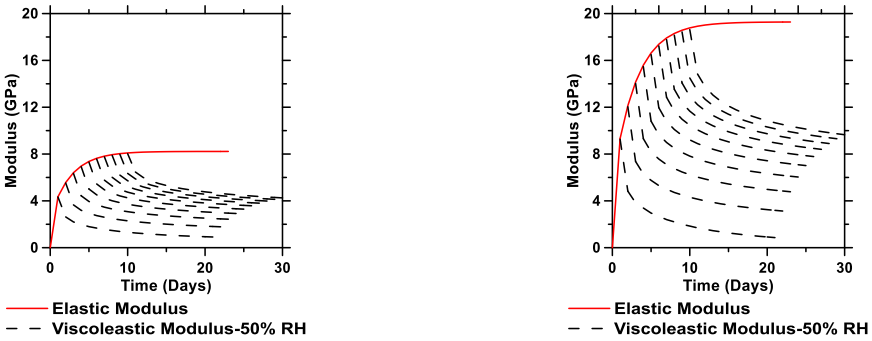

(c) (d)

Figure 5-5. (a) Time-Dependent Viscoelastic Moduli for: (a) Plain Paste (b) Paste With 10% PCM Inclusions (c) Paste With 20% PCM Inclusions, and (d) Paste With 10% Quartz Inclusions. The Dashed Lines Correspond to Different Ages t' = 1,2….10 Days

5.3.4 Imposed Loading to Simulate Shrinkage

The restrained ring test is usually accompanied by the free shrinkage test. The free shrinkage strain measured in the experiments at any given time is applied to the 2D finite element model as an imposed eigenstrain, assuming that the relative humidity is constant along the depth of the specimen. However, moisture gradients within the specimen give rise to differential shrinkage strain (Neithalath, Pease, and Attiogbe 2005; Z. P. Bažant and Najjar 1971). The movement of moisture inside the specimen is governed by diffusion and can be expressed as (Z. P. Bažant and Najjar 1971):

$$\frac{\partial w}{\partial t} = -\text{div}\mathbf{J_m} \tag{5.15}$$

where, w is the specific moisture content and $\mathbf{J_m}$ is the moisture flux through the specimen. This equation is highly nonlinear in the sense that $\mathbf{J_m}$ depends upon the gradient of the moisture content. In addition, it also depends on the specimen temperature which varies significantly during hydration (Zdeněk P. Bažant, 1988). At temperatures of interest, pore (relative) humidity is frequently used instead of specific moisture content as it eliminates

the effects of hydration (Neithalath, Pease, and Attiogbe 2005; Zdeněk P. Bažant, 1988). The corresponding equation is then stated as:

$$\frac{\partial H}{\partial t} = -\text{div}(\text{Dgrad H}) + \frac{\partial H_{auto}}{\partial t} \tag{5.16}$$

where, D is the diffusion coefficient, H is the pore relative humidity, and H_{auto} is the self-desiccation humidity. For specimens made with water-to-cement ratio greater than about 0.40, self-desiccation can be ignored. The diffusion coefficient is expressed as (Z. P. Bažant and Najjar 1971):

$$\text{D} = \text{D}_1\left(\alpha + \frac{1-\alpha}{1+\left(\frac{1-H}{1-h_c}\right)^n}\right) \tag{5.17}$$

where, α, h_c and n are constants taken as 0.05, 0.8 and 15 (Z. P. Bažant and Najjar 1971). D_1 is taken as 60 mm^2/day as per CEB-FIP (1990) (Comite Euro-International Du Beton 1993) for early age cement pastes (~7 x 10^{-10} m^2/s). Neumann's boundary condition (Oliveira, Azenha, and Lourenço 2015) is used, which is given as:

$$\text{D}\left(\frac{\partial H}{\partial x}\right) = f_{boundary}\left(H_{env} - H_{surf}\right) \tag{5.18}$$

where, $f_{boundary}$ is the surface factor, taken as 0.3 mm/day (Oliveira, Azenha, and Lourenço 2015). H_{env} is the environmental humidity and $H_{surf}$is the exposed surface humidity. The solution to the above problem is obtained by discretizing it using the finite difference technique and the resultant non-linear equations solved using Newton-Raphson method with a maximum tolerance of 0.0001. Further details can be found in (Oliveira, Azenha, and Lourenço 2015). The humidity profiles are shown in Figure 5-6(a), from which the imposed shrinkage strains are then calculated for 3D simulation as:

$$\Delta\varepsilon_{sh} = \varepsilon_{SH-\infty}\Delta H \tag{5.19}$$

where, $\varepsilon_{SH-\infty}$ is the ultimate shrinkage strain. The ultimate shrinkage strain depends upon the applied RH and thus different values are used for pastes drying under different RH. For pastes drying at 87.5% RH, this value was obtained as 2000 μm/m by fitting the free strain data reported in (Wei, Falzone, Das, et al. 2017b). For the paste drying at 50% RH this value was taken as 4000 μm/m (Hansen 1987). The shrinkage profiles are shown in Figure 5-6(b). The calculated shrinkage was imposed as a volumetric eigenstrain over the entire specimen for 3D simulations.

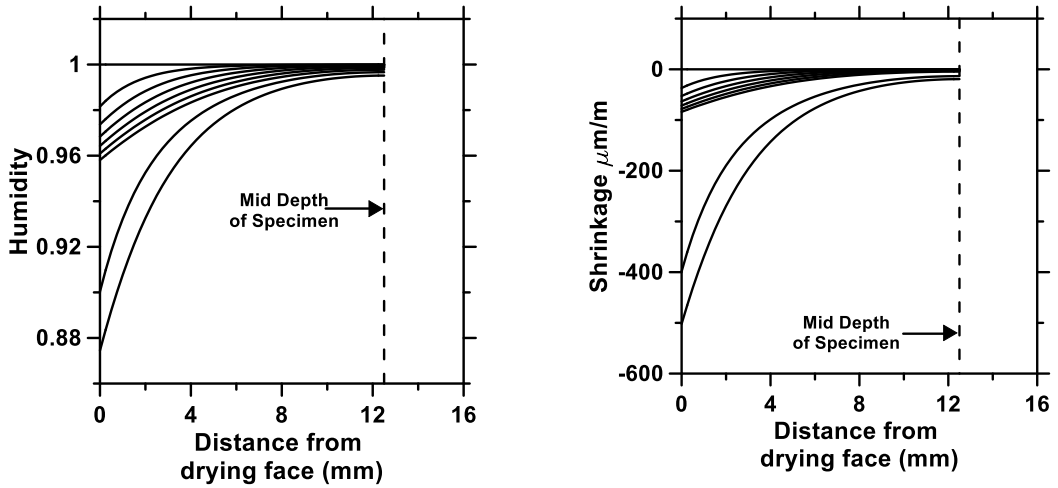

(a) (b)

Figure 5-6. Variation of: (a) Humidity, and (b) Shrinkage as a Function of the Specimen Depth at t=1,3,4,..9 Days for 3D Simulations.

5.4 Simulation of Restrained Shrinkage Cracking

In this section, the FE modeling scheme described above and as implemented in MOOSE, is used to simulate the restrained shrinkage response of OPC pastes containing soft or stiff inclusions with variable humidity. Figures 5-7 (a)-(c) shows the simulated residual stress development for the cement pastes containing PCM or quartz, and their comparison with the experimental data from (Wei, Falzone, Das, et al. 2017a). The simulated residual stress is the average of the hoop stresses in all the elements along the

inner surface of the ring, while the experimental data correspond to the residual stress calculated from the measured strain from the four gages. The calculated residual stresses by the simulations during the first 7 days of drying under partially sealed conditions match the trends reported in the experiments, i.e., higher stress for the system with stiffer inclusions, and the residual stress scaling with the elastic modulus. The imposed changes in viscoelastic parameters as a function of the change in drying rate (see Figure 5-6) enables accurate prediction of the sudden increase in stress development after 7 days as can be noticed in Figures 5-7 (a)-(c). The effect of aleatory uncertainty-based strength distribution on the stress response is also shown, with the post-crack band (shaded) showing the stress values simulated using multiple seed values of the random number. The simulated time of cracking is found to match quite well with the experimental results for all the modeled cement pastes. The simulation captures the fact that the addition of complaint PCM inclusions delays the cracking time as compared to stiffer quartz inclusions.

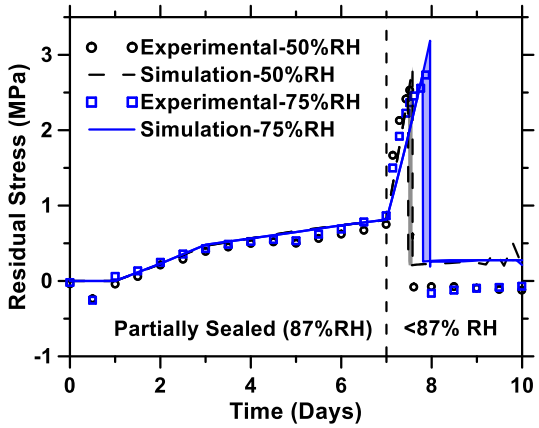

(a)

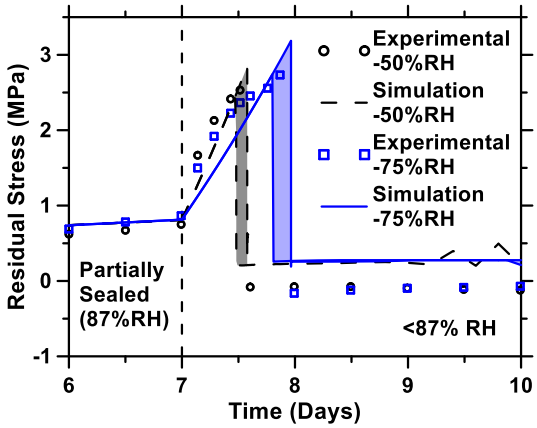

(b)

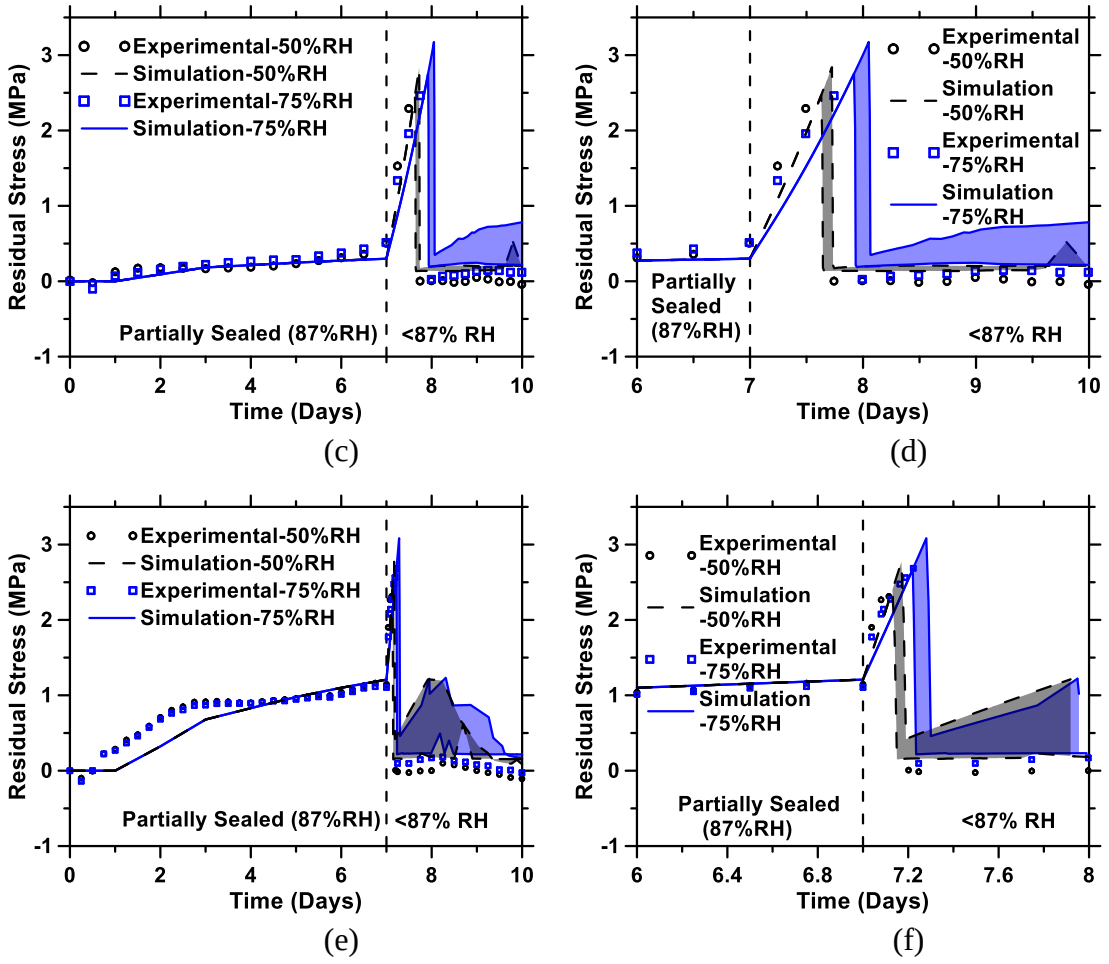

Figure 5-7. Simulated Residual Stress Development in the Cement Pastes and Their Comparison With Experimental Results from (Wei, Falzone, Das, et al. 2017b) With: (a) 10% PCM Inclusions, (c) 20% PCM Inclusions, and (e) 10% Quartz Inclusions, and Their Zoomed in Plots at the Instant of Cracking in (b), (d) and (f) Respectively. The Shaded Regions Show the Uncertainty in Time-to-Cracking and Residual Stresses Based on the Aleatory Uncertainty-Based Strength Distribution.

Figure 5-8 shows the simulated hoop strain development for the cement pastes with or without inclusions for 3D simulations respectively, and their comparison with the experimental data from (Wei, Falzone, Das, et al. 2017b). The simulated hoop strain is the average of the hoop strains in all the elements along the inner surface of the ring, while the experimental data correspond to the measured strain from the four gages. The time to cracking obtained from the experiments and simulations are provided in Table 5-2. The

simulated time of cracking is found to match quite well with the experimental results for all the modeled cement paste. The results for 2D simulations are better as compared to 3D simulations as the effect of change in humidity is more gradual and occur only at the top in 3D simulations. The 2D simulations ignore this and thus give better results. The time to cracking in the paste with PCM (soft) inclusions is slightly delayed as compared to the plain paste and the paste with quartz (stiff) inclusions. The delay in the cracking for paste with soft inclusions can be best understood by plotting the development of hoop stress at the top of the specimen as shown in Figure 5-9 (a). Due to the lower rate of stress growth (based on the viscoelastic properties), the time to reach the peak stress is delayed in the pastes with soft inclusions. The effect of aleatory uncertainty-based strength distribution on the stress response is also shown in Figure 5-9 (b), with the post-crack band (shaded) showing the influence on cracking stress when simulated using multiple seed values of the random number. The 3D simulations will be further examined in a little more detail.

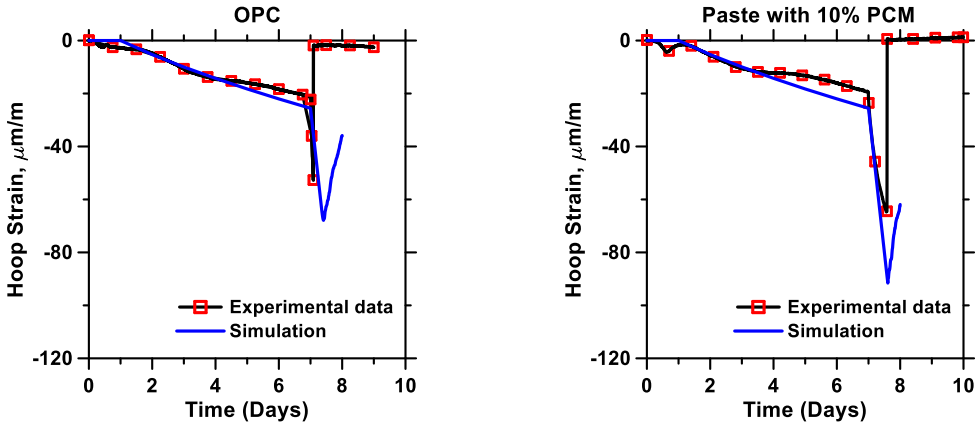

(a) (b)

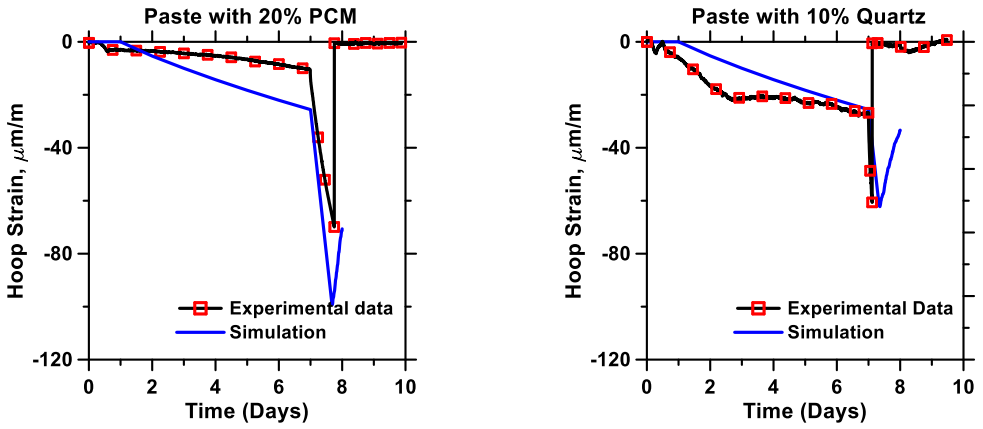

(c) (d)

Figure 5-8. Simulated Hoop Strain Development in the Inside of Invar Ring With Drying (a) Cement Paste, (b) Paste With 10% PCM Inclusions, (c) Paste With 20% PCM Inclusions, and (d) Paste With 10% Quartz Inclusion and Their Comparison With Experimental Results from (Wei, Falzone, Das, et al. 2017b) . The Simulated Results are the Mean Values of 10 Realizations.

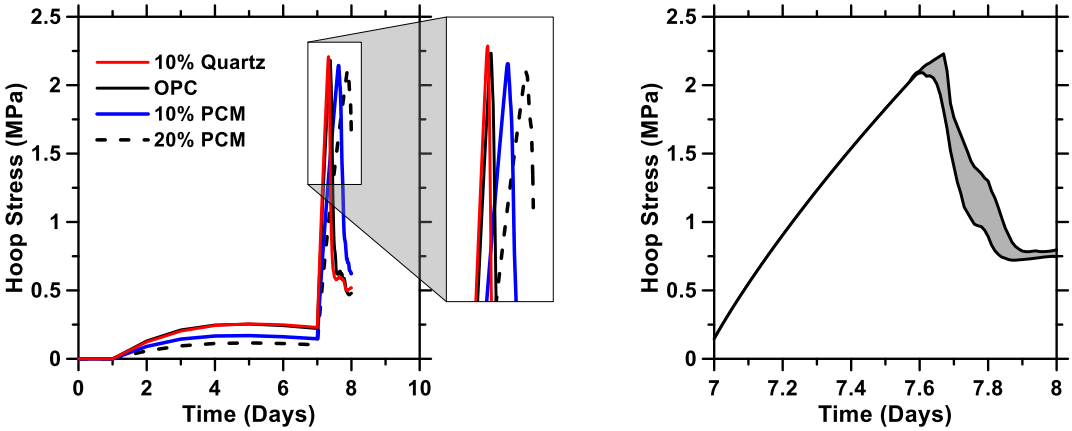

Figure 5-9. (a) Comparison of Development of Hoop Stress on the Top Layer for Different Pastes. The Lines Represent the Mean of 10 Realizations, and (b) Hoop Stress in the 10% PCM Paste With the Shaded Regions Show the Uncertainty in Time-to-Cracking.

Table 5-2. Estimated Time to Cracking Based on Experiments and Simulation for OPC Pastes With Inclusions

Mixture	**Time to Cracking (days)**		
	Experimental	Simulation (2D)	Simulation (3D)
OPC	7.09	7.07-7.10	7.34-7.39
10%PCM	7.51	7.47-7.57	7.61-7.68
20%PCM	7.53	7.63-7.73	7.81-7.92
10%Quartz	7.11	7.13-7.17	7.30-7.33

Figures 5-10 (a) and (b) show the hoop stresses at the instant of cracking for OPC paste and the paste with 10% PCM using the same seed value of the random generator of tensile strength. The distribution of hoop stress is very similar in both the specimens at the instant of cracking. In the OPC paste, the cracking initiated at 7.32 days, while in the paste with 10% PCM, it occurred at 7.52 days. The stress at the end of 8 days is also shown in Figures 5-10 (c) and (d). The isotropic damage index is shown in Figures 5-10 (e) and (f) for the OPC paste and the paste with 10% PCM respectively. Increased damage can be clearly observed in the plain OPC paste since the hoop stress increases faster in the OPC paste. This creates a situation where elements farther from the crack continue to carry the load and does not unload quickly. It can also be observed from Table 5-2, that the predicted time to cracking is higher for the paste with lower stiffness. However, the predicted time for same paste is slightly higher in the simulations. This is because, during the damage computations using Equation 4.1 in the finite element framework, the stress depends upon the previous state of damage. This makes the solution dependent on the time step between two iterations of the solver. In all the previous solutions, the chosen time step was 0.01 days. An extremely small time-step increases the computational effort by a significant margin. Figure 5-11 shows the isotropic damage index computed using three different time steps (0.1, 0.01 and 0.001 day) for the plain OPC paste. The solver took 10 minutes, 55 minutes and 24 hours to complete the simulations with the system configuration described earlier in this document. It can be noticed that damage is better localized as the time step is reduced. It is instructive to note that, in restrained ring tests of cementitious materials, a single crack is generally observed. Two-dimensional, plane stress simulations (not

considering moisture gradients) are able to accurately characterize the single cracking within manageable time steps. For computationally intensive 3D simulations, time step reduction is needed to capture the occurrence of a single crack. Moreover, cracking occurs in the top layer in the simulations, as is the case in the experiments, due to the high stresses caused by shrinkage of the top layers. Once cracking occurs, the drop in stiffness releases the tensile stress in the specimen. This reduces the compression which is acting on the ring and is indicated by the sudden drop in the hoop strain recorded by the strain gage. In the simulations, as explained above, the specimen continues to carry some load even after cracking occurs and thus the drop is not as sudden as observed in the experiments. Due to the residual stiffness in the specimen, the hoop strain also does not drop completely as in the experiments. A similar outcome has been reported in (Šmilauer et al. 2019) with the hoop strain in the ring not dropping instantaneously and damage localized to only the top layers. Figure 5-12 shows the development of hoop stress with time for different time steps chosen, using the same seed value of the random distribution of tensile strength. The peak stress and the time to cracking are found to reduce as the time step is reduced.

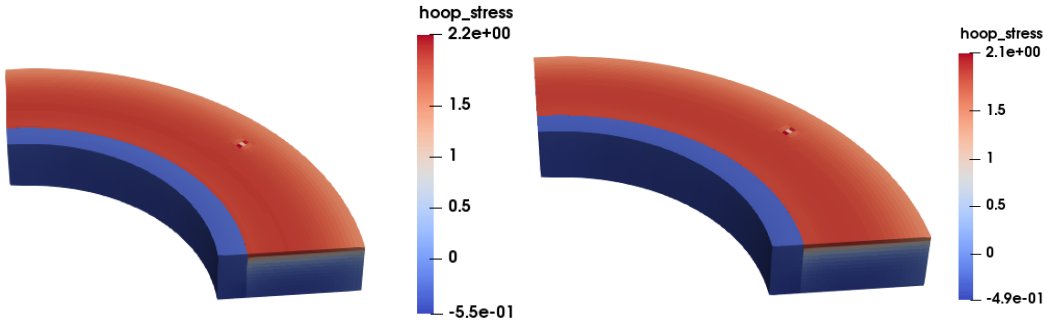

(a) (b)

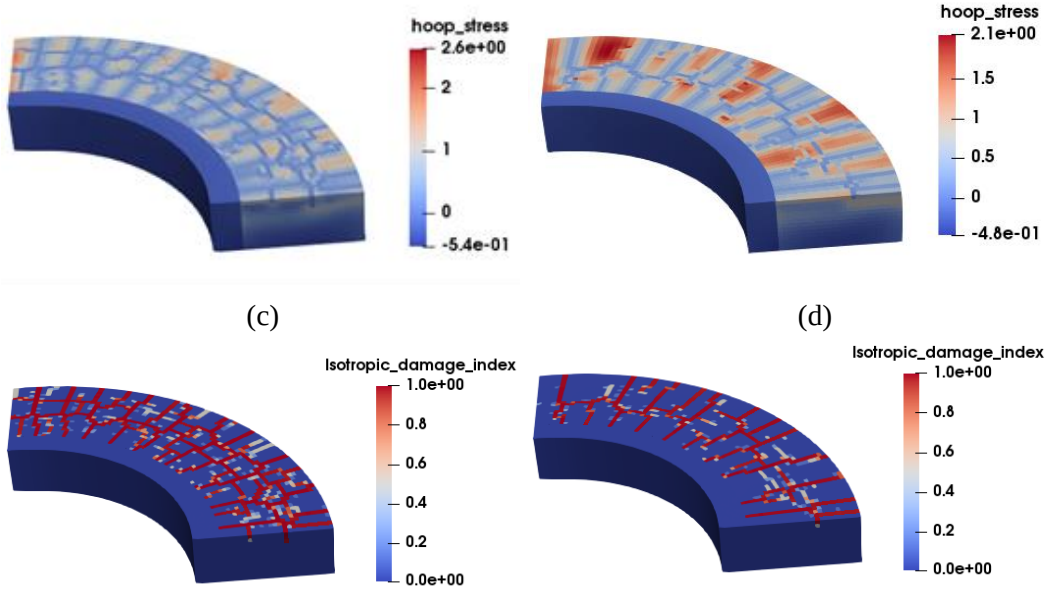

Figure 5-10. Hoop Stress at the Instant of Cracking in: (a) Plain OPC Paste, and (b) Paste With 10% PCM; Hoop Stress and After 8 days in: (c) Plain OPC Paste and (d) Paste With 10% PCM. Damage at the End of 8 Days for: (e) Plain OPC Paste, and (f) Paste With 10% PCM.

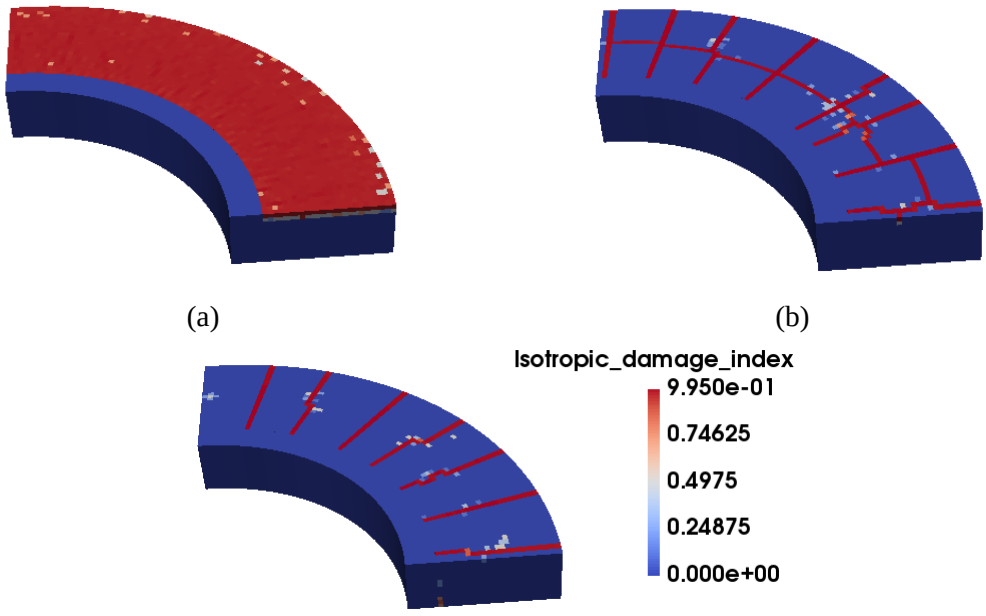

Figure 5-11. Isotropic Damage in the Specimen at the End of 8 Days When Time steps of: (a) 0.1 Day, (b) 0.01 Day and (c) 0.001 Day are Used.

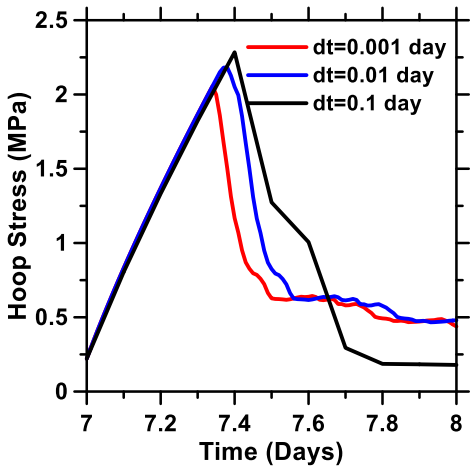

Figure 5-12. Hoop Stress in the OPC Paste When Simulations are Carried Out at Different Time Steps (the Hoop Stress Significantly Increases from Day 7 Since That is When the Experimental RH was Dropped from 87.5% to 50%).

5.5 Summary and Conclusions

This chapter describes a comprehensive finite element framework to model the restrained ring shrinkage test used to assess the cracking propensity of cementitious mixtures at early ages. A model based on the MOOSE framework was used to describe the early-age response of several cement pastes, including those containing soft or stiff inclusions. This model incorporates specific attributes required to simulate the early-age response of an aging, random, heterogeneous material undergoing drying shrinkage.

An eigenstrain was imposed on the FE model which considered moisture diffusion through the specimen. The relaxation function of cementitious pastes was determined based on the degree of hydration, which is independent of the presence of inclusions. Relaxation curves corresponding to different ages of loading thus obtained were used to determine the time-dependent Maxwell spring moduli for the selected systems. The aleatory uncertainty-based

approach adopted for the distribution of tensile strengths of the finite elements, helped to account for microscale heterogeneities that are influential in cracking, yet preserve the median strength of a finite volume of material.

The numerical model was validated for a series of cement pastes containing soft (phase change materials, PCM) or stiff (quartz) inclusions. The model adequately captured the delay in cracking time with the incorporation of soft inclusions. The influence of changing relative humidity is also considered in the simulation of pastes containing soft/stiff inclusions. The effect of time steps on the accuracy of the numerical results are also explained in this study. It is anticipated that the effect of using other compliant inclusions (e.g., expanded polystyrene for lightweight and energy absorbing composites, superabsorbent polymers for internal curing) on the cracking resistance of cementitious systems will be similar to those reported here – i.e., delaying the time to cracking and reducing the overall damage. The methodology demonstrated in this document to simulate restrained can be successfully adopted in such cases also. This eliminates the need for difficult experimental methods to determine viscoelastic parameters and provides a methodology wherein the designer can choose and optimize compliant or stiff inclusions with considerations of volume change and cracking also, in addition to the commonly considered mechanical properties. The model can be further used to examine the rate of stress development and cracking time for cement-based materials as a function of the restraining characteristics (ring material, thickness, and stiffness), material characteristics (elastic modulus, viscoelastic properties), exposure conditions (varying RH), and specimen size.

CHAPTER 6

VALIDATION OF NUMERICAL MODEL - IRRADIATED CONCRETE EXPERIMENTS

In this validation exercise, experimental results from published literature are used to validate the developed constitutive model by considering the coupled hygrothermal simulation and its effect on the creep, shrinkage kinetics. In this validation, aggregate and mortar will be modelled separately unlike previous examples where the material was considered homogenous.

6.1 Experimental Investigations

In this section, the studies carried out by Maruyama et al. (Maruyama et al. 2017) used for numerical simulations will be examined. Maruyama et al. (Maruyama et al. 2017) carried out a series of experiments to evaluate the reference values for fast neutron fluence and gamma ray dosage beyond which concrete is no longer considered sound. Presently, these values are taken as $1x10^{20}n/cm^2$ and $2x10^5$ kGy based on the irradiated concrete experimental studies collected by Hilsdorf et al. (Hilsdorf, Kropp, and Koch 1978). In a neutron radiation environment, secondary gamma rays are always present causing gamma heating. Thus, comprehensive tests were carried out to ascertain the effect of neutrons, which were supplemented with gamma ray tests and heating and drying effects on concrete. Two tests called Interaction test (IT) and Physical property test (PPT) were done in this study. The former deals with radiolysis of water in the cement paste while the latter deals with changes in the properties such as young's modulus, strength etc. PPT test also included heating and drying to include the effects of factors other than radiation, on the concrete. The fast neutron fluence was measured using monitoring wires placed inside the

capsules while the distribution of radiation in the vertical direction was obtained using MCNP5 FE code. The reactor JEEP II reactor at Norway's Institute for Energy Technology (IFE) was selected for neutron irradiation due to the low gamma heating values. The cylindrical specimen of size Φ40x60 mm with 13 mm dia (maximum) aggregate was selected to be tested in the irradiation rig. The specimen diameter was selected to reduce the difference in the internal and surface temperature, caused by gamma heating, thereby restricting the cracking of the specimen at the surface. The height was selected to fit maximum specimens inside the irradiation capsule. The clearance between specimen and internal surface of capsule was kept as 1% of sample diameter. The capsule was made of aluminum due to its high thermal conductivity to dissipate heat quickly and due to aluminum soft nature to avoid any damage to the specimen in case of any excessive expansion. High early strength cement with a w/c ratio of 0.5 was used to stabilize hydration at the end of 1 year to avoid radiation induced strength development. All the concrete and pastes specimens were kept in a sealed condition for 1 year at 20^{o}C. The cement paste specimens were then dried at 75^{o}C in thermostatic chamber for 1 week. To evaluate the expansion level of aggregate with α quartz content, irradiation tests were performed, with five kinds of siliceous rocks (namely GA, GB, GC, GD and GE with decreasing quartz content) and a representative limestone rock (GF), on specimen of size Φ10x10 mm.

Four concrete specimens (called CON-A) with GA aggregate and four specimens (called CON-B) with GB aggregate were irradiated simultaneously at four levels of neutron fluence i.e. 0.75, 1.5, 3 and 6 (10^{19}n/cm^2) at a dose of approximately 3.6x10^{12} n/cm^2/s. Along with concrete specimens, six cement pastes specimens (Φ10x10 mm) and six

aggregate specimens (Φ10x10 mm) of each type were also irradiated by placing them in Al sample holders. The fluence were achieved in ~30, 50, 155 and 320 days respectively and are referred as PPT-B, PPT-C, PPT-D and PPT-E. The number of days required to achieve the same fluence level varied slightly over the experiments due to outage. The results of PPT-E are not reliable as the specimen expanded a little more than expected, causing the fracture of the capsule holding the specimens and flooding by cooling water, hence the experimental result up to PPT-D will only be considered with $3x10^{19}$ n/cm^2 being the maximum fluence for the simulations. The results of experiments on concrete, hardened paste and aggregate are summarized in Table 6-1.

Table 6-1. Experimental Results by Maruyama et al.

Neutron Irradiation Test	
PPT- Concrete	
Mass Change	The mass change was similar (~3.5%) in both concrete specimens (CON-A and CON-B).
Length change	It was greater for Con-A (1% at highest fluence) than Con-B (0.5% at highest fluence) due to the higher amount of quartz in CON-A
Strength	45% and 35% and reduction in strength for CON-A and CON-B.
Elastic modulus	70% and 60% reduction in elastic modulus for CON-A and CON-B.
Cold Test- Concrete	
Compressive Strength	It was observed to be constant at 70 MPa for both concrete types at the end of 0, 50, 155 and 1000 days after sealed curing condition for one year and the days to testing at 20^{o}C. The 28- day compressive strength was 50 MPa
Young's Modulus	It was 37.5 GPa after 0, 50 and 155 days for both concrete types after one year and the days to testing at sealed curing condition.
Heating Test- Concrete	
Shrinkage	Exhibited slight shrinkage (~ 500 microns)
Strength	15% reduction in strength
Modulus	20% reduction in modulus
PPT-HCP	

Mass change	Mass increase was observed at low level of radiation (PPT-B), which was due to absorption of moisture during condensation of moisture inside the capsule and insufficient drying at 76^{o}C. PPT-C and PPT-D showed a decrease in mass due to elimination of condensation and mass increase was observed in PPT-E due to capsule flooding due to capsule fracture.
Length change	In early stages, the specimen absorbed moisture and exhibited swelling however starts shrinking at higher fluence. The data seems unreliable though.
Vickers Hardness	It increased with fluence indicating cement paste has high resistance against radiation.
PPT-Aggregates	
Length change	In early stages, the specimen absorbed moisture and exhibited swelling however starts shrinking at higher fluence. The data seems unreliable though.
XRD data	It showed that the diffraction peaks grew smaller and shifted to the small angle region with increasing fluence indicating structural collapse and widened atomic spacing.

6.2 Simulation Approach

The entire simulation is done in two stages as shown in Figure 6-1. Stage 1 consists of using a coupled thermo-hygral model (Zdeněk P. Bažant, Chern, and Thonguthai 1982; Bazant and Thonguthai 1978; Zdeněk P. Bažant and Thonguthai 1979) to compute temperature and relative humidity fields and together with the radiation field form an input for stage 2 which consists of a mechanical model and computes the strain based on the applied fields. The applied temperature and moisture content/pore relative humidity profiles were calculated based on the deposited energy from the irradiation. These fields are then applied to estimate the creep, shrinkage and thermal strains on the mortar and radiation induced volumetric strain on the aggregate in the mechanical model which are then converted to stress fields using appropriate constitutive law. There is a dearth of information in the open literature when it comes to concrete under irradiated conditions as

only a few tests have been carried out. The limited tests, whenever available, also corresponds to different type of radiation dosages, concrete mix, aggregate types, curing age and environmental condition during the irradiation scenario (Field, Remec, and Pape 2015; Le Pape, Field, and Remec 2015). In the current work, the proposed framework is validated with the experimental results of Maruyama et al. (Maruyama et al. 2017), which to date feature the most comprehensive set of tests on irradiated concrete. However significant gaps remain and as a result, a lot of approximations were either made or models pertaining to concrete under non irradiated scenarios are used.

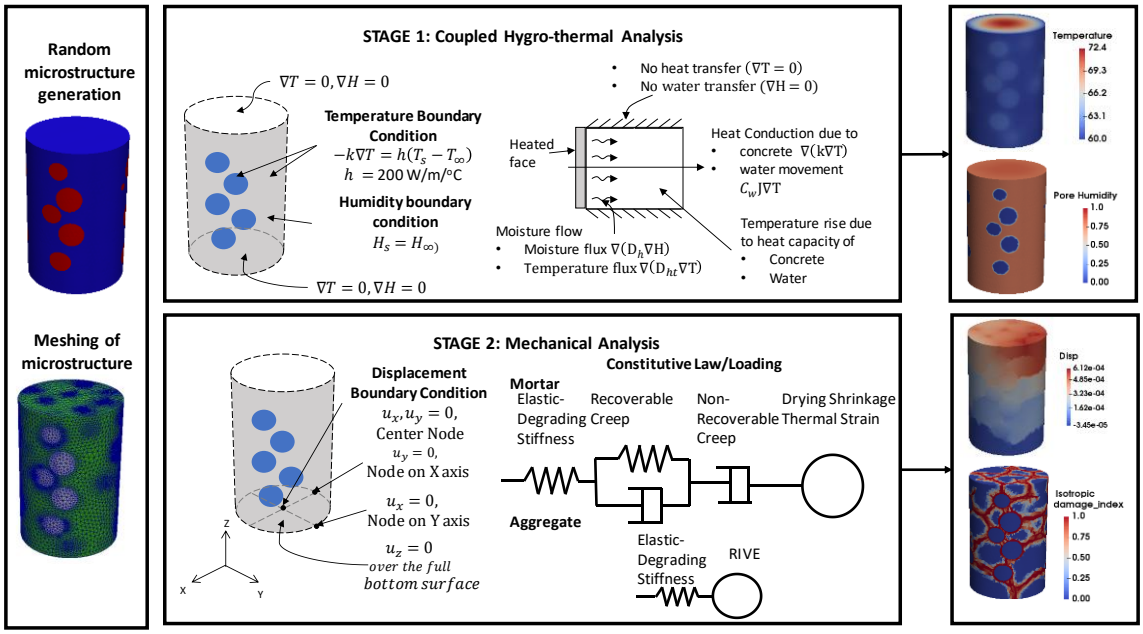

Figure 6-1. Meso-Scale Microstructure-Based FE Framework to Detect Damage in Concrete With Expansive Aggregate.

6.3 Microstructure and Mesh Generation

The microstructure has been generated based on the particle size distribution of the coarse aggregates provided by Maruyama et al. (Maruyama et al. 2017) using the microstructure generation algorithm as found in (Lubachevsky and Stillinger 1990). Meshing has been

done using 378589 four noded tetrahedral elements using the geometry adaptive meshing scheme. The volume fraction was further verified by calculating the volume of elements that correspond to aggregate and mortar. The volume fraction of 0.34 was achieved against the 0.38 used in the experiments. The finite element mesh, boundary conditions and the loading conditions for both stages are shown in Figure 6-1.

6.4 Material Model for Aggregate

Aggregates are treated as linear elastic material undergoing radiation induced volumetric expansion and damage due to neutron impingement as shown by XRD data.

6.4.1 Elasticity

The modulus of aggregate reduces under neutron irradiation. However, no measurements of decrease of elastic modulus were carried out due to neutron irradiation. Elleuch et al. (Elleuch, Dubois, and Rappeneau 1972) carried out the experiments on serpentine aggregates and found that the pulse velocity, v_m reduces from 7200 m/sec to 4720 m/sec (see Figure 6-2) as neutron fluence, φ changes from 0 to 10 (10^{19} n/cm^2). Most of the reduction occurs in the initial phase up to 1 (10^{19} n/cm^2). The following equation has been formulated to capture this effect

$$v_m = \begin{cases} -1360n + 7200 & \varphi < \dfrac{10^{19}\mathrm{n}}{\mathrm{cm2}} \\ 5840\varphi^{-0.1} & \varphi > \dfrac{10^{19}\mathrm{n}}{\mathrm{cm2}} \end{cases} \tag{6.1}$$

In the absence of experimental data, the same reduction of elastic modulus is assumed to occur in the aggregates GA and GB as these aggregates have typically high amount of quartz content (>40%). The elastic modulus is proportional to the square of the pulse velocity. The variation of elastic modulus with neutron fluence is then given by:

$$E_{agg}(\varphi) = E_{stat}\left(\frac{v_m(\varphi)}{(v_m(\varphi = 0)}\right)^2 \quad (6.2)$$

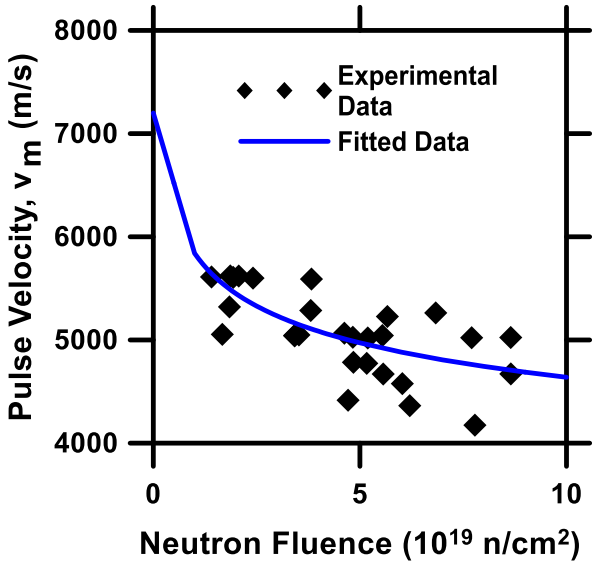

Figure 6-2. Pulse Velocity Against Neutron Fluence for Serpentine Aggregates as per Elleuch et al. (Elleuch, Dubois, and Rappeneau 1972)

6.4.2 Radiation Induced Volumetric Expansion

It has been observed that aggregates with covalent bonds (siliceous aggregates) are more susceptible to radiation induced expansion than aggregates with ionic bonds. Quartz, which is present in aggregates is more susceptible to radiation induced swelling, however, other minerals, texture, grain boundaries also influence the rate of expansion (Maruyama et al. 2017). As these effects are difficult to be considered at this stage, we will consider uniform volumetric expansion of aggregates. It is to be noted that temperature also affects the degree of quartz metamictization (Bykov et al. (Bykov et al. 1981)). Bykov et al. (Bykov et al. 1981) found out that the expansion decreases with increasing temperature indicating that thermal heating heals the damage in the aggregate. They considered the thermal

healing at high temperature and expressed RIVE using the nucleation and growth model (shown in Figure 6-2) as,

$$\varepsilon_{\Phi} = \varepsilon_{max}\left(1 - exp\left(-\left(\frac{\varphi}{K(T)}\right)^{d}\right)\right) \tag{6.3}$$

where, ε_{max} is the maximum expansion volume as observed in experiments (0.18, 0.15 for GA and GB aggregates (Maruyama et al. 2017)), φ is the fast neutron fluence (n/cm2), $K(T)$ is the fast neutron fluence when expansion reaches half the maximum expansion volume (n/cm2), T is the temperature (in Kelvin), d is the dimension coefficient taken as 2.38 based on Field et al. (Field, Remec, and Pape 2015). $K(T)$ is given by,

$$K(T) = 0.45 \times 10^{20} \times \frac{\exp(2000/298)}{\exp(2000/\mathrm{T})} \tag{6.4}$$

The thermal deformation which is negligible in comparison to RIVE is ignored in the simulations where radiation is applied, however it is considered in the cases where only thermal heating occurs. Moreover, elevated temperature causes healing and thus controls RIVE which is considered in this study. Thermal healing is also enhanced under low neutron flux conditions. This effect is not considered in the current work due to high constant flux in the test reactors, however to simulate real-world reactor setting (with low and varying flux condition) the three-phase model proposed by Nakano et al. 2006 (Nakano, Muto, and Tanabe 2006) could be used, in which expansion also depends upon the neutron flux.

6.4.3 Thermal Expansion

The thermal deformation is negligible in comparison to RIVE. However, it needs to be considered for specimens which are only under heating. It is well known that thermal

deformation is linear with the temperature with the coefficient of thermal expansion, α_a relating the thermal expansion with the applied temperature.

$$\varepsilon_t = \alpha_a(T - T_0) \tag{6.5}$$

where, ε_t is the thermal strains, T, T_0 are the applied temperature and the reference temperature (in ^oC).

6.5 Material Models for Mortar

Mortar has been modeled as an elastic material undergoing stiffness degradation, drying shrinkage, thermal expansion and long-term creep owing to the elevated temperature.

6.5.1 Drying Shrinkage

The drying shrinkage of cementitious materials can be directly related to the pore water content or the internal pore relative humidity of the specimen (Neithalath, Pease, and Attiogbe 2005; Zdeněk P. Bažant, 1988).

$$\varepsilon_{ld}(t) = \varepsilon_{SH,\infty}(0.97 - 1.898(H(x,t) - 0.2)^3) \tag{6.6}$$

where, $\varepsilon_{SH,\infty}$ is the free shrinkage coefficient which is equal to maximum shrinkage obtained at infinite time.

6.5.2 Creep

Based on the experiments, McDowall (McDowall 1972) concluded that the creep reduces under gamma irradiation while shrinkage increases. There is not much data in open literature about the effect of irradiation on the creep mechanism in concrete, hence its effect will be ignored in the present simulations. However the effect of humidity and temperature will be considered here as in (A. Giorla et al. 2015). A single Kelvin Voigt chain with an additional dashpot is used to model recoverable and non-recoverable creep as was done in a previous study (A. Giorla et al. 2015). The effect of elevated temperature on creep is

considered using Arrhenius law, such that the Kelvin-Voigt characteristic time is given by (Zdeněk P. Bažant 1983; Zdeněk P. Bažant and Baweja 1995):

$$\tau_p(T) = \exp\left[T_{act}\left(\frac{1}{T} - \frac{1}{T_0}\right)\right]\tau_p(T = T_0) \tag{6.7}$$

where, T_{act} is the activation temperature for creep (5000K (Zdeněk P. Bažant and Baweja 1995)). 'τ_p' is the characteristic time of the specimen and is taken as 2 days (Hummel 1959). The viscosity tensor for the Kelvin Voigt model is calculated by considering the viscosity in terms of relative humidity $'h'$ as,

$$\eta_p(h) = \left[\left(\frac{1-h}{h_C} + exp\left(\frac{1-h}{h_C}\right)\right)\right]\eta_p(h = 1) \tag{6.8}$$

where, h_C is a material property equal to 0.2 (A. Giorla et al. 2015). η_p is taken as 40 GPad (A. Giorla et al. 2015).

6.5.3 Thermal Expansion

The thermal expansion of mortar is given by,

$$\varepsilon_t = \alpha_m(T - T_0) \tag{6.9}$$

where, ε_t is the thermal strains, T is the applied temperature and T_0 is the reference temperature. α_m is the thermal expansion coefficient of mortar which is usually greater than the coefficient of thermal expansion of aggregate. It depends on the amount of moisture present in the pore system or equilibrium relative humidity (Grasley and Lange 2007; Maruyama and Igarashi 2015). However, this effect is not considered due to lack of experimental data.

6.5.4 Post Peak Response

Mortar is a brittle material. It fails instantaneously when cracked, indicating very low amount of fracture energy. However, the mechanism of failure and the fracture energy are highly sensitive to the rate of application of load, temperature and relative humidity (Weerheijm and Van Doormaal 2007). At lower rates, creep occurs in the fracture process zone releasing the buildup of energy. This has also been shown experimentally on concrete by Bazant and Gettu (Zdenek P. Bažant and Gettu 1992). The peak strength for a faster applied load is also higher than the slowly applied load. In faster load rates, crack passes through the aggregate and not around it. As the strength of aggregate is higher, it causes more resistance for the crack to go through the aggregate than around it. There have been extensive studies on the rate dependence behavior of concrete, but extensive data is not available for cement mortar particularly at lower rate of loading. In the radiation environment, the growth of crack will be slow due to the slow expansion of aggregates with the radiation. The isotropic model is used in this approach because of the flexibility with which the damage behavior can be simulated by specifying the softening function. However, it has been well been noted that only specifying the fracture strain cause convergence issues and makes it mesh sensitive. Introducing fracture mechanics approach using the concept of fracture energy removes this issue. This has been discussed in detail in Chapter 4.

6.6 Finite Element Implementation

The FE model with boundary condition is shown in Figure 6-1. The boundary condition has been chosen to avoid any rigid body modes. The Agave cluster of the HPC at Arizona State University was employed to carry out the simulations using a single node of 28 cores and 128 GB RAM which took approximately 1 and 24 hours for stage 1 and stage 2 analysis

to complete. A combined creep damage algorithm taking into consideration the above formulations was incorporated in MOOSE framework, an open source object oriented finite element analysis toolkit developed by Idaho National Lab (Permann et al. 2019). The formulation considers one step finite difference scheme to estimate the viscoelastic effect and consider linear isotropic damage based on fracture energy to simulate the effect of cracking as detailed in Chapter 4. The implementation of coupled temperature and humidity model could be found in Chapter 3.

6.7 Input Parameters

6.7.1 Aggregates

The dynamic modulus GA and GB are given as 65 GPa and 81 GPa with a Poisson ratio of 0.28 and 0.25 (GA and GB _Chapter 4 notation G3 and G5, aggregate A and C notation Table 35) [2]. The static modulus is observed to be lower than the dynamic modulus by about 10% [5]. Thus, we reduce the value by 10% to estimate the static modulus as 58.5 GPa and 72.9 GPa. The variation of modulus with neutron fluence is calculated as per Equation 6.2. The Poisson's ratio is best estimated from the dynamic measurements [4] hence the value of 0.28 and 0.25 is taken for GA and GB. The radiation induced volumetric expansion is computed using Equation 6.3, 6.4 and shown in Figure 6-3. The coefficient of thermal expansion is related to the amount of quartz in the material (Maruyama et al. 2017) (GA and GB has 92% and 47% quartz respectively) using the following equation (Maruyama et al. 2017)

$$\alpha_a = 0.058x + 4.2 \tag{6.10}$$

where, x is the amount of quartz (in %) in aggregate. α_a is the thermal expansion coefficient (in μ/ºC). This gives 9.5 μ/ºC and 6.9 μ/ºC as the thermal expansion coefficient for GA and GB.

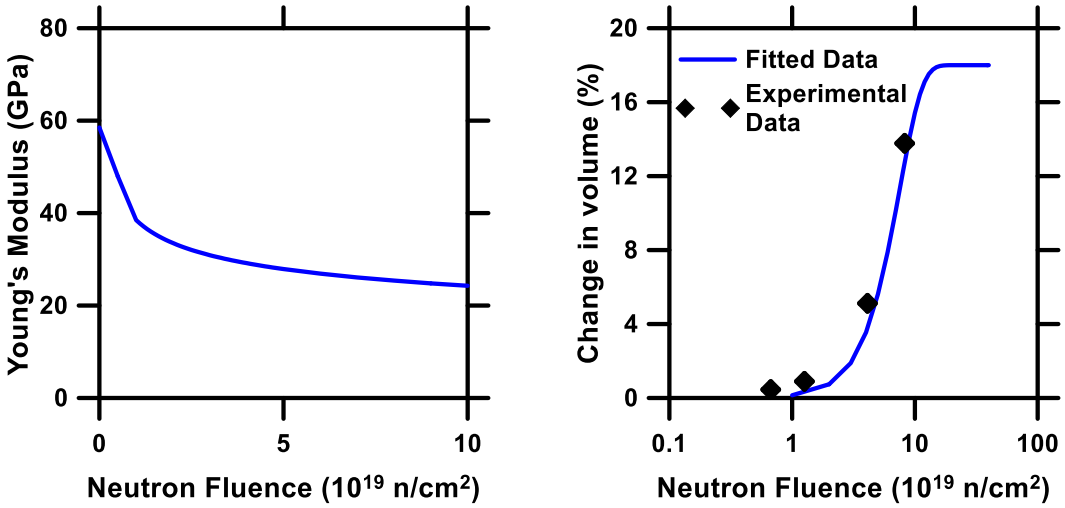

Figure 6-3. Young's Modulus and RIVE Against Neutron Fluence for GA.

6.7.2 Mortar

The cement mortar is modeled as an elastic material (E_m=30.25 GPa) undergoing drying shrinkage, thermal deformation and creep owing to the high temperature (T~70ºC). As no information on Poisson's ratio was available, we have taken typical value of cement mortar which is 0.2. The Young's modulus is affected with temperature and humidity. Maruyama found that the modulus of high early strength cement paste mix (E_m = 12MPa) is fairly constant at high temperature upto 90ºC (Maruyama et al. 2014). The thermal expansion coefficient of mortar is calculated by upscaling the thermal expansion coefficient of cement paste using the simple rule of mixture (Maruyama and Igarashi 2015) as:

$$\alpha_m = \frac{1}{\frac{1-V_s}{\alpha_p} + \frac{V_s}{\alpha_s}} \tag{6.11}$$

where, V_s is the volumetric ratio of sand in mortar (0.5 in this case). α_s, α_p are the thermal expansion coefficients of paste (30 μ/ °C) and sand (6.95 μ/ °C, using Equation 6.10 and x=47.35 as per (Maruyama et al. 2017)). This gives the coefficient of thermal expansion as 11 μ/ °C. The bending strength of the paste attains fluctuates between 10 and 15 MPa for temperature between 40 and 90°C. At 70°C the bending strength, was 16 MPa for the paste mix used and is considered in the present study. At 100% RH and 20°C this value was approximately 6 MPa. The fracture energy also changes at high temperature. However, no measurement of fracture energy of mortar or cement paste is carried out. As a result, the fracture energy is calibrated from the thermal treatment tests and is taken as 250 N-m/m^2. The input parameters are also tabulated in Table 6-2.

Table 6-2. Constitutive Parameters Used in the Simulation of Irradiated Concrete

Variable	Value	Unit	Variable	Value	Unit
Aggregates			$\varepsilon_{sh,\infty}$	-4000	μm/m
α_a	9.5	μm/m	f_t	16	MPa
T_0	20	°C	E_M	30.25	GPa
E_a	58.5	GPa	η_p	40	40 GPa-days
ν_a	0.28		τ_p	2	days
ε_{max}	0.18,0.15		ν_p	0.2	
d	2.38		h_C	0.2	
ρ_a	2600	kg/m^3	T_{act}	5000	K
C_a	1100	J/kg/°C	ρ_m	2231	kg/m^3
k_a	3	W/m/°C	C	1100	J/kg/°C
h_{surf}	200	W/m^2°C	k	3	W/m/°C
Concrete			D_1	3x10^{-10}	m^2/s
T_0	20	°C			
Q	211111	J/kg/s			
Mortar			p_{vs}	2500	Pa
α_m	11	μm/m	T_{env}	50	°C
G_F	250	N-m/m^2	β'	0.1	
			T_0	20	°C

6.8 Numerical Simulations & Results

The microstructure and mesh used in the simulations along with the boundary conditions are shown in Figure 6-1.

6.8.1 Stage 1 Analysis

A coupled hygro-thermal analysis is carried out in this stage to compute the variation of temperature and pore humidity inside the specimen. In actual condition, 9 concrete specimens (1 concrete specimen was a dummy specimen to measure temperature) were irradiated together inside a double aluminum capsule with coolant water flowing between the inner and our edge of capsule. This helped in reducing the temperature inside the specimen which is measured at the center of the top specimen. Moreover, water was released from the specimen once the pressure exceeded 1.25 bar. It was difficult to characterize the boundary condition as it would require modelling of the all the specimens with the capsule including the flowing coolant water. Instead of carrying out such a complex analysis, some simplifying assumptions were made. The thermal conductivity of the surface was calibrated so that the simulations can match the temperature at the center of the specimen which reached 72^{o}C quickly in the experiments. This was reached in 16 hours as per the simulations and remained constant thereafter. Figure 6-4 shows the temperature profile in the specimen at the start and at 16 hours. The aggregates show slightly higher temperature than mortar at the same location due to their higher thermal conductivity.

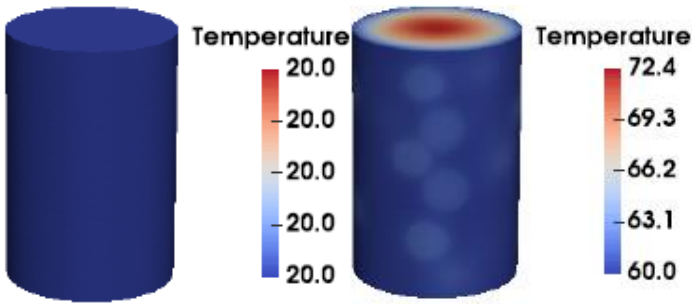

Figure 6-4. Evolution of Temperature in the Specimen at 0 and 16 Hours. It Achieves a Steady State Condition at the End of 16 Hours.

As the reaction proceeded the moisture released by the specimen kept on reducing. This would mean that the environmental humidity was changing rapidly in the space between the specimen and capsule. This was also flushed out once the pressure in the region reached 1.25 bar. The pressure was released more frequently in the beginning due to higher available moisture in the specimen and consequently higher gas release. In the simulations a simplification was made, the environmental humidity was calibrated to drop at a rate such that the total water released by the specimen matched with those in the experiments. Figure 6-5(a) shows the assumed environmental humidity profile while Figure 6-5(b) shows the experimental and simulated water released. The experimental water released consists of the water which forms the gas released and water absorbed on condenser for PPT-D specimen. The gas is assumed to consists of 2/3 hydrogen. It is converted to molar mass of water assuming STP condition (1 molar mass of hydrogen= 22.4 liter =1 molar mass of water = 18-gram water). Figure 6-6 shows the moisture inside the specimen at different times. Currently, there is no way to validate the pore humidity condition as no measurements of humidity or water content are made during irradiation of concrete.

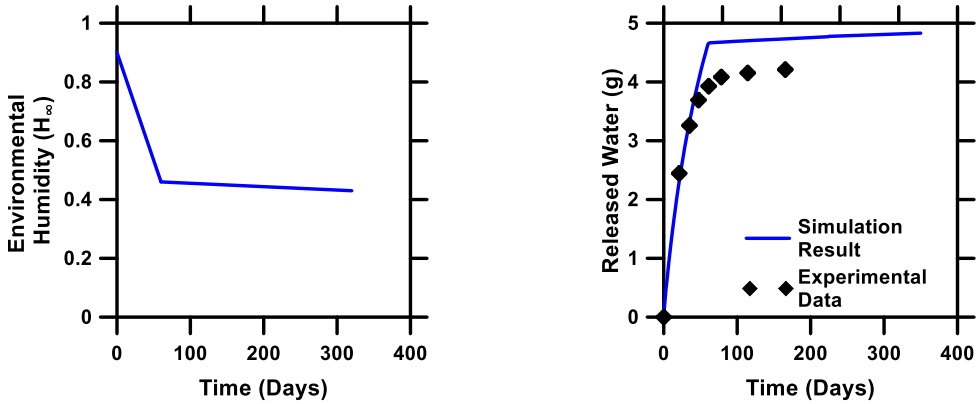

Figure 6-5. (a) Assumed Environmental Humidity and (b) Experimental and Simulated Amount of Water Released.

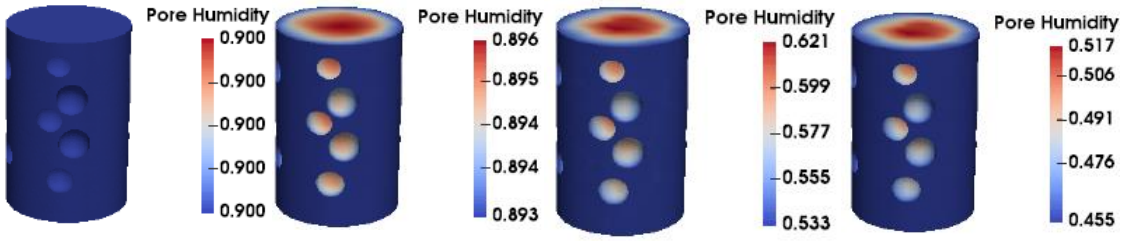

Figure 6-6. Evolution of Pore Relative Humidity in the Specimen at 0, 10, 50 and 100 Days. The Aggregates were Removed as Their Relative Humidity is not Considered in the Simulations.

6.8.2 Stage 2 Analysis

Once the temperature and humidity profile are known mechanical analysis could be carried out. The radiation dose is considered constant along the depth of the specimen as it doesn't change appreciably over one specimen. The mesh and boundary condition are shown in Figure 6-1. The boundary condition has been chosen to avoid any rigid body modes. The simulated results are compared with the experimental results in the form of length change and damage in the specimen. The computed length change from the experiment compared with simulations is shown in Figure 6-7(a) while the damage is compared in Figure 6-7(b). The simulated length change corresponds to the average of the nodes on the top surface.

The damage is volume average of the cement paste and aggregate individually. The damage at the end of 300 days is shown in Figure 6-8.

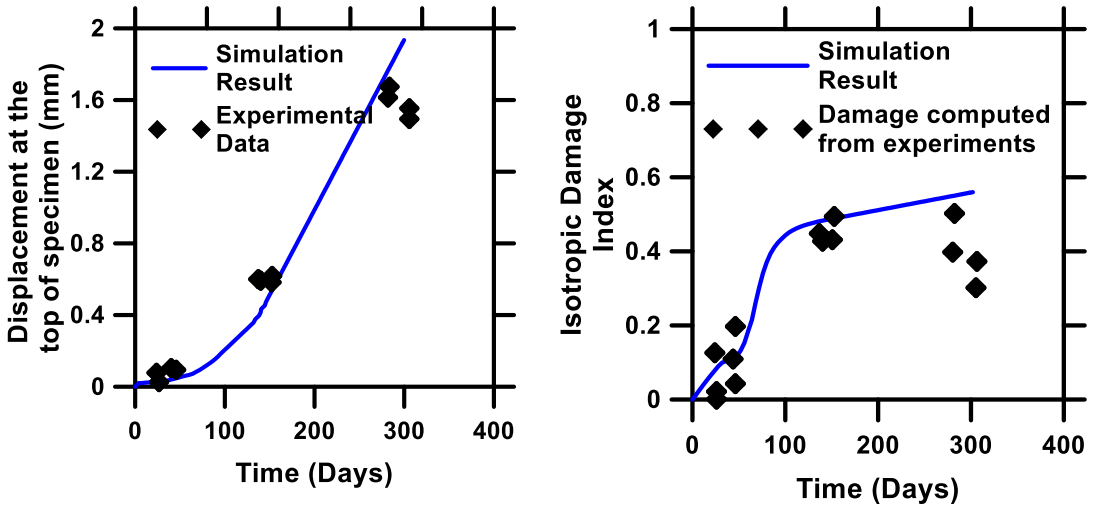

Figure 6-7. Experimental and Simulated (a) Displacement and (b) Isotropic Damage Index.

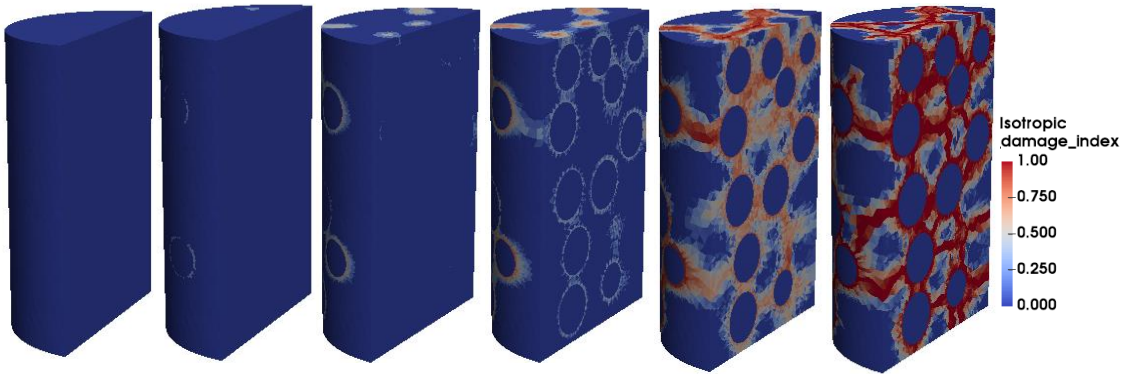

Figure 6-8. Progression of Damage in the Specimen at the End of 0, 48, 64, 80 and 150 Days.

6.9 Summary and Conclusions

This chapter presents a comprehensive finite element framework to model the concrete under neutron irradiation. The framework computes damage under irradiation induced expansion of concrete in two stages. In the first stage, the temperature and humidity profile in the specimen are computed using a coupled hygro-thermal model. This moisture transport characteristics are accounted using water mass balance equations, empirical

sorption isotherms for concrete. The effect of thermal gradient on the moisture diffusion is also considered. The thermal transport considers the heat balance and consider the effect of all the constituents of concrete including free water. The temperature, humidity profile computed from the first step along with the radiation dose forms an input to the second stage of analysis. In the second stage, the effect of three input parameters on the mechanical properties are considered. Radiation causes aggregate to expand which is characterized using nucleation and growth model. It also causes aggregates modulus to reduce. The effect of temperature and humidity on drying shrinkage and creep kinetics are also considered.

CHAPTER 7

CONCLUSIONS

The key contributions and conclusions from this study are outlined below

1. A coupled creep damage model was incorporated in MOOSE to simulate failure in concrete specimens. The developed model considers linear viscoelasticity using generalized Maxwell model or generalized Kelvin Voigt model while damage is considered using an isotropic approach. To avoid convergence issues with vanishing energy dissipation, the characteristic length of each element is used such that the energy release rate for each element remains constant. The proposed formulation captures the interaction between creep and damage, and with a modification in the elastic damage model, can capture the behavior of concrete under slowly applied loading rates.
2. The model was then validated against the test results of notched specimens under uniaxial loading for the damage-only case. The model adequately captures the peak and post-peak behavior of the specimen, thus validating the damage model. The creep-damage model was also used to simulate the results of experimental tests whose duration varied from minutes to a few days. The results showed that a strong coupling between creep and damage overestimates the damage and underpredicts the constitutive response. Parametric simulations using various values of the creep-damage parameter showed that only about 10% of the creep strain contributes towards damage for the cases considered in this study.
3. The numerical model was validated for early age shrinkage of a series of cement pastes containing soft (phase change materials, PCM) or stiff (quartz) inclusions in

a restrained shrinkage test. The model adequately captured the delay in cracking time with the incorporation of soft inclusions. The influence of changing relative humidity is also considered in the simulation of pastes containing soft/stiff inclusions.

4. The numerical model was validated for irradiated concrete in a test reactor. A meso scale approach was adopted and aggregates and mortar were modeled separately. A coupled hygro-thermal model was used to estimate the humidity and temperature distribution inside the specimen. Radiation dose was assumed constant across the depth of the specimen. The simulated damage and expansion matched quite well with the experimental results. This showed that the entire framework seems promising and present the first step towards having a matured tool for predicting irradiation induce damage in concrete.

REFERENCES

Ababneh, Ayman, Farid Benboudjema, and Yunping Xi. 2003. "Chloride Penetration in Nonsaturated Concrete." *Journal of Materials in Civil Engineering* 15 (2): 183–91. https://doi.org/10.1061/(ASCE)0899-1561(2003)15:2(183).

Acker, Paul, and Franz-Josef Ulm. 2001. "Creep and Shrinkage of Concrete: Physical Origins and Practical Measurements." *Nuclear Engineering and Design* 203 (2): 143–58. https://doi.org/10.1016/S0029-5493(00)00304-6.

Aguayo, Matthew, Sumanta Das, Amit Maroli, Nihat Kabay, James C. E. Mertens, Subramaniam D. Rajan, Gaurav Sant, Nikhilesh Chawla, and Narayanan Neithalath. 2016. "The Influence of Microencapsulated Phase Change Material (PCM) Characteristics on the Microstructure and Strength of Cementitious Composites: Experiments and Finite Element Simulations." *Cement and Concrete Composites* 73 (Oct): 29–41. https://doi.org/10.1016/j.cemconcomp.2016.06.018.

Alexander, SC. 1963. "Effects of Irradiation on Concrete. Final Results." *Atomic Energy Research Establishment, Harwell* 34.

Altoubat, S. A., and D. A. Lange. 2001. "Creep, Shrinkage, and Cracking of Restrained Concrete at Early Age." *ACI Materials Journal* 98 (4): 323–31.

Bai, Yu, Yao Wang, and Yunping Xi. 2020. "Modeling the Effect of Temperature Gradient on Moisture and Ionic Transport in Concrete." *Cement and Concrete Composites* 106 (Feb): 103454. https://doi.org/10.1016/j.cemconcomp.2019.103454.

Bažant, Zdeněk P. 1999. "Size Effect on Structural Strength: A Review." *Archive of Applied Mechanics* 69: 703–25.

Bažant, Zdeněk P., and L. J. Najjar. 1971. "Drying of Concrete as a Nonlinear Diffusion Problem." *Cement and Concrete Research* 1 (5): 461–73. https://doi.org/10.1016/0008-8846(71)90054-8.

Bažant, Zdeněk P. 1983. "Mathematical Model for Creep and Thermal Shrinkage of Concrete at High Temperature." *Nuclear Engineering and Design* 76 (2): 183–91. https://doi.org/10.1016/0029-5493(83)90133-4.

Bažant, Zdeněk P. 1995. "Creep and Damage in Concrete." *Materials Science of Concrete IV*, 355–89.

Bažant, Zdeněk P. 1988 "Mathematical Modeling of Creep and Shrinkage of Concrete." *John Wiley & Sons, Inc., New York, N.Y.*

Bažant, Zdeněk P., F Asce, Ted B Belytschko, M Asce, Ta-Peng Chang, and S M Asce. 1984. “Continuum Theory for Strain-Softening.” *J. Eng. Mech.* 110 (12): 14.

Bažant, Zdeněk P., and Sandeep Baweja. 1995. “Justification and Refinements of Model B3 for Concrete Creep and Shrinkage 2. Updating and Theoretical Basis.” *Materials and Structures* 28 (8): 488–95. https://doi.org/10.1007/BF02473171.

Bažant, Zdenek P., and Sandeep Baweja. 2000. “Creep and Shrinkage Prediction Model for Analysis and Design of Concrete Structures: Model B3.” *ACI Special Publications* 194: 1–84.

Bažant, Zdeněk P., Jenn-Chuan Chern, and Werapol Thonguthai. 1982. “Finite Element Program for Moisture and Heat Transfer in Heated Concrete.” *Nuclear Engineering and Design* 68 (1): 61–70. https://doi.org/10.1016/0029-5493(82)90040-1.

Bažant, Zdeněk P., and Ravindra Gettu. 1992. “Rate Effects and Load Relaxation in Static Fracture of Concrete.” *ACI Materials Journal* 89 (5): 457–68.

Bažant, Zdeněk P., and Yuan-Neng Li. 1997. “Cohesive Crack with Rate-Dependent Opening and Viscoelasticity: I. Mathematical Model and Scaling.” *International Journal of Fracture* 86 (3): 247–65. https://doi.org/10.1023/A:1007486221395.

Bažant, Zdeněk P., and Feng-Bao Lin. 1988. “Nonlocal Smeared Cracking Model for Concrete Fracture.” *Journal of Structural Engineering* 114 (11): 2493–2510.

Bažant, Zdeněk P., and B. H. Oh. 1983. “Crack Band Theory for Fracture of Concrete.” *Matériaux et Constructions* 16 (3): 155–77. https://doi.org/10.1007/BF02486267.

Bažant, Zdeněk P., and Gilles Pijaudier-Cabot. 1989. “Measurement of Characteristic Length of Nonlocal Continuum.” *Journal of Engineering Mechanics* 115 (4): 755–67. https://doi.org/10.1061/(ASCE)0733-9399(1989)115:4(755).

Bažant, Zdenek P., and Jaime Planas. 1997. *Fracture and Size Effect in Concrete and Other Quasibrittle Materials*. CRC Press.

Bažant, Zdeněk P., and Santosh Prasannan. 1989. “Solidification Theory for Concrete Creep. I: Formulation.” *Journal of Engineering Mechanics* 115 (8): 1691–1703. https://doi.org/10.1061/(ASCE)0733-9399(1989)115:8(1691).

Bazant, Zdenek P., and Werapol Thonguthai. 1978. “PORE PRESSURE AND DRYING OF CONCRETE AT HIGH TEMPERATURE.” *ASCE J Eng Mech Div* 104 (5): 1059–79.

Bažant, Zdeněk P., and Werapol Thonguthai. 1979. “Pore Pressure in Heated Concrete Walls: Theoretical Prediction.” *Magazine of Concrete Research* 31 (107): 67–76. https://doi.org/10.1680/macr.1979.31.107.67.

Bažant, Zdeněk P., and S. T. Wu. 1974. “Rate-Type Creep Law of Aging Concrete Based on Maxwell Chain.” *Matériaux et Constructions* 7 (1): 45–60. https://doi.org/10.1007/BF02482679.

Bažant, Zdeněk P., and Spencer T. Wu. 1973. “Dirichlet Series Creep Function for Aging Concrete.” *ASCE J Eng Mech Div* 99 (EM2): 367–87.

Bažant, Zdenek P., and Spencer T. Wu. 1973. “Dirichlet Series Creep Function for Aging Concrete.” *ASCE J Eng Mech Div* 99 (EM2): 367–87.

Bažant, Zdeněk P., and Yunping Xi. 1991. “Statistical Size Effect in Quasi-brittle Structures: II. Nonlocal Theory.” *Journal of Engineering Mechanics* 117 (11): 2623–40. https://doi.org/10.1061/(ASCE)0733-9399(1991)117:11(2623).

Bear, Jacob. 1991. “Modelling Transport Phenomena in Porous Media.” In *Convective Heat and Mass Transfer in Porous Media*, edited by Sadik Kakaç, Birol Kilkiş, Frank A. Kulacki, and Faruk Arinç, 7–69. NATO ASI Series. Dordrecht: Springer Netherlands. https://doi.org/10.1007/978-94-011-3220-6_2.

Bentz, D.P. 2008. “A Review of Early-Age Properties of Cement-Based Materials.” *Cement and Concrete Research* 38 (2): 196–204. https://doi.org/10.1016/j.cemconres.2007.09.005.

Bernard, F., S. Kamali-Bernard, and W. Prince. 2008. “3D Multi-Scale Modelling of Mechanical Behaviour of Sound and Leached Mortar.” *Cement and Concrete Research* 38 (4): 449–58. https://doi.org/10.1016/j.cemconres.2007.11.015.

Blosser, TV, GW Bond, LA Lee, DT Morgan, JF Nichols, RC Reid, AB Reynolds, TOP Speidel, DW Vroom, and MA Welt. 1958. “A Study of the Nuclear and Physical Properties of the ORNL Graphite Reactor Shield.” Oak Ridge National Lab., Tenn.

Bykov, V. N., A. V. Denisov, V. B. Dubrovskii, V. V. Korenevskii, G. K. Krivokoneva, and L. P. Muzalevskii. 1981. “Effect of Irradiation Temperature on the Radiation Expansion of Quartz.” *Soviet Atomic Energy* 51 (3): 593–95.

Carlson, R. W., and T. J. Reading. 1988. “Model Study of Shrinkage Cracking in Concrete Building Walls.” *Structural Journal* 85 (4): 395–404. https://doi.org/10.14359/2666.

Challamel, Noël, Christophe Lanos, and Charles Casandjian. 2005. “Creep Damage Modelling for Quasi-Brittle Materials.” *European Journal of Mechanics - A/Solids* 24 (4): 593–613. https://doi.org/10.1016/j.euromechsol.2005.05.003.

Comite Euro-International Du Beton. 1993. *CEB-FIP MODEL CODE 1990: DESIGN CODE*. Thomas Telford Publishing. https://doi.org/10.1680/ceb-fipmc1990.35430.

“Compute Elasticity Tensor|MOOSE.” Accessed April 25, 2019. https://mooseframework.org/source/materials/ComputeElasticityTensor.html#.

Cristiani, G, S Granata, and A Montagnini. 1972. “Behaviour of Plastic Mortar Samples under Temperature and Radiation Conditions.” In , 41–53.

Dean, S. W., J. L. Schlitter, A. H. Senter, D. P. Bentz, T. Nantung, and W. J. Weiss. 2010. “A Dual Concentric Ring Test for Evaluating Residual Stress Development Due to Restrained Volume Change.” *Journal of ASTM International* 7 (9): 103118. https://doi.org/10.1520/JAI103118.

Dean, Sw, J-H Moon, F Rajabipour, B Pease, and J Weiss. 2006. “Quantifying the Influence of Specimen Geometry on the Results of the Restrained Ring Test.” *Journal of ASTM International* 3 (8): 100436. https://doi.org/10.1520/JAI100436.

RILEM FMC-50. “Determination of the Fracture Energy of Mortar and Concrete by Means of Three-Point Bend Tests on Notched Beams.” 1985. *Materials and Structures* 18 (4): 287–90. https://doi.org/10.1007/BF02472918.

Di Luzio, Giovanni. 2009. “Numerical Model for Time-Dependent Fracturing of Concrete.” *Journal of Engineering Mechanics* 135 (7): 632–40. https://doi.org/10.1061/(ASCE)0733-9399(2009)135:7(632).

Dong, Wei, Xiangming Zhou, Zhimin Wu, and Bohan Xu. 2017. “Investigating Crack Initiation and Propagation of Concrete in Restrained Shrinkage Circular/Elliptical Ring Test.” *Materials and Structures* 50 (1): 1–13. https://doi.org/10.1617/s11527-016-0942-1.

Du Plessis, J. Prieur, and Jacob H. Masliyah. 1988. “Mathematical Modelling of Flow through Consolidated Isotropic Porous Media.” *Transport in Porous Media* 3 (2): 145–61. https://doi.org/10.1007/BF00820342.

Dubrovskii, VB, Sh Sh Ibragimov, M Ya Kulakovskii, A Ya Ladygin, and BK Pergamenshchik. 1967. “Radiation Damage in Ordinary Concrete.” *Soviet Atomic Energy* 23 (4): 1053–58.

Dubrovskij, V. B., S. S. Ibragimov, A. Y. Ladygin, and B. K. Pergamenshchik. 1966. “The Effect of Neutron Irradiation on Certain Properties of Refractory Concretes.” *At.Energ.At.Energ.* 21: 108–12.

Elleuch, L. F., F. Dubois, and J. Rappeneau. 1972. “Effects of Neutron Radiation on Special Concretes and Their Components.” *Special Publication* 34 (January): 1071–1108. https://doi.org/10.14359/18107.

Fernandes, Fabio, Shilpa Manari, Mathew Aguayo, Kevin Santos, Tandre Oey, Zhenhua Wei, Gabriel Falzone, Narayanan Neithalath, and Gaurav Sant. 2014. “On the Feasibility of Using Phase Change Materials (PCMs) to Mitigate Thermal Cracking in Cementitious Materials.” *Cement and Concrete Composites* 51 (August): 14–26. https://doi.org/10.1016/j.cemconcomp.2014.03.003.

Fichant, Stéphanie, Christian La Borderie, and Gilles Pijaudier-Cabot. 1999. “Isotropic and Anisotropic Descriptions of Damage in Concrete Structures.” *Mechanics of Cohesive-Frictional Materials* 4 (4): 339–59. https://doi.org/10.1002/(SICI)1099-1484(199907)4:4<339::AID-CFM65>3.0.CO;2-J.

Field, K.G., I. Remec, and Y. Le Pape. 2015. “Radiation Effects in Concrete for Nuclear Power Plants – Part I: Quantification of Radiation Exposure and Radiation Effects.” *Nuclear Engineering and Design* 282 (February): 126–43. https://doi.org/10.1016/j.nucengdes.2014.10.003.

Gaston, D, G Hansen, S Kadioglu, D A Knoll, C Newman, H Park, C Permann, and W Taitano. 2009. “Parallel Multiphysics Algorithms and Software for Computational Nuclear Engineering.” *Journal of Physics: Conference Series* 180 (July): 012012. https://doi.org/10.1088/1742-6596/180/1/012012.

Gaston, Derek, Chris Newman, Glen Hansen, and Damien Lebrun-Grandié. 2009. “MOOSE: A Parallel Computational Framework for Coupled Systems of Nonlinear Equations.” *Nuclear Engineering and Design* 239 (10): 1768–78. https://doi.org/10.1016/j.nucengdes.2009.05.021.

Gaston, Derek R., Cody J. Permann, John W. Peterson, Andrew E. Slaughter, David Andrš, Yaqi Wang, Michael P. Short, et al. 2015. “Physics-Based Multiscale Coupling for Full Core Nuclear Reactor Simulation.” *Annals of Nuclear Energy*, Multi-Physics Modelling of LWR Static and Transient Behaviour, 84 (October): 45–54. https://doi.org/10.1016/j.anucene.2014.09.060.

Giorla, A., M. Vaitová, Y. Le Pape, and P. Štemberk. 2015. “Meso-Scale Modeling of Irradiated Concrete in Test Reactor.” *Nuclear Engineering and Design* 295 (December): 59–73. https://doi.org/10.1016/j.nucengdes.2015.08.027.

Giorla, Alain B. 2017. “Implementation of Concrete Creep Model in Grizzly, Technical Report No ORNL/TM-2017/729.” Technical Report ORNL/TM-2017/729.

Giorla Alain B., Le Pape Yann, and Dunant Cyrille F. 2017. “Computing Creep-Damage Interactions in Irradiated Concrete.” *Journal of Nanomechanics and Micromechanics* 7 (2): 04017001. https://doi.org/10.1061/(ASCE)NM.2153-5477.0000118.

Gopalaratnam, V. S., and Surendra P. Shah. 1985. “Softening Response of Plain Concrete in Direct Tension.” *Journal Proceedings* 82 (3): 310–23. https://doi.org/10.14359/10338.

Grasley, Zachary C., and Matthew D. D’Ambrosia. 2011. “Viscoelastic Properties and Drying Stress Extracted from Concrete Ring Tests.” *Cement and Concrete Composites* 33 (2): 171–78. https://doi.org/10.1016/j.cemconcomp.2010.10.014.

Grasley, Zachary C., and David A. Lange. 2007. “Thermal Dilation and Internal Relative Humidity of Hardened Cement Paste.” *Materials and Structures* 40 (3): 311–17. https://doi.org/10.1617/s11527-006-9108-x.

Gray, BS. 1972. “The Effect of Reactor Radiation on Cements and Concrete.” *Comm. of the European Communities, Luxembourg*, 17–39.

Guinea, G. V., J. Planas, and M. Elices. 1992. “Measurement of the Fracture Energy Using Three-Point Bend Tests: Part 1—Influence of Experimental Procedures.” *Materials and Structures* 25 (4): 212–18. https://doi.org/10.1007/BF02473065.

Hansen, Will. 1987. “Drying Shrinkage Mechanisms in Portland Cement Paste.” *Journal of the American Ceramic Society* 70 (5): 323–28. https://doi.org/10.1111/j.1151-2916.1987.tb05002.x.

Henkensiefken, Ryan, Dale Bentz, Tommy Nantung, and Jason Weiss. 2009. “Volume Change and Cracking in Internally Cured Mixtures Made with Saturated Lightweight Aggregate under Sealed and Unsealed Conditions.” *Cement and Concrete Composites* 31 (7): 427–37. https://doi.org/10.1016/j.cemconcomp.2009.04.003.

Hillerborg, A., M. Modéer, and P.-E. Petersson. 1976. “Analysis of Crack Formation and Crack Growth in Concrete by Means of Fracture Mechanics and Finite Elements.” *Cement and Concrete Research* 6 (6): 773–81. https://doi.org/10.1016/0008-8846(76)90007-7.

Hilsdorf, H. K., J. Kropp, and H. J. Koch. 1978. “The Effects of Nuclear Radiation on the Mechanical Properties of Concrete.” *Special Publication* 55 (August): 223–54. https://doi.org/10.14359/6616.

Holt, E., and M. Leivo. 2004. “Cracking Risks Associated with Early Age Shrinkage.” *Cement and Concrete Composites* 26 (5): 521–30. https://doi.org/10.1016/S0958-9465(03)00068-4.

Hooton, Rd, S Lepage, M Baalbaki, É Dallaire, and Pc Aïtcin. 1999. “Early Shrinkage Development in a High Performance Concrete.” *Cement, Concrete and Aggregates* 21 (1): 31–35. https://doi.org/10.1520/CCA10505J.

Hoover, Christian G., and Zdeněk P. Bažant. 2014. “Cohesive Crack, Size Effect, Crack Band and Work-of-Fracture Models Compared to Comprehensive Concrete Fracture Tests.” *International Journal of Fracture* 187 (1): 133–43. https://doi.org/10.1007/s10704-013-9926-0.

Hordijk, D. A., and H. W. Reinhardt. 1990. “Fracture of Concrete in Uniaxial Tensile Experiments as Influenced by Curing Conditions.” *Engineering Fracture Mechanics* 35 (4): 819–26. https://doi.org/10.1016/0013-7944(90)90166-E.

Hossain, Akhter B., and Jason Weiss. 2004. “Assessing Residual Stress Development and Stress Relaxation in Restrained Concrete Ring Specimens.” *Cement and Concrete Composites* 26 (5): 531–40. https://doi.org/10.1016/S0958-9465(03)00069-6.

Hossain, Akhter B., and Jason Weiss. 2006. “The Role of Specimen Geometry and Boundary Conditions on Stress Development and Cracking in the Restrained Ring Test.” *Cement and Concrete Research* 36 (1): 189–99. https://doi.org/10.1016/j.cemconres.2004.06.043.

Https://Github.Com/Idaholab/Moose. (2014) 2019. C++. Idaho National Laboratory. https://github.com/idaholab/moose.

Huang, Hai, and Benjamin Spencer. 2016. “Grizzly Model of Fully Coupled Heat Transfer, Moisture Diffusion, Alkali-Silica Reaction and Fracturing Processes in Concrete.” In *Proceedings of the 9th International Conference on Fracture Mechanics of Concrete and Concrete Structures*. Berkeley, CA: IA-FraMCoS. https://doi.org/10.21012/FC9.194.

Hummel, A. 1959. “Vom Einfluss Der Cementart, Des Wasserzementverhaltnisses Und Des Belastungalters Auf Das Kriechen Des Betons.” *Zement-Kalk-Gips* 12 (5): 181–87.

“Impact of Gamma-Ray Irradiation on Hardened White Portland Cement Pastes Exposed to Atmosphere | Elsevier Enhanced Reader.” Accessed March 13, 2020. https://doi.org/10.1016/j.cemconres.2018.03.005.

Ingham, Derek B., and I. Pop. 1998. *Transport Phenomena in Porous Media*. Elsevier.

"MOOSE Computer Simulation Framework - Idaho National Laboratory Research Fact Sheet." Accessed March 29, 2018. http://www4vip.inl.gov/research/moose-applications/.

Kelly, B., J. Brocklehurst, D. Mottershead, and S. McNearney. 1969. "The Effects of Reactor Radiation on Concrete." *Proceedings of the Second Information Meeting on Pre Stress Concrete and Reactor Pressure Vessels and Their Thermal Isolation*, 237–65.

Khaled, Bilal, Loukham Shyamsunder, Canio Hoffarth, Subramaniam D Rajan, Robert K Goldberg, Kelly S Carney, Paul DuBois, and Gunther Blankenhorn. 2019. "Damage Characterization of Composites to Support an Orthotropic Plasticity Material Model." *Journal of Composite Materials* 53 (7): 941–67. https://doi.org/10.1177/0021998318793506.

Khudhair, Amar M., and Mohammed M. Farid. 2004. "A Review on Energy Conservation in Building Applications with Thermal Storage by Latent Heat Using Phase Change Materials." *Energy Conversion and Management* 45 (2): 263–75. https://doi.org/10.1016/S0196-8904(03)00131-6.

Kirk, Benjamin S., John W. Peterson, Roy H. Stogner, and Graham F. Carey. 2006. "LibMesh : A C++ Library for Parallel Adaptive Mesh Refinement/Coarsening Simulations." *Engineering with Computers* 22 (3–4): 237–54. https://doi.org/10.1007/s00366-006-0049-3.

Knoll, D.A., and D.E. Keyes. 2004. "Jacobian-Free Newton–Krylov Methods: A Survey of Approaches and Applications." *Journal of Computational Physics* 193 (2): 357–97. https://doi.org/10.1016/j.jcp.2003.08.010.

Kodur, V. K. R., T. C. Wang, and F. P. Cheng. 2004. "Predicting the Fire Resistance Behaviour of High Strength Concrete Columns." *Cement and Concrete Composites*, Fire Resistance, 26 (2): 141–53. https://doi.org/10.1016/S0958-9465(03)00089-1.

Künzel, Hartwig M. 1995. *Simultaneous Heat and Moisture Transport in Building Components: One- and Two-Dimensional Calculation Using Simple Parameters*. Stuttgart: IRB Verlag.

Kurumatani, Mao, Kenjiro Terada, Junji Kato, Takashi Kyoya, and Kazuo Kashiyama. 2016. "An Isotropic Damage Model Based on Fracture Mechanics for Concrete." *Engineering Fracture Mechanics* 155 (April): 49–66. https://doi.org/10.1016/j.engfracmech.2016.01.020.

Le Bellégo, Caroline, Jean-François Dubé, Gilles Pijaudier-Cabot, and Bruno Gérard. 2003. “Calibration of Nonlocal Damage Model from Size Effect Tests.” *European Journal of Mechanics - A/Solids* 22 (1): 33–46. https://doi.org/10.1016/S0997-7538(02)01255-X.

Le, Jia Liang, Zdeněk P. Bažant, and Martin Z. Bažant. 2011. “Unified Nano-Mechanics Based Probabilistic Theory of Quasibrittle and Brittle Structures: I. Strength, Static Crack Growth, Lifetime and Scaling.” *Journal of the Mechanics and Physics of Solids* 59 (7): 1291–1321. https://doi.org/10.1016/j.jmps.2011.03.002.

Le Pape, Y., K. G. Field, and I. Remec. 2015. “Radiation Effects in Concrete for Nuclear Power Plants, Part II: Perspective from Micromechanical Modeling.” *Nuclear Engineering and Design* 282 (February): 144–57. https://doi.org/10.1016/j.nucengdes.2014.10.014.

Li, Victor C., and Mohamed Maalej. 1996. “Toughening in Cement Based Composites. Part I: Cement, Mortar, and Concrete.” *Cement and Concrete Composites*, Toughness of FRC Composites, 18 (4): 223–37. https://doi.org/10.1016/0958-9465(95)00028-3.

Lubachevsky, Boris D., and Frank H. Stillinger. 1990. “Geometric Properties of Random Disk Packings.” *Journal of Statistical Physics* 60 (5–6): 561–83.

Luikov, A. V. 1975. “Systems of Differential Equations of Heat and Mass Transfer in Capillary-Porous Bodies (Review).” *International Journal of Heat and Mass Transfer* 18 (1): 1–14. https://doi.org/10.1016/0017-9310(75)90002-2.

MacNamara, Shev, and Gilbert Strang. 2016. “Operator Splitting.” In *Splitting Methods in Communication, Imaging, Science, and Engineering*, edited by Roland Glowinski, Stanley J. Osher, and Wotao Yin, 95–114. Cham: Springer International Publishing. https://doi.org/10.1007/978-3-319-41589-5_3.

Maruyama, Ippei, and Go Igarashi. 2015. “Numerical Approach towards Aging Management of Concrete Structures: Material Strength Evaluation in a Massive Concrete Structure under One-Sided Heating.” *Journal of Advanced Concrete Technology* 13 (11): 500–527. https://doi.org/10.3151/jact.13.500.

Maruyama, Ippei, Osamu Kontani, Masayuki Takizawa, Shohei Sawada, Shunsuke Ishikawao, Junichi Yasukouchi, Osamu Sato, Junji Etoh, and Takafumi Igari. 2017. “Development of Soundness Assessment Procedure for Concrete Members Affected by Neutron and Gamma-Ray Irradiation.” *Journal of Advanced Concrete Technology* 15 (9): 440–523. https://doi.org/10.3151/jact.15.440.

Maruyama, Ippei, Hiroshi Sasano, Yukiko Nishioka, and Go Igarashi. 2014. “Strength and Young’s Modulus Change in Concrete Due to Long-Term Drying and Heating up

to 90°C." *Cement and Concrete Research* 66 (December): 48–63. https://doi.org/10.1016/j.cemconres.2014.07.016.

Mazars, Jacky. 1986. "A Description of Micro- and Macroscale Damage of Concrete Structures." *Engineering Fracture Mechanics* 25 (5): 729–37. https://doi.org/10.1016/0013-7944(86)90036-6.

Mazars, Jacky, François Hamon, and Stéphane Grange. 2015. "A New 3D Damage Model for Concrete under Monotonic, Cyclic and Dynamic Loadings." *Materials and Structures* 48 (11): 3779–93. https://doi.org/10.1617/s11527-014-0439-8.

Mazzotti, C, and M Savoia. 2001. "An Isotropic Damage Model for Non Linear Creep Behavior of Concrete in Compression." *4th Int. Conf. on Fracture Mechanics of Concrete and Concrete Structures, Cachan, France,* 8.

Mazzotti, Claudio, and Marco Savoia. 2003. "Nonlinear Creep Damage Model for Concrete under Uniaxial Compression." *Journal of Engineering Mechanics* 129 (9): 1065–75. https://doi.org/10.1061/(ASCE)0733-9399(2003)129:9(1065).

McDowall, D. C. 1972. "The Effect of Gamma Irradiation on the Creep Properties of Concrete." http://inis.iaea.org/Search/search.aspx?orig_q=RN:4042786.

Mensi, R., P. Acker, and A. Attolou. 1988. "Séchage du béton: analyse et modélisation." *Materials and Structures* 21 (1): 3–12. https://doi.org/10.1007/BF02472523.

Moon, Jae Heum, and Jason Weiss. 2006. "Estimating Residual Stress in the Restrained Ring Test under Circumferential Drying." *Cement and Concrete Composites* 28 (5): 486–96. https://doi.org/10.1016/j.cemconcomp.2005.10.008.

Nakano, Shinsuke, Shunsuke Muto, and Tetsuo Tanabe. 2006. "Change in Mechanical Properties of Ion-Irradiated Ceramics Studied by Nanoindentation." *MATERIALS TRANSACTIONS* 47 (1): 112–21. https://doi.org/10.2320/matertrans.47.112.

Neithalath, N, B Pease, and E Attiogbe. 2005. "Considering Moisture Gradients and Time-Dependent Crack Growth in Restrained Concrete Elements Subjected to Drying." *Proceedings of the Indo-US Workshop on High Performance Cement Based Concrete Composites, American Ceramic Society, Chennai, India*, January, 11.

"NRC: Backgrounder on Reactor License Renewal." Accessed March 19, 2020. https://www.nrc.gov/reading-rm/doc-collections/fact-sheets/fs-reactor-license-renewal.html#status.

Oliveira, Mateus A., Miguel Azenha, and Paulo B. Lourenço. 2015. "Simulation of Humidity Fields in Concrete: Experimental Validation and Parameter Estimation."

Journal of Advanced Concrete Technology 13 (4): 214–29. https://doi.org/10.3151/jact.13.214.

Omar, Mirvat, Ahmed Loukili, Gilles Pijaudier-Cabot, and Yann LE PAPE. 2009. "Creep Damage Coupled Effects: Experimental Investigation on Bending Beams with Various Sizes." *Journal of Materials in Civil Engineering* 21 (2): 65–72. https://doi.org/10.1061/(ASCE)0899-1561(2009)21:2(65).

"Parallel Multiphysics Finite Element Framework." Accessed April 24, 2019. https://mooseframework.org/.

Passuello, Alexandra, Giacomo Moriconi, and Surendra P. Shah. 2009. "Cracking Behavior of Concrete with Shrinkage Reducing Admixtures and PVA Fibers." *Cement and Concrete Composites* 31 (10): 699–704. https://doi.org/10.1016/j.cemconcomp.2009.08.004.

Permann, Cody J., Derek R. Gaston, David Andrs, Robert W. Carlsen, Fande Kong, Alexander D. Lindsay, Jason M. Miller, et al. 2019. "MOOSE: Enabling Massively Parallel Multiphysics Simulation." *ArXiv:1911.04488 [Physics]*, November. http://arxiv.org/abs/1911.04488.

Pijaudier-Cabot, Gilles, and Zdeněk P. Bažant. 1987. "Nonlocal Damage Theory." *Journal of Engineering Mechanics* 113 (10): 1512–33. https://doi.org/10.1061/(ASCE)0733-9399(1987)113:10(1512).

Pijaudier-Cabot, Gilles, Zdeněk P. Bažant, and Mazen Tabbara. 1988. "Comparison of Various Models for Strain- Softening." *Engng Comput.* 5: 141–50.

Pijaudier-Cabot, Gilles, and Jacky Mazars. 2001. "Damage Models for Concrete." In *Handbook of Materials Behavior Models*, edited by Jean Lemaitre, 2:500–512. Failures of Materials. Elsevier. https://doi.org/10.1016/B978-012443341-0/50056-9.

Pijaudier-Cabot, Gilles, Mirvat Omar, Ahmed Loukili, and Yann LE Pape. 2005. "Creep - Damage Interaction in Concrete Structures." In *11th International Conference on Fracture*, 6.

Ping, Zhou Fan. 1992. "Time-Dependent Crack Growth and Fracture in Concrete." http://inis.iaea.org/Search/search.aspx?orig_q=RN:24000668.

Planas, J., M. Elices, and G. V. Guinea. 1992. "Measurement of the Fracture Energy Using Three-Point Bend Tests: Part 2—Influence of Bulk Energy Dissipation." *Materials and Structures* 25 (5): 305–12. https://doi.org/10.1007/BF02472671.

Pomaro, Beatrice. 2016. “A Review on Radiation Damage in Concrete for Nuclear Facilities: From Experiments to Modeling.” Research article. Modelling and Simulation in Engineering. 2016. https://doi.org/10.1155/2016/4165746.

Powers, T. C., and T. L. Brownyard. 1946. “Studies of the Physical Properties of Hardened Portland Cement Paste.” *Journal Proceedings* 43 (9): 249–336. https://doi.org/10.14359/15301.

Raoufi, Kambiz, John Schlitter, Dale Bentz, and Jason Weiss. 2011. “Parametric Assessment of Stress Development and Cracking in Internally Cured Restrained Mortars Experiencing Autogenous Deformations and Thermal Loading.” Research article. Advances in Civil Engineering. 2011. https://doi.org/10.1155/2011/870128.

Raphael, Jerome M. 1984. “Tensile Strength of Concrete.” *Journal Proceedings* 81 (2): 158–65. https://doi.org/10.14359/10653.

“Researches Toward a General Flexural Theory for Structural Concrete.” 1960. *ACI Journal Proceedings* 57 (7). https://doi.org/10.14359/8009.

Rosa, A. L., R. C. Yu, G. Ruiz, L. Saucedo, and J. L. A. O. Sousa. 2012. “A Loading Rate Dependent Cohesive Model for Concrete Fracture.” *Engineering Fracture Mechanics* 82 (March): 195–208. https://doi.org/10.1016/j.engfracmech.2011.12.013.

Ruiz, G., X. X. Zhang, R. C. Yu, R. Porras, E. Poveda, and J. R. del Viso. 2011. “Effect of Loading Rate on Fracture Energy of High-Strength Concrete.” *Strain* 47 (6): 518–24. https://doi.org/10.1111/j.1475-1305.2010.00719.x.

Salomoni, V. A., C. E. Majorana, B. Pomaro, G. Xotta, and F. Gramegna. 2014. “Macroscale and Mesoscale Analysis of Concrete as a Multiphase Material for Biological Shields against Nuclear Radiation.” *International Journal for Numerical and Analytical Methods in Geomechanics* 38 (5): 518–35. https://doi.org/10.1002/nag.2222.

Schlitter, J L, D P Bentz, and W J Weiss. 2013. “Quantifying Stress Development and Remaining Stress Capacity in Restrained, Internally Cured Mortars.” *ACI Materials Journal* 110 (1): 3–12.

See, Heather T., Emmanuel K. Attiogbe, and Matthew A. Miltenberger. 2003. “Shrinkage Cracking Characteristics of Concrete Using Ring Specimens.” *Materials Journal* 100 (3): 239–45. https://doi.org/10.14359/12625.

Slaughter, Andrew E., John W. Peterson, Derek R. Gaston, Cody J. Permann, David Andrš, and Jason M. Miller. 2015. “Continuous Integration for Concurrent MOOSE

Framework and Application Development on GitHub." *Journal of Open Research Software* 3 (1): e14. https://doi.org/10.5334/jors.bx.

Šmilauer, Vít, Petr Havlásek, Tobias Gasch, Arnaud Delaplace, David E. -M. Bouhjiti, Farid Benboudjema, Matthieu Briffaut, Fragkoulis Kanavaris, and Miguel Azenha. 2019. "Hygro-Mechanical Modeling of Restrained Ring Test: COST TU1404 Benchmark." *Construction and Building Materials* 229 (December): 116543. https://doi.org/10.1016/j.conbuildmat.2019.07.269.

Stefan, Radek. 2015. "Transport Processes in Concrete at High Temperatures. Mathematical Modelling and Engineering Applications with Focus on Concrete Spalling." https://doi.org/10.13140/RG.2.1.2956.9123.

Strack, O.E., R.B. Leavy, and R.M. Brannon. 2015. "Aleatory Uncertainty and Scale Effects in Computational Damage Models for Failure and Fragmentation." *International Journal for Numerical Methods in Engineering* 102 (3–4): 468–95. https://doi.org/10.1002/nme.4699.

Tamtsia, Basile T., James J. Beaudoin, and Jacques Marchand. 2004. "The Early Age Short-Term Creep of Hardening Cement Paste: Load-Induced Hydration Effects." *Cement and Concrete Composites*, Early Age Concrete - Properties and Performance, 26 (5): 481–89. https://doi.org/10.1016/S0958-9465(03)00079-9.

Thiele, Alexander M., Zhenhua Wei, Gabriel Falzone, Benjamin A. Young, Narayanan Neithalath, Gaurav Sant, and Laurent Pilon. 2016. "Figure of Merit for the Thermal Performance of Cementitious Composites Containing Phase Change Materials." *Cement and Concrete Composites* 65 (January): 214–26. https://doi.org/10.1016/j.cemconcomp.2015.10.023.

Vree, J. H. P. de, W. A. M. Brekelmans, and M. A. J. van Gils. 1995. "Comparison of Nonlocal Approaches in Continuum Damage Mechanics." *Computers & Structures* 55 (4): 581–88. https://doi.org/10.1016/0045-7949(94)00501-S.

Wang, Yao, and Yunping Xi. 2017. "The Effect of Temperature on Moisture Transport in Concrete." *Materials* 10 (8): 926. https://doi.org/10.3390/ma10080926.

Weerheijm, J., and J.C.A.M. Van Doormaal. 2007. "Tensile Failure of Concrete at High Loading Rates: New Test Data on Strength and Fracture Energy from Instrumented Spalling Tests." *International Journal of Impact Engineering* 34 (3): 609–26. https://doi.org/10.1016/j.ijimpeng.2006.01.005.

Wei, Zhenhua, Gabriel Falzone, Sumanta Das, Naman Saklani, Yann Le Pape, Laurent Pilon, Narayanan Neithalath, and Gaurav Sant. 2017a. "Restrained Shrinkage Cracking of Cementitious Composites Containing Soft PCM Inclusions: A Paste

(Matrix) Controlled Response." *Materials & Design* 132 (October): 367–74. https://doi.org/10.1016/j.matdes.2017.06.066.

Wei, Zhenhua, Gabriel Falzone, Bu Wang, Alexander Thiele, Guillermo Puerta-Falla, Laurent Pilon, Narayanan Neithalath, and Gaurav Sant. 2017. "The Durability of Cementitious Composites Containing Microencapsulated Phase Change Materials." *Cement and Concrete Composites* 81 (August): 66–76. https://doi.org/10.1016/j.cemconcomp.2017.04.010.

Weiss, W. J., and S. P. Shah. 2002. "Restrained Shrinkage Cracking: The Role of Shrinkage Reducing Admixtures and Specimen Geometry." *Materials and Structures* 35 (2): 85–91. https://doi.org/10.1007/BF02482106.

Weiss, W. Jason, Wei Yang, and Surendra P. Shah. 1998. "Shrinkage Cracking of Restrained Concrete Slabs." *Journal of Engineering Mechanics* 124 (7): 765–74. https://doi.org/10.1061/(ASCE)0733-9399(1998)124:7(765).

Weiss, W. Jason, Wei Yang, and Surendra P. Shah. 2000. "Influence of Specimen Size/Geometry on Shrinkage Cracking of Rings." *Journal of Engineering Mechanics* 126 (1): 93–101. https://doi.org/10.1061/(ASCE)0733-9399(2000)126:1(93).

www.energy.gov. "What's the Lifespan for a Nuclear Reactor? Much Longer Than You Might Think." Energy.Gov. Accessed March 24, 2020. https://www.energy.gov/ne/articles/whats-lifespan-nuclear-reactor-much-longer-you-might-think.

"Www.Mooseframework.Org: ComputeStressBase Class Reference." Accessed April 30, 2019. https://mooseframework.inl.gov/docs/doxygen/modules/classComputeStressBase.html.

"Www.Mooseframework.Org: StressDivergenceTensors Class Reference." Accessed April 25, 2019. https://mooseframework.inl.gov/docs/doxygen/modules/classStressDivergenceTensors.html#details.

Xi, Yunping, Zdeněk P. Bažant, and Hamlin M. Jennings. 1994. "Moisture Diffusion in Cementitious Materials Adsorption Isotherms." *Advanced Cement Based Materials* 1 (6): 248–57. https://doi.org/10.1016/1065-7355(94)90033-7.

Xi, Yunping, Zdenňek P. Bažant, Larissa Molina, and Hamlin M. Jennings. 1994. "Moisture Diffusion in Cementitious Materials Moisture Capacity and Diffusivity." *Advanced Cement Based Materials* 1 (6): 258–66. https://doi.org/10.1016/1065-7355(94)90034-5.

Zhang, P, P Klein, Y Huang, H Gao, and P D Wu. 2002. “Numerical Simulation of Cohesive Fracture by the Virtual-Internal-Bond Model,” 16.

Zhou, Xiangming, Wei Dong, and Olayinka Oladiran. 2014. “Experimental and Numerical Assessment of Restrained Shrinkage Cracking of Concrete Using Elliptical Ring Specimens.” *Journal of Materials in Civil Engineering* 26 (11): 04014087. https://doi.org/10.1061/(ASCE)MT.1943-5533.0001001.

Zi, Goangseup, and Zdeněk P. Bažant. 2002. “Continuous Relaxation Spectrum for Concrete Creep and Its Incorporation into Microplane Model M4.” *Journal of Engineering Mechanics* 128 (12): 1331–36. https://doi.org/10.1061/(ASCE)0733-9399(2002)128:12(1331).

APPENDIX A

HEADER FILE FOR ISOTROPIC DAMAGE MODEL

```
#ifndef ISOTROPICDAMAGE_H
#define ISOTROPICDAMAGE_H

#include "ColumnMajorMatrix.h"
#include "ScalarDamageBase.h"
#include "SmearedCrackSofteningBase.h"
#include "Function.h"
#include "GuaranteeConsumer.h"

class IsotropicDamage;

template <>
InputParameters validParams<IsotropicDamage>();

/**
 * IsotropicDamage computes the stress for a finite strain
 * material with smeared cracking
 */
class IsotropicDamage : public ScalarDamageBase, public GuaranteeConsumer
{
public:
  IsotropicDamage(const InputParameters & parameters);

  virtual void initialSetup() override;
  virtual void initQpStatefulProperties() override;

protected:

  virtual void updateQpDamageIndex() override;
  void computeDamageEvolution(Real max_principal_strain, Real cracking_strain, Real cracking_stress,
Real youngs_modulus);


  /// Enum defining the crack release model
  const enum class CrackingRelease { exponential, linear, brittle } _cracking_release;

  /// Enum defining the failure criterion
  const enum class FailureCriterion { stressbased, strainbased } _failure_criterion;

  /// Threshold at which cracking initiates if tensile stress exceeds it
  const VariableValue & _tensile_strength;

  /// Ratio of the residual stress after being fully cracked to the tensile
  /// cracking threshold stress
  const Real _residual_frac;

  /// Fracture energy
  const Real _Gf;

  // Fraction of creep strain causing damage
  const Real _creep_damage_param;

  //@{ Strain upon crack initiation
  MaterialProperty<Real> & _crack_initiation_strain;
  const MaterialProperty<Real> & _crack_initiation_strain_old;
```

```
  ///@}

  //@{ Flag variable to indicate if cracking has occured or not
  MaterialProperty<Real> & _crack_flag;
  const MaterialProperty<Real> & _crack_flag_old;
  ///@}

  //@{ Cracking surface
  MaterialProperty<Real> & _cracking_yield_surface;
  const MaterialProperty<Real> & _cracking_yield_surface_old;
  ///@}

  //@{ Actual cracking stress during initiation
  MaterialProperty<Real> & _actual_cracking_stress;
  const MaterialProperty<Real> & _actual_cracking_stress_old;
  ///@}

  //@{ Equivalent Strain
  MaterialProperty<Real> & _equivalent_strain;
  const MaterialProperty<Real> & _equivalent_strain_old;
  ///@}

  /// Enum defining the equivalent strain definition
  const enum class EquivalentStrainDefinition { mazar, modifiedvonmises, modifiedmazar }
_equivalent_strain_definition;

  /// Name of elasticity tensor
  const std::string _elasticity_tensor_name;

  /// Current undamaged elasticity tensor
  const MaterialProperty<RankFourTensor> & _elasticity_tensor;

  /// Current stress
  const MaterialProperty<RankTwoTensor> & _stress;

  /// Current elastic strain
  const MaterialProperty<RankTwoTensor> & _elastic_strain;

  /// Current creep strain
  const MaterialProperty<RankTwoTensor> & _mechanical_strain;

};

#endif // ISOTROPICDAMAGE_H
```

APPENDIX B

SOURCE CODE FOR ISOTROPIC DAMAGE MODEL

```
#include "IsotropicDamage.h"
#include "MooseMesh.h"
#include "ElasticityTensorTools.h"
#include "StressUpdateBase.h"
#include "Conversion.h"
#include "RankTwoTensor.h"
#include "RankFourTensor.h"
#include "MooseUtils.h"

#include "libmesh/utility.h"

registerMooseObject("TensorMechanicsApp", IsotropicDamage);

template <>
InputParameters
validParams<IsotropicDamage>()
{
  InputParameters params = validParams<ScalarDamageBase>();
  params.addClassDescription("Compute stress using an isotropic damage model");
  MooseEnum cracking_release("exponential linear brittle", "linear");
  params.addParam<MooseEnum>("cracking_release",
                                      cracking_release,
                                     "The cracking release type.  'linear' (default) gives an linear stress release "
                     "'exponential' uses an exponential softening model ");
  MooseEnum failure_criterion("stressbased strainbased", "stressbased");
  params.addParam<MooseEnum>("failure_criterion",
                                      failure_criterion,
                                     "failure criterion.  'stressbased' (default) gives a stress based failure "
                     "'strainbased' uses a strain based failure ");
  params.addRequiredCoupledVar("tensile_strength",
                                       "The stress threshold beyond which cracking occurs. Negative values
prevent cracking.");
  params.addParam<Real>("residual_fraction",
                                    0.0,
                                    "The fraction of the cracking stress allowed to be maintained following a
crack.");
  params.addParam<Real>("fracture_energy",
                                    "The fracture energy of the material");
  params.addParam<Real>("creep_damage_parameter",
                        0.0,
                                    "Fraction of creep strain causing damage");
  MooseEnum equivalent_strain_definition("mazar modifiedvonmises modifiedmazar",
"modifiedvonmises");
  params.addParam<MooseEnum>("equivalent_strain_definition",
                                      equivalent_strain_definition,
                                     "How damage evolves with strain.  'modifiedvonmises' (default) calculate
strain as modified version of Vonmises"
                     "'mazar' calculates strain as per Mazar model, ");
  return params;
}

IsotropicDamage::IsotropicDamage(const InputParameters & parameters)
  : ScalarDamageBase(parameters),
    GuaranteeConsumer(this),
    _cracking_release(getParam<MooseEnum>("cracking_release").getEnum<CrackingRelease>()),
```

```
    _failure_criterion(getParam<MooseEnum>("failure_criterion").getEnum<FailureCriterion>()),
    _tensile_strength(coupledValue("tensile_strength")),
    _residual_frac(getParam<Real>("residual_fraction")),
    _Gf(getParam<Real>("fracture_energy")),
    _creep_damage_param(getParam<Real>("creep_damage_parameter")),
    _crack_initiation_strain(declareProperty<Real>(_base_name + "crack_initiation_strain")),
    _crack_initiation_strain_old(getMaterialPropertyOld<Real>(_base_name + "crack_initiation_strain")),
    _crack_flag(declareProperty<Real>(_base_name+"crack_flag")),
    _crack_flag_old(getMaterialPropertyOld<Real>(_base_name+"crack_flag")),
    _cracking_yield_surface(declareProperty<Real>(_base_name + "crack_yield_surface")),
    _cracking_yield_surface_old(getMaterialPropertyOld<Real>(_base_name + "crack_yield_surface")),
    _actual_cracking_stress(declareProperty<Real>("actual_cracking_stress")),
    _actual_cracking_stress_old(getMaterialPropertyOld<Real>(_base_name + "actual_cracking_stress")),
    _equivalent_strain(declareProperty<Real>(_base_name +"equivalent_strain")),
    _equivalent_strain_old(getMaterialPropertyOld<Real>(_base_name + "equivalent_strain")),

_equivalent_strain_definition(getParam<MooseEnum>("equivalent_strain_definition").getEnum<Equivale
ntStrainDefinition>()),
    _elasticity_tensor_name(_base_name + "elasticity_tensor"),
    _elasticity_tensor(getMaterialPropertyByName<RankFourTensor>(_elasticity_tensor_name)),
    _stress(getMaterialProperty<RankTwoTensor>(_base_name + "stress")),
    _elastic_strain(getMaterialProperty<RankTwoTensor>(_base_name + "elastic_strain")),
    _mechanical_strain(getMaterialProperty<RankTwoTensor>(_base_name + "mechanical_strain"))
{
}

void
IsotropicDamage::initQpStatefulProperties()
{
  ScalarDamageBase::initQpStatefulProperties();
  _crack_initiation_strain[_qp]=0.0;
  _crack_flag[_qp]=0.0;
  _cracking_yield_surface[_qp] =_tensile_strength[_qp];
  _actual_cracking_stress[_qp]=_tensile_strength[_qp];
  _equivalent_strain[_qp]=0.0;
}

void
IsotropicDamage::initialSetup()
{
  if (!hasGuaranteedMaterialProperty(_elasticity_tensor_name, Guarantee::ISOTROPIC))
    mooseError("IsotropicDamage requires that the elasticity tensor be "
               "guaranteed isotropic");
}

void
IsotropicDamage::updateQpDamageIndex()
{
  const Real youngs_modulus =
ElasticityTensorTools::getIsotropicYoungsModulus(_elasticity_tensor[_qp]);
  const Real poissons_ratio = ElasticityTensorTools::getIsotropicPoissonsRatio(_elasticity_tensor[_qp]);
      std::vector<Real> eigval(3, 0.0);
            _crack_flag[_qp]=_crack_flag_old[_qp];
            _crack_initiation_strain[_qp]=_crack_initiation_strain_old[_qp];
            _actual_cracking_stress[_qp]=_actual_cracking_stress_old[_qp];
```

```
   _stress[_qp].symmetricEigenvalues(eigval);
   Real max_principal_stress=std::max(std::max(eigval[0],eigval[1]),eigval[2]);
   _mechanical_strain[_qp].symmetricEigenvalues(eigval);
   Real max_principal_strain=std::max(std::max(eigval[0],eigval[1]),eigval[2]);
   // Find equivalent strain
   RankTwoTensor _effective_strain = _elastic_strain[_qp] + _creep_damage_param *
(_mechanical_strain[_qp]-_elastic_strain[_qp]);
   _effective_strain.symmetricEigenvalues(eigval);
   max_principal_strain=std::max(std::max(eigval[0],eigval[1]),eigval[2]);

  switch (_equivalent_strain_definition)
  {
          case EquivalentStrainDefinition::modifiedvonmises:
          {
          Real k=10;
          Real eps_xx=_effective_strain(0,0);
          Real eps_yy=_effective_strain(1,1);
          Real eps_zz=_effective_strain(2,2);
          Real eps_xy=_effective_strain(0,1);
          Real eps_xz=_effective_strain(0,2);
          Real eps_yz=_effective_strain(1,2);
          Real I1=eps_xx+eps_yy+eps_zz;
          Real J2=(eps_xx*eps_xx+eps_yy*eps_yy+eps_zz*eps_zz-eps_xx*eps_yy-eps_xx*eps_zz-
eps_yy*eps_zz+3*(eps_xy*eps_xy+eps_xz*eps_xz+eps_yz*eps_yz))/3;
      _equivalent_strain[_qp] = (k-1)/(2*k*(1-2*poissons_ratio))*I1+1/(2*k)*std::sqrt(std::pow(((k-
1)*I1/(1-2*poissons_ratio)),2)+12*k*J2/(std::pow((1+poissons_ratio),2)));
      break;
          }
          case EquivalentStrainDefinition::modifiedmazar:
          {
          Real eps_x1=eigval[0];
      Real eps_x2=eigval[1];
      Real eps_x3=eigval[2];
          Real I1=eps_x1+eps_x2+eps_x3;
          Real J2=0.5*(std::pow((eps_x1-eps_x2),2)+std::pow((eps_x2-eps_x3),2)+std::pow((eps_x3-
eps_x1),2));
      _equivalent_strain[_qp] = I1/2/(1-2*poissons_ratio)+std::sqrt(J2)/2/(1+poissons_ratio);
      break;
          }
          case EquivalentStrainDefinition::mazar:
          {
          Real eps_x1=std::max(eigval[0],0.0)*std::max(eigval[0],0.0);
      Real eps_x2=std::max(eigval[1],0.0)*std::max(eigval[1],0.0);
      Real eps_x3=std::max(eigval[2],0.0)*std::max(eigval[2],0.0);
          _equivalent_strain[_qp] = std::sqrt(eps_x1+eps_x2+eps_x3);
      break;
          }
  }
     Real initial_crack=0;

      //Checking if material is cracked or not
      if ( _crack_flag_old[_qp] == 0.0)
      {
                  switch (_failure_criterion)
```

```
                {
                        case FailureCriterion::stressbased:
                        {
                    if (max_principal_stress >= _cracking_yield_surface_old[_qp])
                        initial_crack=1;
                        break;
                        }
                        case FailureCriterion::strainbased:
                        {
                    if (_equivalent_strain[_qp] >= _cracking_yield_surface_old[_qp]/youngs_modulus)
                        initial_crack=1;
                        break;
                        }
                }

      // When the material cracks the first time
         if (initial_crack==1)
         {
           _crack_initiation_strain[_qp] =_equivalent_strain[_qp];
           _stress[_qp].symmetricEigenvalues(eigval);
           _actual_cracking_stress[_qp] =std::max(std::max(eigval[0],eigval[1]),eigval[2]);

           computeDamageEvolution(_equivalent_strain[_qp],_crack_initiation_strain[_qp],_actual_cracking
_stress[_qp],youngs_modulus);
                    _crack_flag[_qp]=1.0;
         }
         else
         {
            _crack_flag[_qp]==0.0;
         }
      }
      else
      {
         // If the crack is propagating
         if (_crack_flag_old[_qp]==1.0 && _equivalent_strain[_qp]>_equivalent_strain_old[_qp])
         {

           computeDamageEvolution(_equivalent_strain[_qp],_crack_initiation_strain[_qp],_actual_cracking
_stress[_qp],youngs_modulus);
             if (_damage_index[_qp]>0.1)
             Real a =_t;
         }
         // If the crack exist but is not propagating
         else
         {
                    _damage_index[_qp]=_damage_index_old[_qp];
                    _cracking_yield_surface[_qp]=_cracking_yield_surface_old[_qp];
           _crack_flag[_qp]=1.0;
         }
      }
}


void IsotropicDamage::computeDamageEvolution
          (Real equivalent_strain, Real cracking_strain, Real cracking_stress, Real youngs_modulus)
```

```
{
 Real residual_stress = _residual_frac*cracking_stress;
 // Get characteristic length for element
 Real hce=_current_elem->volume();
 if (_mesh.dimension()==2)
 {
 if (_current_elem->type() == 3 || _current_elem->type() == 4)
 hce=std::sqrt(2*_current_elem->volume());
 if (_current_elem->type() == 5 || _current_elem->type() == 6 || _current_elem->type() == 7)
 hce=std::sqrt(_current_elem->volume());
 }
 if (_mesh.dimension()==3)
 {
 if (_current_elem->type() == 8 || _current_elem->type() == 9)
 hce=std::cbrt(5*_current_elem->volume());
 if (_current_elem->type() == 10 || _current_elem->type() == 11 || _current_elem->type() == 12 )
 hce=std::cbrt(_current_elem->volume());
 }

 switch (_cracking_release)
 {
          case CrackingRelease::linear:
          {
          // Compute fracture strain
          const Real fracture_strain=2*_Gf/(cracking_stress*hce);
     const Real maximum_strain=cracking_strain-(cracking_stress-residual_stress)*(cracking_strain-
fracture_strain)/cracking_stress;
     if (equivalent_strain<maximum_strain)
          _damage_index[_qp]=std::min(std::max(1-cracking_stress*(equivalent_strain-
fracture_strain)/(cracking_strain-
fracture_strain)/youngs_modulus/equivalent_strain,_damage_index_old[_qp]),1.0);
     else
     {
     _damage_index[_qp]=std::min(std::max(1-
residual_stress/youngs_modulus/equivalent_strain,_damage_index_old[_qp]),1.0);
     }
     _cracking_yield_surface[_qp]=std::max(std::min(cracking_stress*(equivalent_strain-
fracture_strain)/(cracking_strain-fracture_strain),cracking_stress),residual_stress);

     break;
          }
          case CrackingRelease::exponential:
          {
          const Real beta=youngs_modulus*cracking_strain*hce/_Gf;
          if (residual_stress>0)
     {
                    Real maximum_strain = cracking_strain-1/beta*std::log(residual_stress/cracking_stress);
          if (equivalent_strain<maximum_strain)
          _damage_index[_qp]=std::min(std::max(1-cracking_strain/equivalent_strain*std::exp(-
beta*(equivalent_strain-cracking_strain)),_damage_index_old[_qp]),1.0);
          else
          _damage_index[_qp]=std::min(std::max(1-
residual_stress/youngs_modulus/equivalent_strain,_damage_index_old[_qp]),1.0);
          }
          else
```

```
      {
          _damage_index[_qp]=std::min(std::max(1-cracking_strain/equivalent_strain*std::exp(-
beta*(equivalent_strain-cracking_strain)),_damage_index_old[_qp]),1.0);
          }

          _cracking_yield_surface[_qp]=std::max(std::min(cracking_stress*cracking_strain/equivalent_strai
n*std::exp(-beta*(equivalent_strain-cracking_strain)),cracking_stress),residual_stress);
          break;
          }
          case CrackingRelease::brittle:
          {
                    std::vector<Real> eigval(3, 0.0);
                    _stress[_qp].symmetricEigenvalues(eigval);
                    Real max_principal_stress=std::max(std::max(eigval[0],eigval[1]),eigval[2]);
          _damage_index[_qp]=1-residual_stress/max_principal_stress;
          _cracking_yield_surface[_qp]=residual_stress;
          break;
          }
  }
}
```

APPENDIX C

BAZANT NAJJAR DIFFUSION CODE

```
clear all;
shrink_ult1=2000E-6;
shrink_ult2=6000E-6;
%%parameter
fb=3e-1;
DI=60.0;
alp=0.05;
hc=0.8;
hen=0.875;
hen2=0.5;
n=15;
T=10;
nt=11;
L=12.5;
dx=0.25;
nx=0:dx:L;
dt=T/(nt-1);
tol=10^-9;maxiter=500;
ni=length(nx);

%%stiffness and force
K= zeros(ni);
FF=zeros(ni,1);
h=ones(ni,nt);



for mm=3:nt
res=10; kk=1;
if (mm>8)
   hen=hen2;
end
while (res)>tol
kk=kk+1;
if (kk >= maxiter)
   fprintf('Newton iteration failed to converge');
   break; %breaks from for or while loop
end
Dh(1)=DI*(alp+(1-alp)/(1+(1-h(1,mm))/(1-hc)^n));
rr(1)=dt*Dh(1)/dx/dx;
bt(1)=1+fb*dx/Dh(1);
gm(1)=fb*dx*hen/Dh(1);
K(1,1)=1+2*rr(1)*bt(1);
K(1,2)=-2*rr(1);
FF(1,1)=h(1,mm-1)+2*rr(1)*gm(1);

Dh(ni)=DI*(alp+(1-alp)/(1+(1-h(ni,mm))/(1-hc)^n));
rr(ni)=dt*Dh(ni)/dx/dx;
bt(ni)=1+fb*dx/Dh(ni);
gm(ni)=fb*dx*hen/Dh(ni);
K(ni,ni)=1+2*rr(ni);K(ni,ni-1)=-2*rr(ni);
FF(ni,1)=h(ni,mm-1);

for mk=2:ni-1
Dh(mk)=DI*(alp+(1-alp)/(1+(1-h(mk,mm))/(1-hc)^n));
```

```
rr(mk)=dt*Dh(mk)/dx/dx;
bt(mk)=1+fb*dx/Dh(mk);
gm(mk)=fb*dx*hen/Dh(mk);
K(mk,mk)=1+2*rr(mk);K(mk,mk-1)=-rr(mk);K(mk,mk+1)=-rr(mk);
FF(mk,1)=h(mk,mm-1);
end
hh=K\FF;
res=norm(hh-h(:,mm));
h(:,mm)=hh;
end
end
Shrinakge_strain(:,1:8)=-shrink_ult1*(1-h(:,1:8));
Shrinakge_strain(:,9:nt)=-shrink_ult2*(1-h(:,9:end));

close all
for kkk=1:1:nt
plot(nx,h(:,kkk),'k')
hold on
end
xlabel('Distance from drying face (mm)');
ylabel('Humidity, H');
plot([12.5;12.5],[0.825;1], 'k--');
annotation('textarrow',[.75,.823],[0.5,.5],'String',{'Mid Depth';' of Specimen'})
figure()
for kkk=1:1:nt
plot(nx,Shrinakge_strain(:,kkk)*10^6,'k')
hold on
end
plot([12.5;12.5],[0;-600], 'k--');
annotation('textarrow',[.75,.823],[0.7,.7],'String',{'Mid Depth';' of Specimen'})
xlabel('Distance from drying face (mm)');
ylabel('Shrinkage Strain \mum/m');


Shrinakge_strain=Shrinakge_strain';
```

APPENDIX D

CODE FOR COMPUTING VISCOELASTIC MODULI

```
%%OPC          PCM10          PCM20
%%pa=1         pa=2           pa=3

clear all
% clf('reset')
pa=2;
if (pa==1)
% % OPC
   kappa=1.7423;
   lambda=0.3402;
   k1=1.7;
   k2=0.477;
   t=0:1:41;                          %%t is the total time/tdash
   tdash=t;
   tdash=tdash';
   tminustdash=0:1:20;
   EM=9580*kappa*(1-exp(-lambda*(t+1)));
%     EM=2134.2*log(t)+10465;
   EM(1,1)=0;
   for i=2:1:21                        %% i repersnts location of tdash, i=tdash+1

   alpha0=(11.854*log(i-1)+42.286)/100;
      for j=i:1:i+20                   %% j represnts total_t+1
      alpha=(11.854*log(j-1)+42.286)/100;
      fd=(alpha-alpha0)/alpha0;
      phi=k1*fd^k2;
      Er(i,j-i+1)=EM(i)/(1+phi);
      end
   end

   for i=2:1:42
   alpha0=(11.854*log(i-1)+42.286)/100;
      for j=i:1:i+21
      alpha=(11.854*log(j-1)+42.286)/100;
      fd=(alpha-alpha0)/alpha0;
      phi=k1*fd^k2;
      Jr(i,j)=(1+phi)/EM(i);
      end
   end

    for i=2:1:21
       for j=i:1:i+20
          del=(j-i)/2;
            t1=floor(del);
            t2=ceil(del);
            tot_t=j-1;
            tdash_t=i-1;
            Jrtminusdeltdash=interp1([tot_t+1-t2;tot_t+1-t2+1],[Jr(tdash_t+1,tot_t+1-t2);Jr(tdash_t+1,tot_t+1-
t2+1)],tot_t+1-del);

Jrtdashtplusdel=interp1([tdash_t+1+t1;tdash_t+1+t1+1],[Jr(tdash_t+1+t1,tot_t+1);Jr(tdash_t+1+t1+1,tot_t+
1)],tdash_t+1+del);
%               clc
             [tdash_t,tot_t,del]
```

```
            [tot_t-t2,tot_t-t2+1,tot_t-del]
            [Jr(tdash_t,tot_t-t1),Jr(tdash_t,tot_t-t1+1)]
%               [tdash_t+1+t1,tdash_t+1+t1+1,tdash_t+1+del]
%               [Jr(tdash_t+1+t1,tot_t+1);Jr(tdash_t+1+t1+1,tot_t+1)]
          Er1(i,j-i+1)=0.992/Jr(i,j)-0.115*EM(i)*(Jrtminusdeltdash/Jrtdashtplusdel-1);
        end
     end
   t1=0:1:20;
   tdash=t1;
   tdash=tdash';
   for count=2:1:length(tdash)
%        plot((tdash(count,1)+tminustdash),Er(count,1:length(tminustdash)),'k--');
       plot((tdash(count,1)+tminustdash),Er1(count,1:length(tminustdash)),'r--');
       hold on
   end

   for i=2:1:42
   alpha0=(11.854*log(i)+42.286)/100;
      for j=i:1:i+21
      alpha=(11.854*log(j)+42.286)/100;
      fd=(alpha-alpha0)/alpha0;
      phi=k1*fd^k2;
      JrbyJo(i,j)=(1+phi);
      end
   end
   plot(t,EM,'k')
   hold on
   xlabel('Time (Days)');
   ylabel('Modulus (MPa)');
   title('Viscoelastic Modulus for OPC')
   ylim([0 20000]);
   Er=Er1;
   EM=EM';
   Er=Er';
end

if (pa==2)
   %%PCM-10%
   kappa=1.3;
   lambda=0.3742;
   k1=2;
   k2=0.5;
   t=0:1:41;
   tdash=t;
   tdash=tdash';
   tminustdash=0:1:20;
   EM=8300*kappa*(1-exp(-lambda*(t+1)));
   EM(1,1)=0;
   for i=2:1:21

   alpha0=(11.854*log(i)+42.286)/100;
      for j=i:1:i+20
         alpha=(11.854*log(j)+42.286)/100;
         fd=(alpha-alpha0)/alpha0;
```

```
        phi=k1*fd^k2;
        Er(i,j-i+1)=EM(i)/(1+phi);
      end
   end

   for i=2:1:42
   alpha0=(11.854*log(i)+42.286)/100;
      for j=i:1:i+21
      alpha=(11.854*log(j)+42.286)/100;
      fd=(alpha-alpha0)/alpha0;
      phi=k1*fd^k2;
      Jr(i,j)=(1+phi)/EM(i);
      end
   end

    for i=2:1:21
       for j=i:1:i+20
          del=(j-i)/2;
           t1=floor(del);
           t2=ceil(del);
           tot_t=j;
           tdash_t=i;
           Jrtminusdeltdash=interp1([tot_t-t2;tot_t-t2+1],[Jr(tdash_t,tot_t-t2);Jr(tdash_t,tot_t-t2+1)],tot_t-
del);

Jrtdashtplusdel=interp1([tdash_t+t1;tdash_t+t1+1],[Jr(tdash_t+t1,tot_t);Jr(tdash_t+t1+1,tot_t)],tdash_t+del)
;
%              clc
%              [tdash_t,tot_t,del]
%              [tot_t-t2,tot_t-t2+1,tot_t-del]
%              [Jr(tdash_t,tot_t-t1),Jr(tdash_t,tot_t-t1+1)]
%              [tdash_t+t1,tdash_t+t1+1,tdash_t+del]
%              [Jr(tdash_t+t1,tot_t);Jr(tdash_t+t1+1,tot_t)]
          Er1(i,j-i+1)=0.992/Jr(i,j)-0.115*EM(i)*(Jrtminusdeltdash/Jrtdashtplusdel-1);
       end
    end
   t1=0:1:20;
   tdash=t1;
   tdash=tdash';
   for count=2:1:length(tdash)
%        plot((tdash(count,1)+tminustdash),Er(count,1:length(tminustdash)),'k--');
      plot((tdash(count,1)+tminustdash),Er1(count,1:length(tminustdash)),'r--');
      hold on
   end




   plot(t,EM,'k')
   plot(t,EM,'k')
   hold on
   xlabel('Time (Days)');
   ylabel('Modulus (MPa)');
```

```
    title('Viscoelastic Modulus for 10%PCM')
    ylim([0 20000]);
    hold on
    Er=Er1;
    EM=EM';
    Er=Er';
end

if (pa==3)
    %%PCM-20%
    kappa=1.3705;
    lambda=0.377;
    k1=2;
    k2=0.5;
    t=0:1:41;
    tdash=t;
    tdash=tdash';
    tminustdash=0:1:20;
    EM=6000*kappa*(1-exp(-lambda*(t+1)));
    EM(1,1)=0;
    for i=2:1:21

        alpha0=(11.854*log(i)+42.286)/100;
        for j=i:1:i+20
            alpha=(11.854*log(j)+42.286)/100;
            fd=(alpha-alpha0)/alpha0;
            phi=k1*fd^k2;
            Er(i,j-i+1)=EM(i)/(1+phi);
        end
    end

    for i=2:1:42
    alpha0=(11.854*log(i)+42.286)/100;
        for j=i:1:i+21
        alpha=(11.854*log(j)+42.286)/100;
        fd=(alpha-alpha0)/alpha0;
        phi=k1*fd^k2;
        Jr(i,j)=(1+phi)/EM(i);
        end
    end

     for i=2:1:21
         for j=i:1:i+20
            del=(j-i)/2;
              t1=floor(del);
              t2=ceil(del);
              tot_t=j;
              tdash_t=i;
              Jrtminusdeltdash=interp1([tot_t-t2;tot_t-t2+1],[Jr(tdash_t,tot_t-t2);Jr(tdash_t,tot_t-t2+1)],tot_t-
del);

Jrtdashtplusdel=interp1([tdash_t+t1;tdash_t+t1+1],[Jr(tdash_t+t1,tot_t);Jr(tdash_t+t1+1,tot_t)],tdash_t+del)
;
%               clc
```

```
%               [tdash_t,tot_t,del]
%               [tot_t-t2,tot_t-t2+1,tot_t-del]
%               [Jr(tdash_t,tot_t-t1),Jr(tdash_t,tot_t-t1+1)]
%               [tdash_t+t1,tdash_t+t1+1,tdash_t+del]
%               [Jr(tdash_t+t1,tot_t);Jr(tdash_t+t1+1,tot_t)]
          Er1(i,j-i+1)=0.992/Jr(i,j)-0.115*EM(i)*(Jrtminusdeltdash/Jrtdashtplusdel-1);
        end
     end
    t1=0:1:20;
    tdash=t1;
    tdash=tdash';
    for count=2:1:length(tdash)
%         plot((tdash(count,1)+tminustdash),Er(count,1:length(tminustdash)),'k--');
        plot((tdash(count,1)+tminustdash),Er1(count,1:length(tminustdash)),'r--');
        hold on
    end

    plot(t,EM,'k')
    hold on
    xlabel('Time (Days)');
    ylabel('Modulus (MPa)');
    title('Viscoelastic Modulus for 20%PCM');
    ylim([0 20000]);
    hold on
    Er=Er1;
    EM=EM';
    Er=Er';
end

if (pa==4)
    %%PCM-20%
    kappa=1.5756;
    lambda=0.3306;
    k1=2;
    k2=0.5;
    t=0:1:41;
    tdash=t;
    tdash=tdash';
    tminustdash=0:1:20;
    EM=12240*kappa*(1-exp(-lambda*(t+1)));
    EM(1,1)=0;
    for i=2:1:21                        %% i repersnts location of tdash, i=tdash+1

    alpha0=(11.854*log(i-1)+42.286)/100;
        for j=i:1:i+20                  %% j represnts total_t+1
        alpha=(11.854*log(j-1)+42.286)/100;
        fd=(alpha-alpha0)/alpha0;
        phi=k1*fd^k2;
        Er(i,j-i+1)=EM(i)/(1+phi);
        end
    end

    for i=2:1:42
    alpha0=(11.854*log(i-1)+42.286)/100;
```

```
      for j=i:1:i+21
      alpha=(11.854*log(j-1)+42.286)/100;
      fd=(alpha-alpha0)/alpha0;
      phi=k1*fd^k2;
      Jr(i,j)=(1+phi)/EM(i);
      end
   end

    for i=2:1:21
       for j=i:1:i+20
          del=(j-i)/2;
            t1=floor(del);
            t2=ceil(del);
            tot_t=j-1;
            tdash_t=i-1;
            Jrtminusdeltdash=interp1([tot_t+1-t2;tot_t+1-t2+1],[Jr(tdash_t+1,tot_t+1-t2);Jr(tdash_t+1,tot_t+1-
t2+1)],tot_t+1-del);

Jrtdashtplusdel=interp1([tdash_t+1+t1;tdash_t+1+t1+1],[Jr(tdash_t+1+t1,tot_t+1);Jr(tdash_t+1+t1+1,tot_t+
1)],tdash_t+1+del);
%               clc
             [tdash_t,tot_t,del]
             [tot_t-t2,tot_t-t2+1,tot_t-del]
             [Jr(tdash_t,tot_t-t1),Jr(tdash_t,tot_t-t1+1)]
%               [tdash_t+1+t1,tdash_t+1+t1+1,tdash_t+1+del]
%               [Jr(tdash_t+1+t1,tot_t+1);Jr(tdash_t+1+t1+1,tot_t+1)]
          Er1(i,j-i+1)=0.992/Jr(i,j)-0.115*EM(i)*(Jrtminusdeltdash/Jrtdashtplusdel-1);
       end
    end
   t1=0:1:20;
   tdash=t1;
   tdash=tdash';
   for count=2:1:length(tdash)
%        plot((tdash(count,1)+tminustdash),Er(count,1:length(tminustdash)),'k--');
      plot((tdash(count,1)+tminustdash),Er1(count,1:length(tminustdash)),'r--');
      hold on
   end

   for i=2:1:42
   alpha0=(11.854*log(i)+42.286)/100;
      for j=i:1:i+21
      alpha=(11.854*log(j)+42.286)/100;
      fd=(alpha-alpha0)/alpha0;
      phi=k1*fd^k2;
      JrbyJo(i,j)=(1+phi);
      end
   end
   plot(t,EM,'k')
   hold on
   xlabel('Time (Days)');
   ylabel('Modulus (MPa)');
   title('Viscoelastic Modulus for OPC')
   ylim([0 20000]);
   Er=Er1;
```

```
    EM=EM';
    Er=Er';
end
```

APPENDIX E

CODE FOR COMPUTING MAXWELL CHAIN PARAMETERS

```
clearvars -except Er tdash tminustdash EM pa;
close all
t=1;
%% Number of Maxwell Chain
tau_mu=[0.001;0.004;0.016;0.064;0.256;1.024;4.096;inf];
n=length(tau_mu);
w1=0.1;
w2=0.1;
Aeq=ones(1,n);
lb=zeros(1,n+1);
ub=Inf*ones(1,n+1);
W1=zeros(n,n);
W2=zeros(n,n);
W1(1,1:2)=w1*[1,-1];
W1(n-1,n-2:n-1)=w1*[-1,1];
for i=2:1:n-2
W1(i,i-1:i+1)=w1*[-1,2,-1];
end
W2(1,1:3)=w2*[1,-2,1];
W2(n-1,n-3:n-1)=w2*[1,-2,1];
W2(2,1:4)=w2*[-2,5,-4,1];
W2(n-2,n-4:n-1)=w2*[1,-4,5,-2];
for i=3:1:n-3
W2(i,i-2:i+2)=w2*[1,-4,6,-4,1];
end
%%% Running loop over tdash
for i=1:1:length(tdash)
   beq=Er(i,1);
   clear X Y;
   X=zeros(n,n);
   Y=zeros(n,1);
   % Running loop over equations
   for ll=1:1:n
   % Running loop over t-t'
   for k=1:1:length(tminustdash)
      Y(ll,1)=Y(ll,1)+Er(i,k)*exp(-(tminustdash(1,k))/tau_mu(ll,1));
       % running loop over maxwell chains
       for j=1:1:n
       X(ll,j)=X(ll,j)+exp(-(tminustdash(1,k))/tau_mu(j,1))*exp(-(tminustdash(1,k))/tau_mu(ll,1));
       end
   end
   end
   %% Adding penalty terms
     X=X+W1+W2;
      Coeff(i,2:n+1)=regress(Y,X);
   Coeff(i,1)=tdash(i,1);
%      Coeff(i,2:n+1)=lsqlin(X,Y,[],[],Aeq,beq,lb,ub);
end
tau_mu(end,1)=78.125;
surf(tau_mu(:,1),Coeff(:,1),Coeff(1:length(tdash),2:n+1))
set(gca, 'XScale', 'log')
% set(gca, 'ZScale', 'log')
xlabel('\tau_\mu (Days)');
ylabel('Age, t^, (Days)');
zlabel('E_\mu ');
```

```
if (pa==1)
title('Relaxation Spectrum OPC')
elseif (pa==2)
title('Relaxation Spectrum 10%PCM')
elseif (pa==3)
title('Relaxation Spectrum 20%PCM')
elseif (pa==4)
title('Relaxation Spectrum 10%Quartz')
end
figure();
tau_mu(end,1)=inf;
Erfitted=zeros(length(tdash),length(tminustdash));
for i=1:1:length(tdash)
   for k=1:1:length(tminustdash)
      for j=1:1:n
      Erfitted(i,k)=Erfitted(i,k)+Coeff(i,j+1)*exp(-(tminustdash(1,k))/tau_mu(j,1));
      end
   end
end
for i=1:1:length(tdash)
plot((tdash(i,1)+tminustdash),Er(i,1:length(tminustdash)),'o');
hold on
plot((tdash(i,1)+tminustdash),Erfitted(i,1:length(tminustdash)),'k--');
end

figure();
for i=2:1:20
plot(Coeff(i,2:end),'o--')
hold on
end
Coeff1=round(Coeff,2);
```